Modulated Impedance Boundary Conditions
For
Leaky-Wave Antenna Analysis and Design

Bakhtiar Ali Khan

A Thesis
In the Department
of
Electrical and Computer Engineering

Presented in Partial Fulfillment of the Requirements
For the Degree of
Doctor of Philosophy (Electrical and Computer Engineering) at
Concordia University
Montreal, Quebec, Canada

January 2019

CONCORIDA UNIVERSITY

SCHOOL OF GRADUATE STUDIES

This is to certify that the thesis prepared

By: Bakhtiar Ali Khan

Entitled: Modulated Impedance Boundary Conditions For Leaky-Wave Antenna Analysis and Design

and submitted in partial fulfillment of the requirements for the degree of

Doctor of Philosophy (Electrical and Computer Engineering)

complies with the regulations of this University and meets the accepted standards with respect to originality and quality.

Signed by the final examining committee:

____ Chair
Dr. Muthukumaran Packirisamy

____ External Examiner
Dr. Yahia M. M. Antar

____ External to Program
Dr. Marius Paraschivoiu

____ Examiner
Dr. Ahmed A. Kishk

____ Examiner
Dr. Christopher W. Trueman

____ Thesis Supervisor
Dr. Robert Paknys

Approved by ____
Dr. Mustafa Mehmet Ali, Graduate Program Director

March 21, 2019 ____________________________________
Dr. Amir Asif, Dean
Gina Cody School of Engineering & Computer Science

Abstract

Modulated Impedance Boundary Conditions for Leaky-Wave Antenna Analysis and Design

Bakhtiar Ali Khan, Ph.D.

Concordia University, January 2019

In this thesis we examine the surface impedance of a grounded dielectric slab with a periodic perturbation of its geometry or permittivity. Using the impedance boundary condition (IBC) allows for the reduction in the number of physical structural parameters such as width, height and permittivity to one single parameter, which is the impedance Z_s. This simplifies the electromagnetic problem. We reduce a 3D IBC problem to a 2D IBC problem because it is suitable for modeling the principal planes of the 3D problem. The 3D and 2D problems are related through a Fourier transform and the 2D problem is relatively easy to analyze.

In the literature, one can find the solution for a constant IBC. However, we are interested in a general IBC field solution that allows for an arbitrary impedance. Commercial electromagnetic solvers do allow for a penetrable IBC but do not allow for an impenetrable IBC. The proposed IBC-MoM (method of moments) is a general solution that allows for an arbitrary impenetrable IBC. We will use this solution for leaky-wave antenna design.

For an IBC to accurately model a physical electromagnetic problem, the surface impedance must match the impedance of the true physical antenna that is being modeled. In general this will not be a constant and depends on the source configuration. It is therefore imperative to consider the surface impedance variation as the excitation is changed. Using the rigorous 2D Green's function field solution for the grounded dielectric slab, it is shown how the surface impedance varies as the excitation source location is changed. For the transmit problem (source close to the slab surface), a Sommerfeld integral is numerically evaluated in the complex w plane, which allows one to compute the exact surface impedance at any surface point, including points near the source. The surface impedance from the exact solution is shown to agree with a numerical electromagnetic full-wave (COMSOL) solution.

For a transmitting antenna the surface impedance is a relatively complicated function, compared to the receiving case. It is therefore incorrect to assume that surface impedance is simply a number based on plane wave incidence, when considering transmitting antennas. This is illustrated by considering the surface impedance on a grounded slab, which is excited by a line source close to the slab surface. For the IBC to have the same field as the original grounded slab, the surface impedance should match the actual slab– and it is not a constant, but varies, especially near the source. A closed form analytic IBC Green's function is not possible when the surface impedance is a function over the surface. However, we can still obtain an exact solution by using radiation integrals on the infinite aperture. We decompose the true aperture fields from the grounded slab problem into geometrical optics (GO) and the surface wave parts. This in turn allows one to compute the field solution by solving the radiation integrals over an infinite aperture. The field solution is shown to agree with COMSOL, which validates the concept.

Sinusoidal and square-wave modulations of the surface reactance are considered. An impenetrable IBC in conjunction with the MoM is used to obtain the radiation patterns for 2D leaky-wave antennas of finite extent. In order to physically realize the modulation, we start with the theory of a grounded dielectric slab. The slab supports a surface wave and a fast spatial harmonic (in our case $n = -1$) will be excited via periodic perturbation of the slab along the guiding direction. First, a sinusoidal reactance modulation is analytically mapped into a slab thickness modulation. Second, a square-wave reactance modulation is mapped into a permittivity modulation, and is realized with subwavelength perforations. The radiation patterns from the 3D physical antennas are computed with a commercial electromagnetic solver (CST) and are validated with our simplified 2D IBC-MoM code. The resulting scan angles and beamwidths predicted by the CST model are found to agree with the 2D IBC-MoM. The 2D model is shown to be useful, because it can treat not only sinusoidal and square-wave modulations but any profile. Therefore, it becomes easy to rapidly predict in 2D the key radiation characteristics (the scan direction and beamwidth) for impedance profiles that are arbitrary. Aspects of the feed design for the 2D and 3D models are addressed to minimize contamination of the radiation pattern by direct radiation from the source.

The extreme near field on the surface is computed with CST and the results confirm that the expected surface impedances are being realized by the thickness-modulated and permittivity-modulated structures.

Acknowledgments

First and foremost, I would like to thank my supervisor Professor R. Paknys for accepting me as his student and for his continued support, advice and motivation. His guidance has been tremendously helpful for the successful realization of this work. This thesis is substantially based on the discussions and meetings I had with Professor R. Paknys. Thanks to the literal and metaphorical open door, I was afforded the opportunity for very frequent interactions during the course of my research.

I would also like to thank the committee members, namely Professor A. Kishk, C.W. Trueman and M. Paraschivoiu from Concordia University Montreal and Professor Yahia M. M. Antar from Royal Military College Kingston for taking the time and their valued comments.

Special thanks to Karim Achouri, Shulabh Gupta and Walid Deyab with whom I had interesting and thought provoking scientific discussions.

I also would like to thank all my friends and family members for their continued support notably Shahnaz, Waqar Khan, Waqar Yousafzai, Shahroon, Majid, Zoé, Luzhou, and Vincent.

I would also like to extend my gratitude to Professor J. J. Laurin from Polytechnique Montreal and the chair of the committee Professor Dr. M. Packirisamy and graduate office coordinator Miss S. Tablan from ENCS Concordia for their help and support.

To Shahnaz

for her patience and forbearance.

Contents

List of Figures

List of Tables

Chapter 1

Introduction

Leaky-wave antennas can be considered as a class of traveling wave antennas that allows the energy to radiate as the wave propagates along the guiding structure. In general, these are low profile antennas capable of producing a directive beam. Relative to a phased array antenna, leaky-wave antennas are simpler in terms of design as they do not need complicated feed networks. However, the inherent frequency beam scanning of a leaky-wave antenna can be an asset in scanning applications and a liability in point to point communication over a wider frequency band [1].

The utility of the IBC is central to leaky-wave antenna design. Using the IBC, a physically complicated electromagnetic problem can be simplified to an equivalent electromagnetic problem. The equivalent problem is simpler to solve for the currents and fields. A surface wave (slow wave) on an impedance boundary of finite extent has an end-fire beam. The periodic modulation of the surface impedance allows a leaky-wave mode to exist on the surface which can radiate in the off end-fire direction (see [2], Sec. 11.3).

A given surface impedance variation can potentially allow for the synthesis of a pencil beam radiation with the desired pattern parameters, such as side lobe level and beamwidth. Furthermore, a certain kind of surface impedance variation may be required for a circularly polarized pencil beam. Due to the inherent high directivity of a pencil beam and robustness of circular polarization to polarization mismatch, this kind of radiation pattern is much desired in space applications.

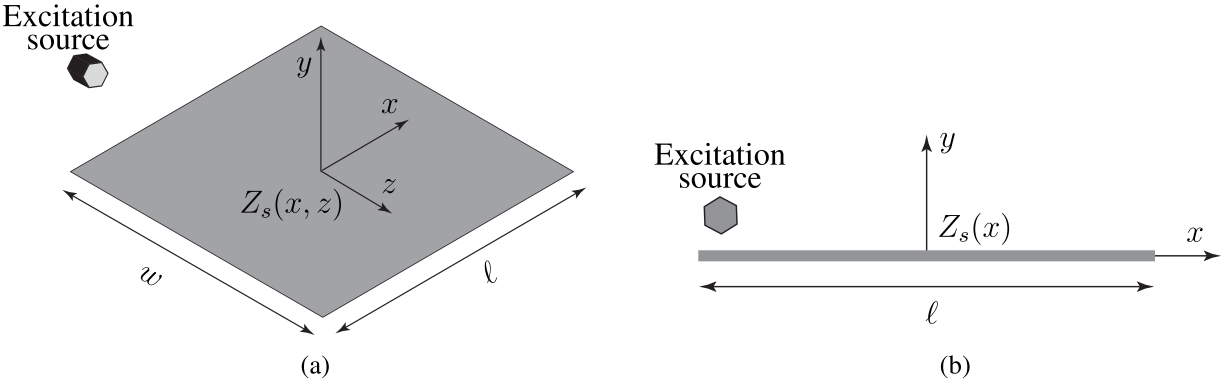

Figure 1.1: a) Illustration of an impedance surface with 2D impedance variation $Z_s(x, z)$. b) Illustration of an impedance strip with 1D impedance variation $Z_s(x)$.

1.1 Problem and Approach

A real physical surface can be modeled by an IBC. Consider an arbitrary impedance surface of finite extent in the x-z plane, which is excited by a source, as shown in Fig. 1.1. The question here is, how to predict the radiation pattern of a finite-extent surface with an arbitrary surface impedance variation? It motivates a need to develop an MoM code for this case. Having a general model that can do this would be useful for leaky-wave antenna design.

We will reduce the 3D problem in Fig. 1.1(a) with $Z_s(x, z)$ to a 2D problem as shown in Fig. 1.1(b). The 2D problem is easier to solve but also less practical. In the 2D problem, variation along the z direction is considered to be zero $(\partial/\partial z = 0)$. Consequently, the spatial impedance variation is reduced to 1D, which is $Z_s(x)$. As shown in Fig. 1.1(b), an impenetrable arbitrary impedance strip of finite extent in the x direction is excited by a source which is very close to the strip. This 2D problem is relatively easy to analyze and is also computationally much faster. However, with this 2D problem (1D impedance variation) one can only predict the principal-plane pattern of the 3D case.

In Fig. 1.1(b) enforcing the IBC at $y = 0$, allows us to write the coupled electric and magnetic field integral equations. Taking advantage of the flat geometry and assuming the top and bottom strip impedances to be the same, we can use field symmetries to decouple the electric and magnetic field integral equations. These decoupled equations can be used in conjunction with the MoM to solve for the equivalent electric and magnetic surface currents. From these currents one can compute the far field radiation pattern for an impenetrable arbitrary impedance strip.

It is also a point of interest that the penetrable thin sheet IBC is widely available in commercial solvers, but the impenetrable (or opaque) IBC is not. It is therefore imperative to develop an IBC-MoM code.

The second problem to investigate is, how to physically realize a given surface impedance? This is important for leaky-wave antenna design. This motivates the need to investigate the relation between the IBC problem and the true physical problem. For the IBC to have the same field as the true physical problem, the surface impedance has to be the same as for the true physical problem. How does the source configuration change the surface impedance? Using the rigorous 2D Green's function field solution for the grounded dielectric slab, it will be shown how the surface impedance varies as the excitation source location is changed. In particular, Z_s for a transmitting configuration (source near the surface $\mathrm{T_x}$) is significantly different from the receiving case (source far away $\mathrm{R_x}$). Consequently, one cannot use the same Z_s for the $\mathrm{T_x}$ and for $\mathrm{R_x}$.

In order to physically realize a given surface impedance modulation, we will use a grounded dielectric slab. A grounded dielectric slab can support a surface wave. By employing the theory of the dielectric grounded slab (see [3], Sec. 3.6.2), the surface impedance $Z_s(x)$ can be mapped onto the slab thickness $d(x)$. This subsequently allows us to obtain a desired surface impedance modulation via thickness modulation of the grounded dielectric slab. Alternatively, we also use the permittivity modulation $\epsilon_r(x)$ of a grounded slab to obtain a desired surface impedance modulation. The permittivity modulation of the slab is achieved via perforations.

1.2 Thesis Overview

The thesis organization is as follows. Chapter 2 provides the essential background on modulated surface impedance and it covers the pertinent literature in detail. In Chapter 3, surface IBC variation due to the excitation source location relative to the IBC is discussed followed by the development of the integral equations, which are subsequently used in conjunction with the MoM to solve for an arbitrary impenetrable surface impedance modulation. Chapter 4 addresses the physical realization of a given surface impedance modulation by using a grounded dielectric slab, to obtain leaky-wave antenna designs. Aspects of feed design are also considered. Chapter 5 concludes by summarizing the thesis along with outlining some potential avenues for further research.

Chapter 2

Background and Literature Review

In 1969 Hessel [4] and Tamir [5] provided an excellent in-depth analysis on the topic of traveling wave and leaky-wave antennas. Relatively recent studies by Jackson and Oliner [1][2] helped improve the understanding of the topic. Caloz *et al.* [6] discussed some new leaky-wave antenna designs, such as composite right-left handed (CRLH) transmission line based design. Jackson *et al.* [7] provided a nice and concise summary on the topic of leaky-wave antennas.

The principles of periodic leaky-wave antennas are well established. A periodic structure supports a fast wave which radiates by progressively leaking. The idea of an IBC is used in leaky-wave and holographic antenna design. A modulated surface impedance can support a fast spatial harmonic hence it is useful in realizing leaky-wave antennas. This chapter provides the necessary background on modulated surface impedance and it also discusses how people have realized the surface impedance modulation.

2.1 Sinusoidally Modulated Surface Impedance

By using the transverse resonance method in conjunction with Floquet's theorem for periodic structures, Oliner and Hessel [8] provided an elegant closed form eigenvalue solution for a sinusoidally modulated impedance surface in 1959 .

They considered a sinusoidally modulated impedance surface which is shown in Fig. 2.1. The

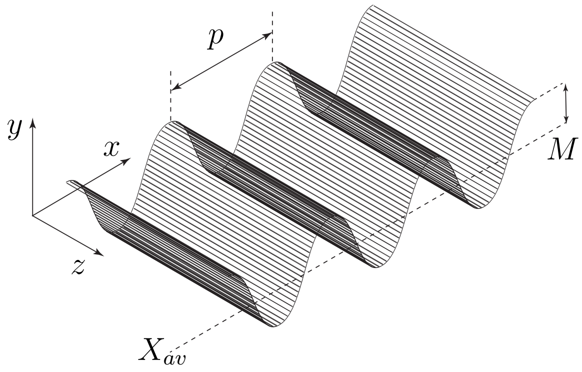

Figure 2.1: Illustration of sinusoidally modulated surface impedance at $y = 0$.

surface is considered to be infinite in the x direction while being invariant in the z direction ($\partial/\partial z = 0$). This surface impedance can be mathematically expressed as

$$Z_s(x) = jX_{av}\left[1 + M\cos\left(\frac{2\pi}{p}x\right)\right] \tag{2.1}$$

where

X_{av} = average reactance
M = modulation index
p = period.

These are the three important parameters that control the propagation constant along the surface. Oliner and Hessel [8] considered an unexcited problem (finding the modes), where the fields obey the IBC in (2.1), and their solution provides the propagation constant along the x direction which is

$$k_x = \beta_n - j\alpha. \tag{2.2}$$

In a periodic structure, the propagation constant of the n^{th} spatial harmonic follows from Floquet's

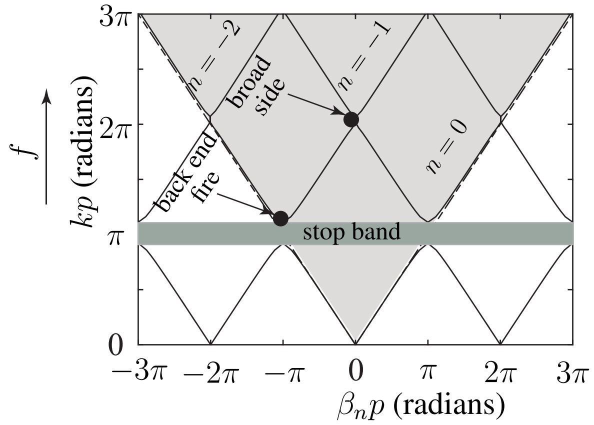

Figure 2.2: Dispersion diagram for a sinusoidally modulated impedance (2.1) with $M = 0.2$, $X_{av} = 377\ \Omega$ and $p = \lambda = 1$ m.

theorem as

$$\beta_n = \beta_0 + \frac{2n\pi}{p} \tag{2.3}$$

where β_0 is the propagation wavenumber along the surface, $n = 0, \pm1, \pm2, \ldots$ denote the spatial harmonics and p is the period.

The detailed derivation that allows one to compute the dispersion diagram shown in Fig. 2.2 is provided in Appendix A. This diagram is sometimes referred to as Brillouin diagram for a periodic structure (see [6], p. 355). From this dispersion diagram we know the β_n for a given spatial harmonic, which is related to the beam angle (with respect to x) as

$$\phi_0 = \cos^{-1}\left(\frac{\beta_n}{k}\right). \tag{2.4}$$

The shaded area in the dispersion diagram, which is bounded by the light line, represents the radiation cone. Any spatial harmonic that lies inside this gray region is called a fast spatial harmonic or sometimes referred to as fast wave, which is to say $\beta/k < 1$ (k is free space propagation constant), and it radiates. To see the behavior more clearly, let us consider $n = -1$ spatial harmonic in Fig. 2.2. As kp (frequency) is increased the $n = -1$ harmonic starts off as a slow wave. As the frequency is further increased, there appears a band of frequencies with no propagation. This called the stop band, as shown in Fig. 2.2. Oliner and Hessel [8] have shown that the stop band bandwidth is directly proportional to the modulation index M. With further increase in frequency, the $n = -1$ spatial harmonic steps into the radiation cone which now becomes a fast wave. From (2.4) we can see that it starts to radiate in the back end-fire direction and goes through the broad side towards the forward-end fire direction as kp (frequency) is increased.

Substituting $M = 0$ and (A.3) in the continued fraction (A.19) gives a simplified approximate relation for k_x; this is the unperturbed case β_u

$$k_x \approx \beta_u = k\sqrt{1 + X_{av}'^2} + \frac{2n\pi}{p} \tag{2.5}$$

with $\alpha = 0$. In order to obtain a nonzero value for the important parameter α, which is related to the beamwidth, and also improve the accuracy of β, Oliner and Hessel provided a perturbation solution for small modulation index M

$$k_x = \beta_u + \Delta\beta - j\alpha \tag{2.6}$$

$$\Delta\beta p - j\alpha p = -\frac{M^2}{4}\frac{kpX_{av}'^2}{\sqrt{1 + X_{av}'^2}}\left(\frac{1}{A} + \frac{1}{B}\right) \tag{2.7}$$

$$\begin{aligned} A &= 1 - \frac{j}{X_{av}'}\sqrt{1 - \left(\sqrt{1 + X_{av}'^2} - \frac{2\pi}{kp}\right)^2} \\ B &= 1 - \frac{j}{X_{av}'}\sqrt{1 - \left(\sqrt{1 + X_{av}'^2} + \frac{2\pi}{kp}\right)^2} \end{aligned}$$

where $X_{av}' = X_{av}/\eta$ and $\eta = 120\pi\ \Omega$. This perturbation solution only takes into account the $n = 0, \pm 1$ spatial harmonics and is inadequate when the beam is in the broad side or end-fire directions. For a more accurate solution (A.19) can be solved and this can also be used for larger values of the modulation index M, if need be.

2.2 Control Over Radiation

How to control the radiation pattern in principle, is another way of saying, what parameter of the surface impedance governs what aspect of the radiation pattern? Understanding this is imperative for the radiation pattern synthesis problem. Let us consider the sinusoidally modulated impedance case, which can be expressed mathematically as in (2.1). The three important parameters are, the average reactance X_{av}, modulation index M and period p. The impedance can be visualized, as shown in Fig. 2.3(a) and (b). The effect of the variation of X_{av} and p can be easily understood from the dispersion diagram in Fig. 2.3(c) and (d), respectively. Knowing X_{av}, p and M allows one to compute k_x through (2.6). The real part of k_x is β_n, which is plotted in Fig. 2.3(c) and (d), as frequency is varied. Only the $n = -1$ spatial harmonic is of interest, which is considered here.

Consider the variation of X_{av}, as shown in Fig. 2.3(c). Changing the average reactance from $X_{av} = 500\ \Omega$ to $X_{av} = 100\ \Omega$, changes the slope of the dispersion line. This can potentially be employed such that the two frequencies f_1 and f_2 end up with the same β_{-1} along the surface. This allows us to have the same beam angle ϕ_0 for both frequencies, from the relation (2.4). As for the frequencies in between f_1 and f_2, in order to keep the β_{-1} same, as we scan the frequency from f_1 to f_2 the X_{av} has to be varied also from $X_{av} = 500\ \Omega$ to $X_{av} = 100\ \Omega$. Similarly the variation of the period from $p = 1\lambda$ to $p = 2\lambda$ leads to a different dispersion line on the dispersion diagram, as shown in Fig. 2.3(d). This can also potentially allow us to have the same β_{-1} for f_1 and f_2 and consequently the same beam angle, according to (2.4).

In general, the propagation constant k_x has two parts, the real part β_{-1}, which governs the beam angle, and the imaginary part α, which governs the beamwidth and side lobe level. The parameter β_{-1} can be controlled by tuning X_{av} and p, while the parameter α is more related to the parameter M.

The modulation index M affects both α and β_{-1}, but the parameter α is more profoundly

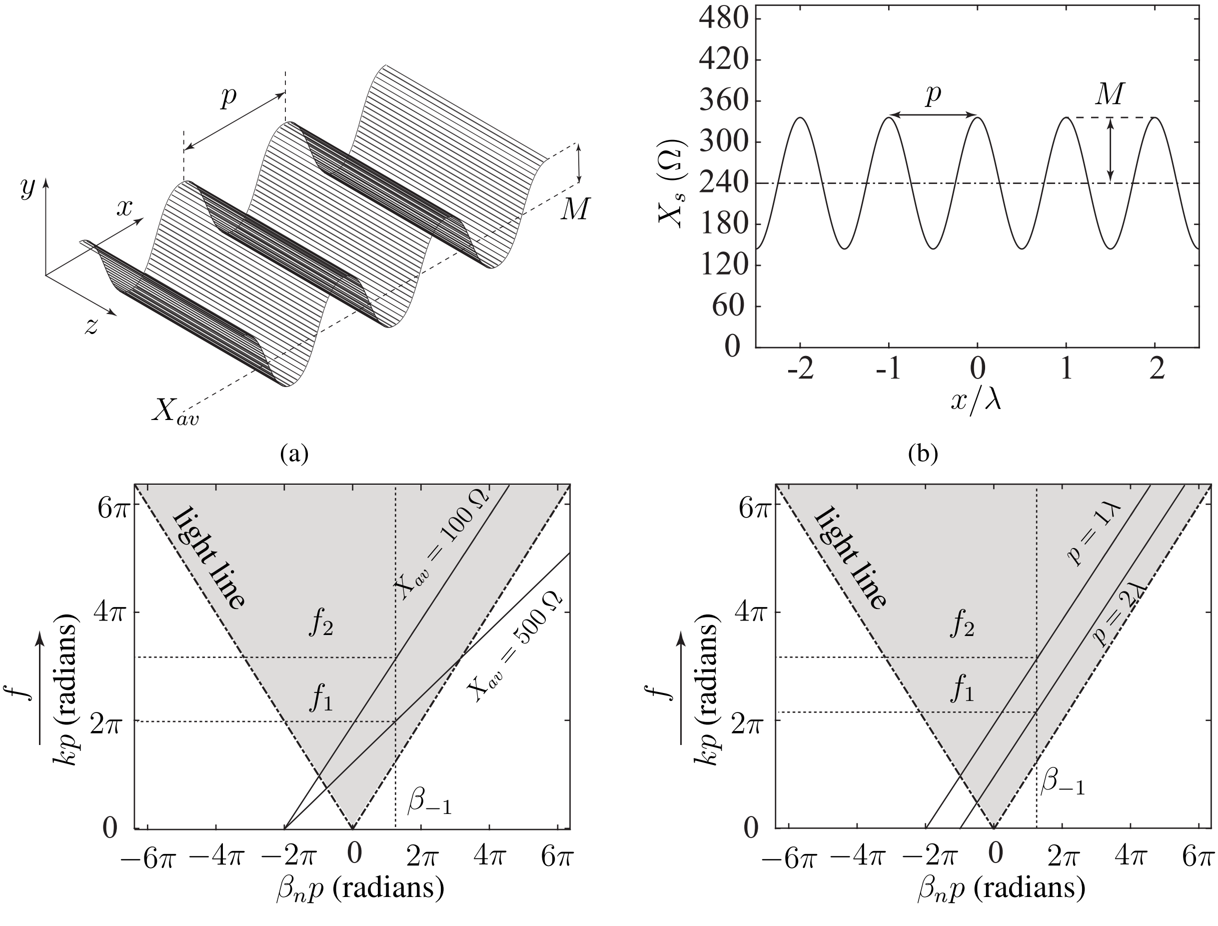

(a) (b)

(c) (d)

Figure 2.3: a) Illustration of sinusoidally modulated surface impedance. b) Reactance $X_s(x)$. c) Dispersion diagram with X_{av} variation for $n = -1$ spatial harmonic $(M = 0.4)$. d) Dispersion diagram with p variation for $n = -1$ spatial harmonic $(M = 0.4)$.

affected by the variation of M. To see this more clearly, let us consider two cases of sinusoidally modulated reactance. In one case, we take the modulation index $M = 0.1$ and in the other case $M = 0.7$. For these two cases the reactance profiles are shown in Fig. 2.4(a). We can use (2.6) and (2.7) to calculate k_x for the two cases, which is then used to evaluate a radiation integral with an aperture field distribution of the form $e^{-jk_x x}$ to obtain the radiation patterns. The radiation patterns for both cases are shown in Fig. 2.4(b) for an aperture integration of 10λ. We can see that a larger M leads to larger values of α. This consequently leads to a wider beam, as shown in Fig. 2.4(b). The variation of M affects β_{-1} as well, as can be seen by the slight change of the beam angle in

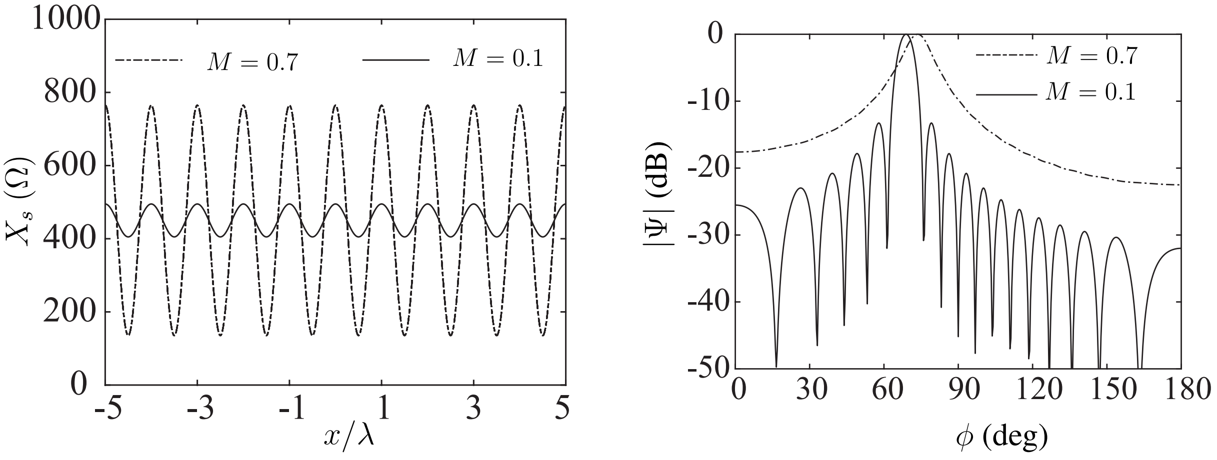

(a)

(b)

Figure 2.4: a) Illustration of sinusoidally modulated reactance for different values of modulation index M. b) Normalized radiation pattern for different values of modulation index M.

Fig. 2.4(b).

2.3 IBC Integral Equations

The IBC integral equations can allow for arbitrary impedance. In 1976, Cho and King [9] developed integral equations for a 2D finite-length impedance strip with sinusoidal modulation on an infinite ground plane. In 1984, Newman and Schrote [10] studied the scattering by a thin planar material slab as well as penetrable and impenetrable impedance boundaries. The planar assumption in conjunction with the symmetry properties of the electric and magnetic currents provided simplifications; uncoupled integral equations were obtained by using the reaction method. Bleyzinski *et al.* [11] later obtained coupled integral equations for the more general non-planar case, and showed that the planar assumption provides decoupling. It appears that the latter formulation is general enough to permit a variable surface impedance, however, they did not explore or test this possibility. In both of the aforementioned papers the application of interest was restricted to finding the radar cross section of a material slab having a constant surface impedance.

We obtained the uncoupled integral equations for a planar and impenetrable variable surface impedance $Z_s(x)$ on a 2D strip. The final form agrees with [10] and [11], provided that their Z_s is replaced with $Z_s(x)$. It is not obvious that this simple replacement would be valid, but it is justified by the derivation in Chapter 3.

2.4 Modulated Surface Impedance Realization

In 1983 Schwering and Peng [12] presented a dielectric grating antenna, an illustration of which is shown in Fig. 2.5(a). The effective dielectric constant method was employed to calculate the propagation constant for the leaky-wave harmonic on a corrugated dielectric slab backed by a ground plane. They considered an unexcited problem also the surface impedance of the structure was not investigated.

In 2011 Patel and Grbic [13] presented a realization of sinusoidally modulated reactance surface (SMRS), which was based on a metal strip grating on a grounded dielectric slab. The sinusoidal variation of the surface impedance was realized by varying the gap g between the metal strips as shown in Fig. 2.5(b). The surface impedance was mapped onto the gap $g(x)$ by using data from full-wave analysis (HFSS [16]). It was shown in [13] that this structure does provide a directive beam, which is associated with the (fast wave) $n = -1$ spatial harmonic.

More recently Martinez-Ros *et al.* [14] presented a half mode substrate integrated waveguide (SIW) based leaky-wave antenna. The width of the waveguide was modulated along the guiding length such that the leaky-wave harmonic can exist on the structure as shown in Fig. 2.5(c). Bai *et al.* [15] realized a sinusoidally modulated leaky-wave antenna based on an inset waveguide. The lower side of the dielectric part of the inset waveguide was modulated to realize sinusoidal impedance variation. An illustration of the realized structure is shown in Fig. 2.5(d).

In all the aforementioned antenna designs, only 1D variation (x direction variation) was considered. These antennas are capable of radiating a fan beam. In order to have a pencil beam radiation pattern 2D variation is required, which is discussed in the subsequent section.

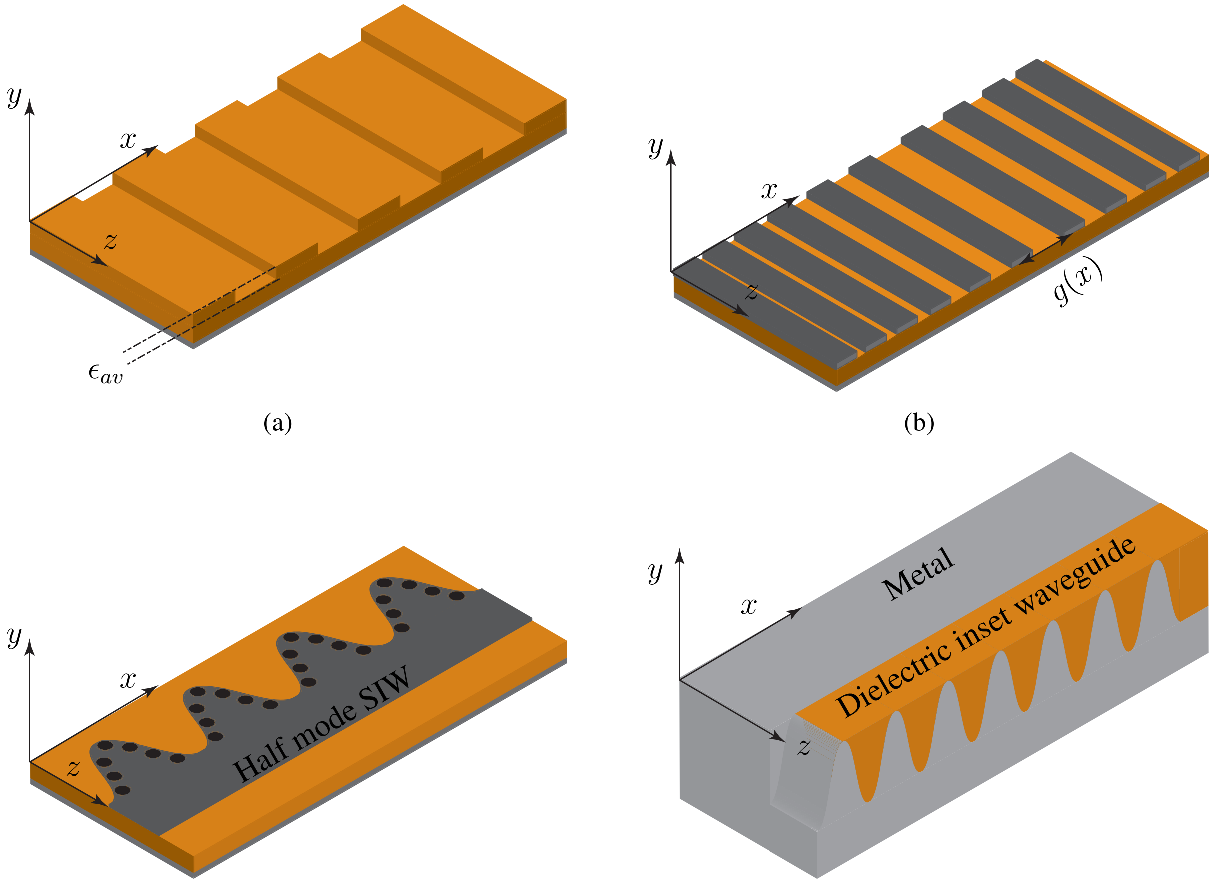

(a) (b) (c) (d)

Figure 2.5: a) Illustration of the structure considered by Schwering and Peng [12]. b) Illustration of sinusoidally modulated reactance surface (SMRS) realization by varying gap g in between the metal strips, considered by Patel and Grbic [13]. c) Illustration of half mode SIW based leaky-wave antenna as realized by Martinez-Ros *et al.* [14]. d) Illustration of sinusoidally modulated reactance realization with dielectric inset waveguide, as presented by Bai *et al.* [15].

2.4.1 Holographic Antenna

The holographic technique is used in optics [17][18]. The idea of holography has been used in microwaves to design antennas since 1970 [19]. The fundamental concept behind the holographic antenna is based on a surface wave interacting with the specific surface impedance Z_s that varies on the surface, which leads to the desired beam direction [20]. The holographic antenna is briefly reviewed here because it is a leaky-wave antenna, and it uses a modulated surface impedance to form a directive beam in a specific direction.

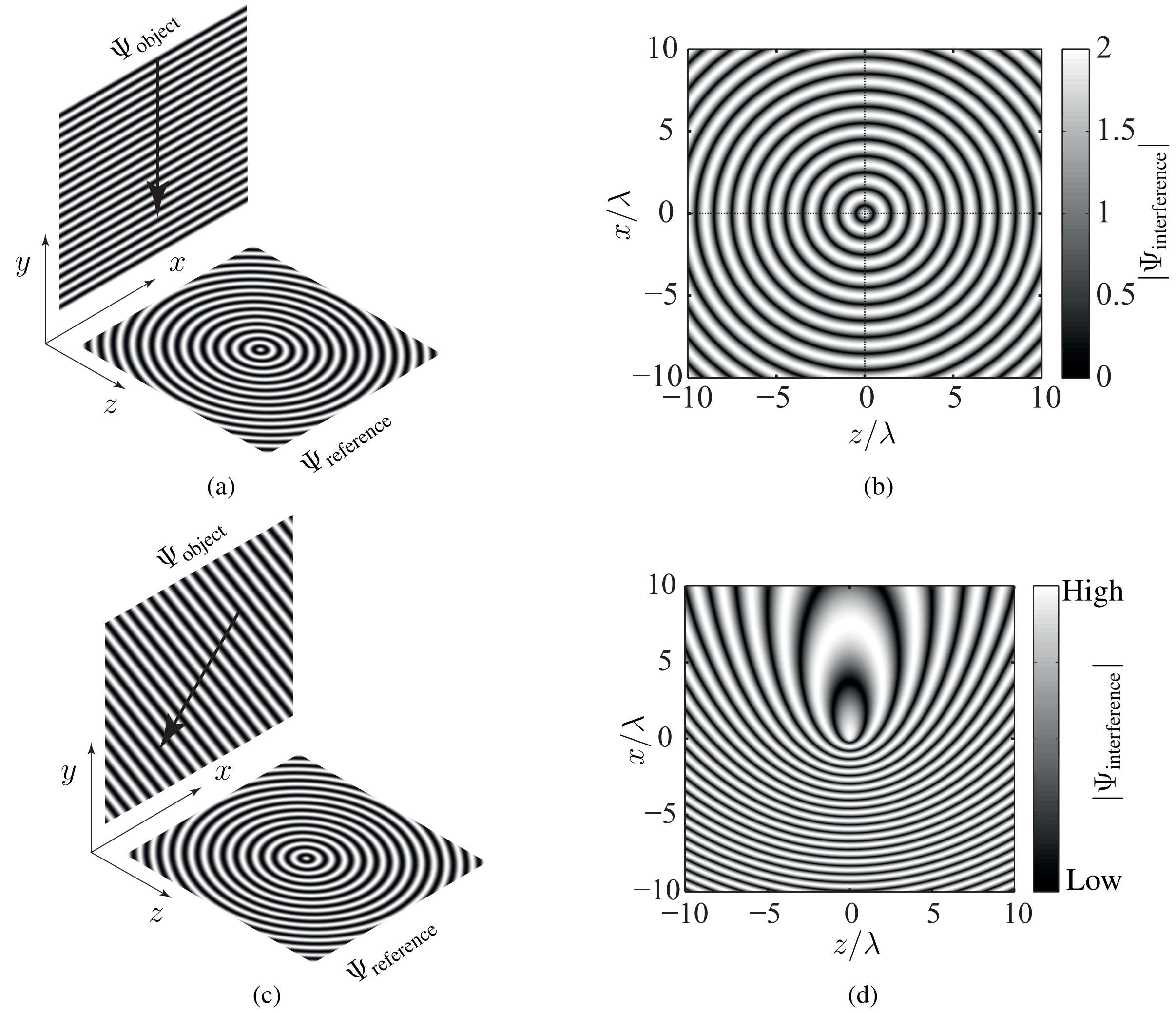

(a) (b) (c) (d)

Figure 2.6: a) Object wave with $\phi_i = 90°$ and reference wave in the x-z plane. b) Interference pattern. c) Object wave with $\phi_i = 60°$ and reference wave in the x-z plane. d) Interference pattern.

To see the concept of holography more clearly, consider a y-directed source in the x-z plane radiating a $\Psi_{\text{reference}}$ wave and a plane wave Ψ_{object} incident at $\phi_i = 90°$ (angle ϕ is with respect to x), as shown in Fig. 2.6(a). Mathematically we can express these two waves as

$$\Psi_{\text{reference}} = e^{-jkr} \tag{2.8}$$

$$\Psi_{\text{object}} = e^{-jk(x\cos\phi + y\sin\phi)} \tag{2.9}$$

where $r = \sqrt{x^2 + z^2}$ and k is the free space propagation constant. The corresponding interference

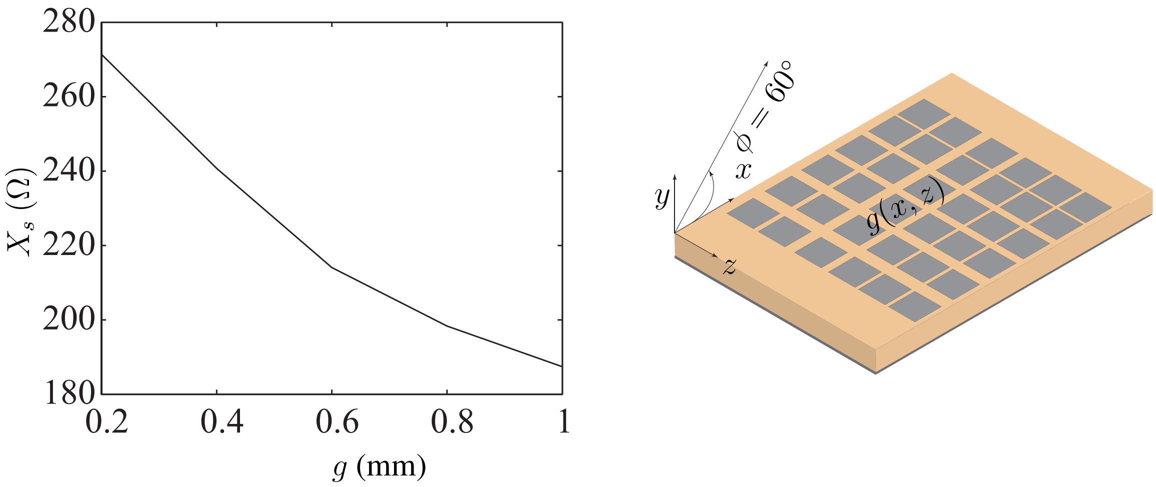

(a) (b)

Figure 2.7: a) Surface reactance as a function of patch gap g. b) Illustration of the realized structure which emulates the holographic surface impedance by patch gap variation $g(x, z)$.

pattern of these two waves in the x-z plane is

$$\Psi_{\text{interference}} = \Psi_{\text{reference}} + \Psi_{\text{object}} \tag{2.10}$$

and is shown in Fig. 2.6(b). By putting thin metal strips at the prescribed locations of zero field in the interference pattern Iizuka *et al.* [21] realized a holographic plate in 1975, which was later optimized by Sooriyadevan *et al.* [22].

The concept of holography is used by Fong *et al.* [23] to obtain a holographic antenna capable of radiating an off-broadside beam. As an example, consider an incident angle $\phi_i = 60°$ (angle ϕ is with respect to x) for Ψ_{object} and $\Psi_{\text{reference}}$ is in the x-z plane as shown in Fig. 2.6(c). The interference pattern of these two waves in the x-z plane is shown in Fig. 2.6(d). The corresponding holographic surface impedance can be realized by using sub-wavelength metallic patches on top of a grounded dielectric slab. Full-wave eigenmode analysis (HFSS [16]) can be used to compute the propagation constant across the unit cell for the surface wave mode. This was used by Fong *et al.* to compute the index of refraction n, which allows for the mapping of a given surface impedance onto the gap g between the patches which is shown in Fig. 2.7(a). An illustration of the realized structure that emulates surface impedance variation in Fig. 2.6(d) as function patch gap size $g(x, z)$ is shown in Fig. 2.7(b). Minatti *et al.* [24] realized a spirally varying surface impedance by varying the metallic patch size on top of a grounded dielectric slab. Pandi *et al.* [25] also presented surface impedance realization via metallic patches on a grounded dielectric slab. Podilchak *et al.* [26] modulated the width of a microstrip line periodically to realize a sinusoidal surface impedance modulation.

We employ the theory of a grounded dielectric slab (see [3], sec. 3.6.2), to map surface impedance onto the: 1) thickness of the grounded slab, 2) permittivity of the grounded slab. This in turn allows one to realize a given surface impedance modulation analytically, which is subsequently used to design leaky-wave antennas in Chapter 4.

Chapter 3

Impedance Boundary Condition (IBC)

The impenetrable IBC can be used to simplify an electromagnetic problem when the field inside the body is not needed. The study of an impenetrable impedance boundary was first presented by Leontovich [27] in 1948. The impenetrable impedance boundary condition is an exterior-only representation of an object, which is to say that the field inside the object is zero. The penetrable IBC (sheet impedance) is used for thin materials that cause both reflection and transmission (see [3], Sec. 2.6). For the penetrable IBC the field inside the thin object is not zero. All this to say that with the impenetrable IBC the object is opaque. The penetrable IBC (sheet impedance) models a thin object that is not opaque.

The surface impedance for the transmit problem T_x (when the source is very close to the impedance surface) is different from the receive problem R_x (when the source is far from the impedance. By using the complete rigorous Green's function solution for a grounded dielectric slab of infinite extent (see [3], sec. 12.6), we investigate the surface impedance variation as the excitation source location is changed.

Next, electric and magnetic coupled field integral equations are formulated for an impenetrable impedance strip of finite extent. Using the field symmetries for the flat strip geometry allows one to decouple these integral equation which can then be solved with MoM for the unknown equivalent currents. Subsequently, one can use these currents to study the radiation characteristics

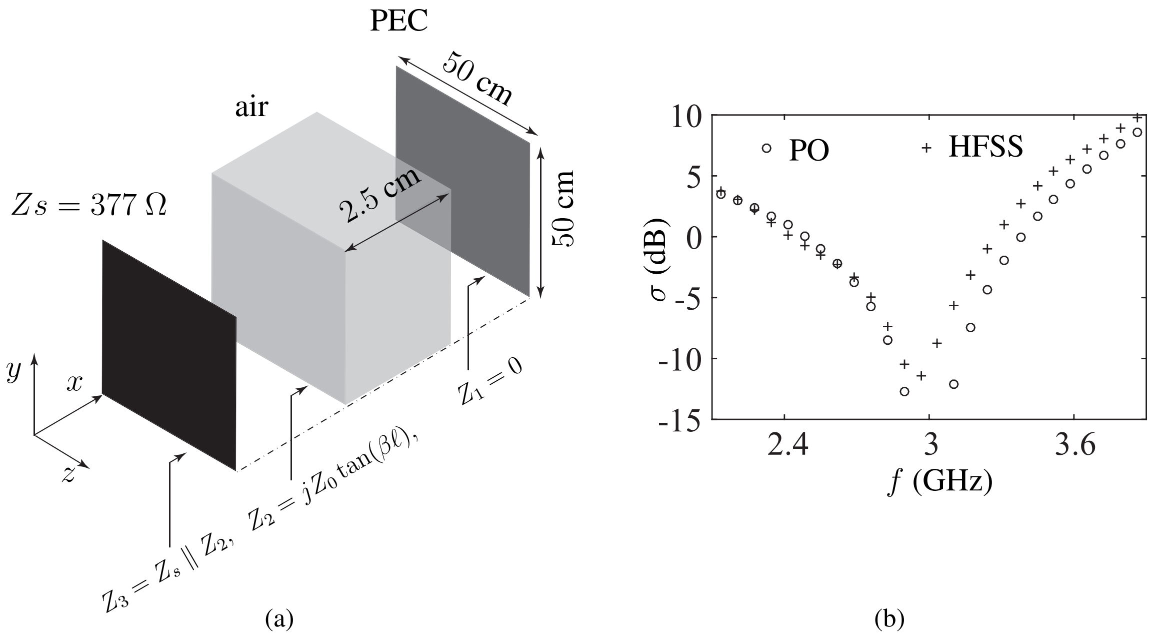

(a) (b)

Figure 3.1: a) Illustration of a 'space cloth'. b) Radar cross section computed with physical optics (PO) and HFSS (0 dB = 1 m^2).

of an arbitrary surface impedance with an arbitrary excitation.

3.1 Penetrable and Impenetrable IBC

Commercial electromagnetic solvers, such as HFSS [16], COMSOL [28] and FEKO [29] do offer IBC but they only account for penetrable IBC. This is commonly known as the "impedance sheet" approximation and is useful for finding the reflection and transmission by a thin material sheet. These solvers do not allow for an impenetrable boundary which is opaque (has zero transmission). Before considering a solution for the impenetrable case we will first illustrate the idea. Let us consider a simple problem of a Salisbury screen absorber, using a "space cloth" (see [3], Sec. 2.9) which is a resistive sheet of $377\ \Omega$ as shown in Fig. 3.1(a). The distance between the PEC plate and the resistive sheet is 2.5 cm, which is to say $\lambda/4$ at 3 GHz. This makes $Z_2 \to \infty$ which leads to $Z_3 = 377\ \Omega$ at 3 GHz, essentially making it a matched load to free space. For this problem one can compute the impedance as shown in Fig.3.1(a) which allow us to calculate the reflection coefficient Γ and radar cross section σ as (see [30], p. 316)

$$\Gamma = \frac{Z_3 - \eta}{Z_3 + \eta} \tag{3.1}$$

$$\sigma = \frac{4\pi A^2}{\lambda^2}|\Gamma|^2 \tag{3.2}$$

where A is the area of the sheet, and λ is the wavelength. This is the physical optics (PO) solution. The same problem can be solved with HFSS. The PO solution is compared with an HFSS solution in Fig.3.1(b), which precisely proves that HFSS solves for a penetrable impedance boundary. One also finds that with HFSS a $377\ \Omega$ sheet backed by a ground plane becomes a ground plane. This further illustrates that HFSS cannot handle an impenetrable IBC.

We are primarily interested in the impenetrable IBC, as it is an exterior-only representation and assumes the field inside the object to be zero. This simplifies the problem of an impedance strip by assuming the fields inside the strip to be zero. To make sense of the "inside the strip" we should give it some small non zero thickness, then take the limit as the thickness shrinks to zero. The MoM field solution outside the impedance strip is developed later in this chapter.

3.2 Transmit $\mathrm{T_x}$ and Receive $\mathrm{R_x}$ Problem

We now investigate how an IBC depends on the location of the source. Let us consider a simple problem of perfect electric conductor (PEC) at $y = 0$ as shown in Fig. 3.2(a). We will consider two situations that we call the transmit problem and receive problem. In the transmit problem $\mathrm{T_x}$ the source point (SP) is close to the PEC and the field point (FP) is far. In the receive problem $\mathrm{R_x}$ the source and field points are interchanged as shown in Fig. 3.2(a). By reciprocity the field at the field points in the two problems are the same. Furthermore, $E_{\text{tan}}^{\mathrm{T_x}}\big|_{y=0} = E_{\text{tan}}^{\mathrm{R_x}}\big|_{y=0} = 0$ in the two problems. However, $H_{\text{tan}}^{\mathrm{T_x}}\big|_{y=0} \neq H_{\text{tan}}^{\mathrm{R_x}}\big|_{y=0}$ (where $E_{\text{tan}}^{\mathrm{T_x}}$ is the tangential electric field in the transmit problem, with similar interpretation for the other terms). Uniqueness of the field solution is guaranteed if either E_{tan} or H_{tan} is specified (see [3], Sec. 4.4). For the problems considered in

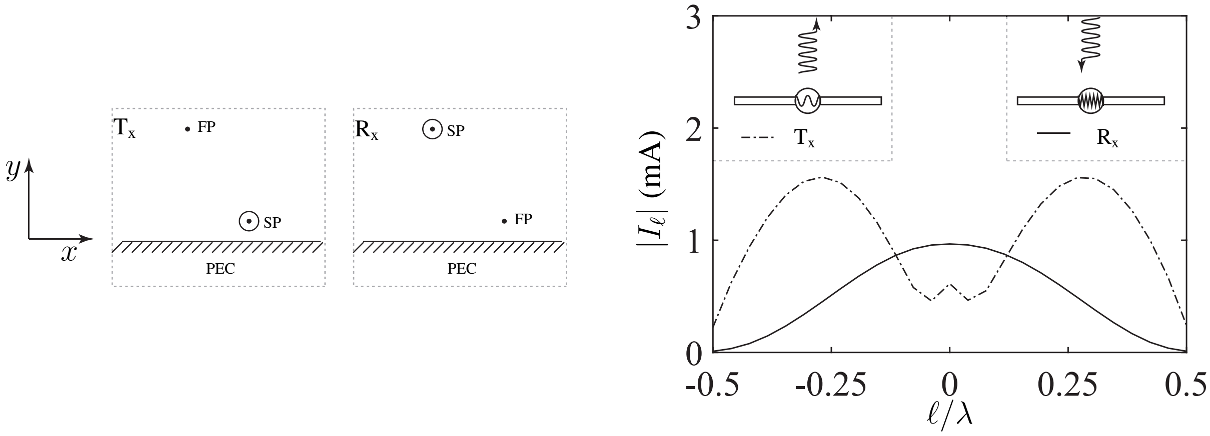

(a) (b)

Figure 3.2: a) Transmit $\mathrm{T_x}$ and receive $\mathrm{R_x}$ problem. b) Transmit $\mathrm{T_x}$ and receive $\mathrm{R_x}$ current on a one-wavelength dipole (computed with FEKO [29]).

Fig. 3.2(a), it is convenient for the field solution to use $E_{\text{tan}} = 0$. However, it conceals the fact that H_{tan} is different in the two problems.

To further illustrate this idea, consider the case of a one-wavelength dipole. The transmit $\mathrm{T_x}$ and receive $\mathrm{R_x}$ currents on the dipole are different, as shown in Fig. 3.2(b) (see [31], p. 242). In the $\mathrm{T_x}$ case 1 V delta gap is used which produces the $\mathrm{T_x}$ current. In the $\mathrm{R_x}$ case a $50\ \Omega$ load resistor is used, across which the power is dissipated. This shows that the transmit $\mathrm{T_x}$ and receive $\mathrm{R_x}$ are reciprocal problems but not equivalent problems. Since H_{tan} is related to the current it shows that the magnetic field boundary condition for the $\mathrm{T_x}$ and $\mathrm{R_x}$ cases are different.

3.2.1 Surface Wave and Plane Wave Impedance

We now consider a grounded dielectric slab, and examine how the impedance looking in to the air-dielectric boundary is affected by the type of illumination.

To begin, we note that plane wave (normal incidence) impedance is different from surface wave impedance. This stems from the idea that a surface wave (slow wave) propagates along a given surface and the field decays away from the surface. Reciprocally, a plane wave (normal incidence) illuminating a given surface can not excite a surface wave. To understand this concept clearly, let

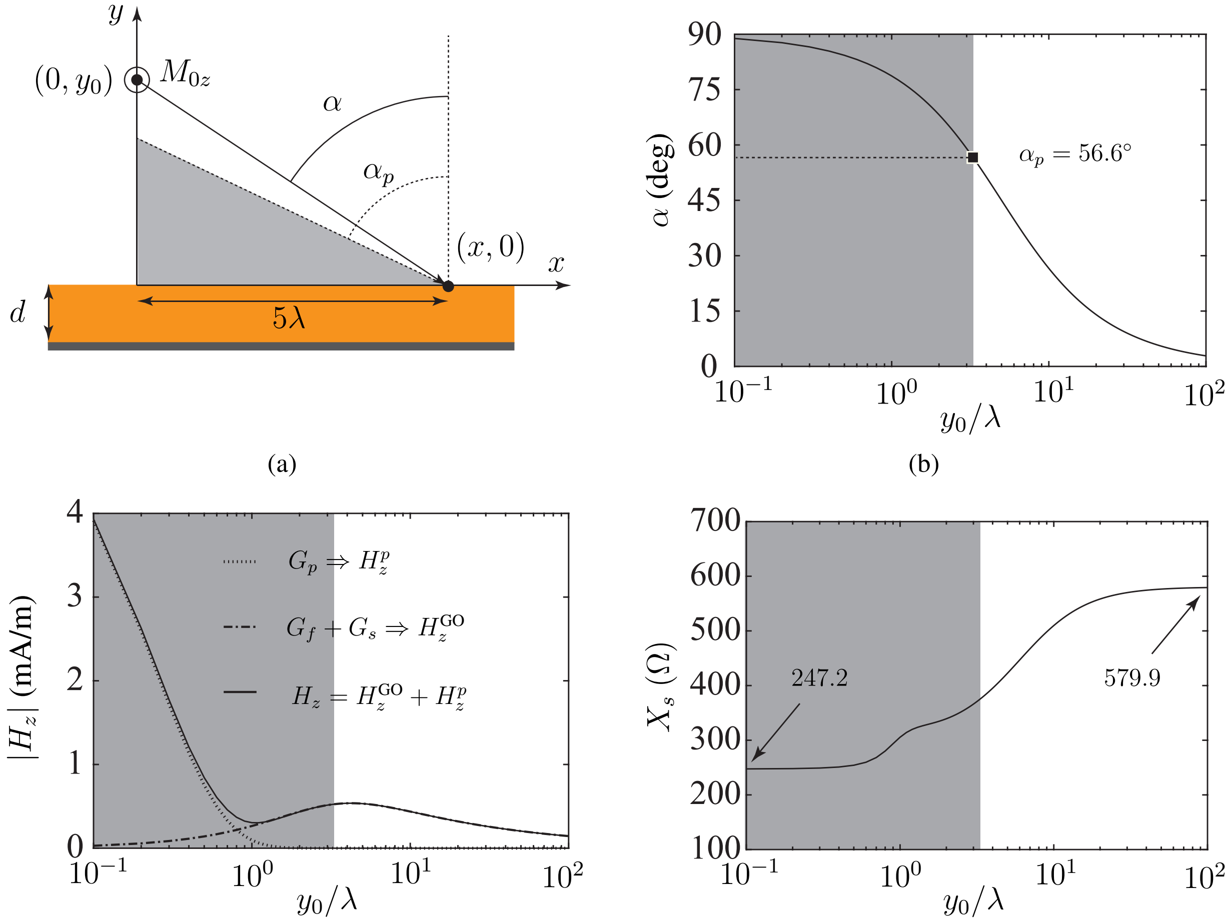

(a) (b) (c) (d)

Figure 3.3: a) Grounded dielectric slab with thickness $d = 0.1\lambda$ and $\epsilon_r = 4$, excited by a magnetic line source M_{0z}, x is treated as fixed and y_0 is a variable. b) α variation as a function of y_0. c) Magnetic field H_z solution at $(5\lambda, 0)$. d) Reactance variation as the source M_{0z} is moved along y direction.

us consider an example problem of an infinite grounded dielectric slab with thickness $d = 0.1\lambda$ (λ is free-space wavelength) and relative permittivity $\epsilon_r = 4$ as shown in Fig. 3.3(a), which can support a surface wave. This slab is excited by a magnetic line source M_{0z} located at $(0, y_0)$. The complete rigorous field solution for this problem is provided in the Appendix B. However, for the case considered here, we chose the field point $(x, 0)$ (where the fields are evaluated) to be at $(5\lambda, 0)$ as shown in Fig. 3.3(a). At this distance between the source point and the field point one can use the saddle point asymptotic approximation (see [3], p. 397) to evaluate the fields.

Moving the magnetic line source M_{0z} in Fig. 3.3(a) along the y coordinate changes the angle α.

In this discussion x is fixed and y_0 is varied. The variation of α versus y_0 is shown in Fig. 3.3(b). The shaded region is bounded by $\alpha_p = 56.6^\circ$. At this angle the steepest descent path (SDP) intercepts the surface wave pole w_p in the complex w plane (details are provided in Appendix B). If M_{0z} lies in the shaded region, the total field H_z will have the contribution from the space wave (continuous spectrum), which is called H_z^{GO} in Fig. 3.3(c), and from the surface wave (discrete spectrum) (see [3], Sec. 11.7), which is represented by H_z^p in the Fig. 3.3(c). On the other hand, if M_{0z} lies outside the shaded region only H_z^{GO} remains and surface wave H_z^p is not excited as shown in Fig. 3.3(c). It should be noted that if x is increased for a fixed y_0 then α will increase. Therefore decreasing y_0 or increasing x has the same effect.

H_z^{GO} has two parts: 1) the direct field contribution G_f from the source and 2) the reflected field contribution G_s from the slab as shown in Fig. 3.3(c); extensive details are provided in Appendix B. Knowing the total magnetic field H_z allows one to calculate the electric field as $\nabla \times \hat{z} H_z \Rightarrow E_x$, which can be used to compute the impedance $Z_s = E_x/H_z$ at the field point. The reactance variation at the field point $(5\lambda, 0)$ as the source M_{0z} is moved along the y coordinate is shown in Fig. 3.3(d).

Consider the source M_{0z} to be at $(0, 0.1\lambda)$, which corresponds to $\alpha \approx 90^\circ$ (grazing incidence) as shown in Fig. 3.3(b). In this case, the direct field part G_f cancels out with the reflected field part G_s, consequently $H_z^{\mathrm{GO}} \approx 0$, and only the surface wave part G_p remains which gives H_z^p as shown in Fig. 3.3(c).

The surface wave reactance for the grounded slab can be calculated as

$$X_s = \eta \frac{q_0}{k_1 d} = 247.2\,\Omega \tag{3.3}$$

where $\eta = 120\pi\ \Omega$, $d = 0.1\lambda$, $k_1 = 2\pi/\lambda$ and $q_0 = 0.412$ (see Fig. B.1(c) in Appendix B). We get the same reactance in Fig. 3.3(d) from the complete field solution, when we have grazing incidence. As in this case the source M_{0z} is very close to the slab surface, it may be called the transmit problem $\mathrm{T_x}$.

As a second case, consider the source M_{0z} to be located at $(0, 100\lambda)$. The corresponding angle is $\alpha \approx 0°$ (normal incidence) as shown in Fig. 3.3(b). In this case, the surface wave is not excited, which is to say $H_z^p = 0$. The only field contribution remaining is H_z^{GO} which is shown in Fig. 3.3(c).

For the normal incidence case, a transverse equivalent network (see [3], Sec. 2.8) approach can be used to calculate the surface reactance

$$X_s = Z_2 \tan(k_2 d) = 580.01\,\Omega \tag{3.4}$$

where $Z_2 = \sqrt{\mu_2/\epsilon_2},\ \mu_2 = \mu_0$, $\epsilon_2 = \epsilon_0\epsilon_r$ = the dielectric slab permittivity, and $k_2 = k_1\sqrt{\epsilon_r}$. The same reactance can be seen in the complete field solution in Fig. 3.3(d), when we have normal incidence. In this case the source M_{0z} is far from the slab surface, so it may be called the receive problem $\mathrm{R_x}$.

As illustrated in Fig. 3.3(d), the surface impedance of the grounded slab is strongly dependent on the location of the source M_{0z} relative to the slab. The surface wave reactance (3.3) ($\mathrm{T_x}$ case) is significantly different from the plane wave (normal incidence) reactance (3.4) ($\mathrm{R_x}$ case).

In order to further our understanding of the implications, let us consider an impedance boundary $Z_s = R_s + jX_s$ of infinite extent at $y = 0$ and it is excited by a magnetic line source M_{0z} located at $(0, 0.1\lambda)$ as shown in Fig. 3.4(a). For a grounded slab we have $R_s \neq 0$, however, $R_s << X_s$ for our case, so it is not included here.

The magnetic field H_z can be calculated as

$$H_z = -j\omega\epsilon_0 M_{0z} G \tag{3.5}$$

$$G = G_f + G_s + G_p. \tag{3.6}$$

Let us assume the field point (x, y) to be 5λ away, which allows us to use the saddle point asymp-

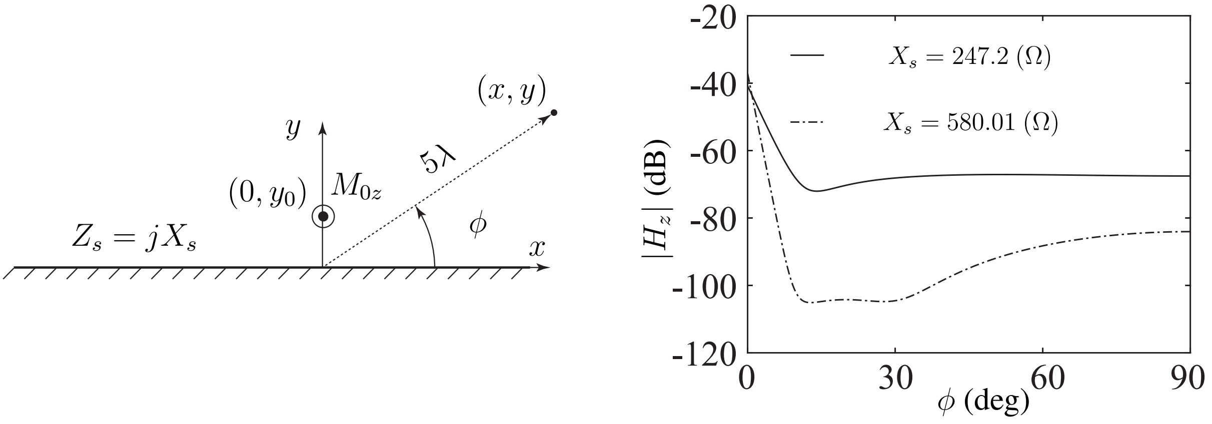

(a) (b)

Figure 3.4: a) Impedance boundary Z_s at $y = 0$ excited by a magnetic line source M_{0z}. b) $|H_z|$ for the impedance boundary using surface wave impedance (3.3) and plane wave impedance (3.4) (0 dB $= 1$ A/m).

totic approximation to evaluate the field (see [32], p. 555)

$$G_f \sim \frac{1}{j4}\sqrt{\frac{2}{\pi k \rho_0}} e^{-j(k\rho_0 - \pi/4)} \tag{3.7}$$

where $\rho_0 = \sqrt{(x - x_0)^2 + (y - y_0)^2}$ and $k = 2\pi/\lambda$. The reflected part is

$$G_s \sim \frac{1}{j4}\sqrt{\frac{2}{\pi k \rho}} e^{-j(k\rho - \pi/4)}\, \Gamma(k \sin\alpha) \tag{3.8}$$

where $\rho = \sqrt{(x - x_0)^2 + (y + y_0)^2}$. The magnetic field reflection coefficient is

$$\Gamma = \frac{\cos\alpha - \bar{Z}_s}{\cos\alpha + \bar{Z}_s}, \tag{3.9}$$

where $\alpha = \pi/2 - \phi$ (see Appendix B), $\bar{Z}_s = Z_s/\eta$ and $\eta = 377\ \Omega$ (see [3], problem 12.5). The surface wave contribution is

$$G_p = \cot w_p e^{-jk\rho\cos(w_p - \alpha)} U(\alpha - \alpha_p) \tag{3.10}$$

where $w_p = \pi/2 + j\sinh^{-1}(X_s/\eta)$.

Using (3.5) allows one to compute H_z for the surface wave impedance (3.3) (the correct $\mathrm{T_x}$ case) and plane wave impedance (3.4) (the incorrect $\mathrm{R_x}$ case), which is shown in Fig. 3.4(b). The discrepancy shows that using the surface reactance $X_s = 580\ \Omega$ derived from plane wave illumination is incorrect for a transmitting antenna.

3.2.2 Near Source Surface Impedance Variation

We saw that the surface impedance depends on the type of illumination. To illustrate this further, we now consider a grounded dielectric slab with $d = 0.1\lambda$ and $\epsilon_r = 4$ excited by a magnetic line source M_{0z} which is close to the surface of the slab as shown in Fig. 3.5(a). Let us compute the $H_z(x, 0)$ using the exact solution in Appendix B. Close to the source, the asymptotic approximation for the reflected field G_s is inaccurate. This requires the Sommerfeld integral (B.4) to be evaluated numerically in the complex w plane. In order to avoid the field singularity just underneath the line source we chose the source location to be slightly above the slab and choosing $y_0 = 0.1583\lambda$ makes the fields add up in phase at $\phi = 90^\circ$.

The complete $H_z(x, 0)$ has three contributions: 1) the direct source field H_z^f, 2) the reflected field from the slab H_z^s and 3) the surface wave field or "pole wave" H_z^p, which are shown in Fig. 3.5(b). Taking $\nabla \times \hat{z}H_z$ allows one to compute $E_x(x, 0)$, see (B.23). The complete $E_x(x, 0)$ also has the three field contributions, which are shown in Fig. 3.5(c).

Knowing the exact fields along the surface of the slab allows us to compute the exact impedance, which is $Z_s = E_x/H_z$ and is shown in Fig. 3.5(d). The reactance (imaginary part of the impedance) X_s is spatially varying near the source and away from the source the exact reactance becomes equal to the surface wave reactance X_p. The positive resistance R_s (real part of the impedance) variation near the source region signifies power flow in the $-y$-direction, which is into the slab, while a negative sign signifies power flow in the $+y$-direction, which is out of the slab. Away from the source region (about 1λ), the resistance R_s becomes zero, which means there is no power flow in the y direction.

The same 2D problem in Fig. 3.5(a) can be solved with COMSOL [28] by using a line source

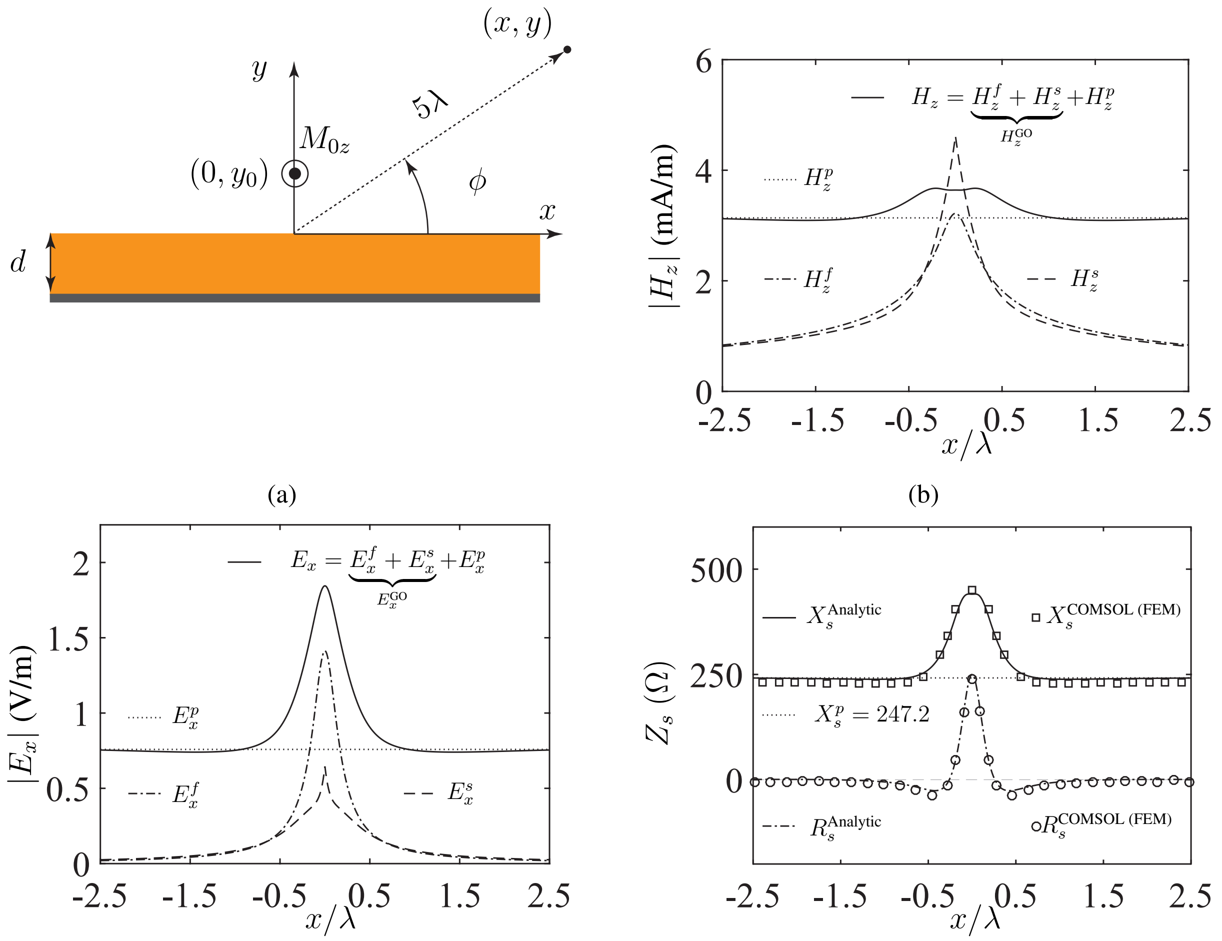

(a) (b)

(c) (d)

Figure 3.5: a) Grounded dielectric slab with thickness $d = 0.1\lambda$ and $\epsilon_r = 4$, excited by a magnetic line source M_{0z}. b) $H_z(x,0)$ along the surface of the dielectric slab, where H_z^f is free space, H_z^s is the reflected and H_z^p is the surface wave part. c) $E_x(x,0)$ along the surface of the dielectric slab, where E_x^f is free space, E_x^s is the reflected and E_x^p is the surface wave part. d) Spatial impedance variation $Z_s(x) = E_x/H_z$.

excitation and absorbing boundary condition. The impedance from COMSOL solver is in good agreement with the exact solution. Both solutions show similar spatial surface impedance variation near the source region.

To see the difference between the transmit T_x and R_x impedance, let us consider the same problem of a grounded slab excited with a magnetic line M_{0z} at $(0, y_0)$ as shown in Fig. 3.6(a). In the transmit problem T_x we assume $y_0 = 0.1538\lambda$ and in the receive problem R_x $y_0 = 100\lambda$ is assumed. Using the saddle point asymptotic approximation (see (B.9)) for the R_x case and solving

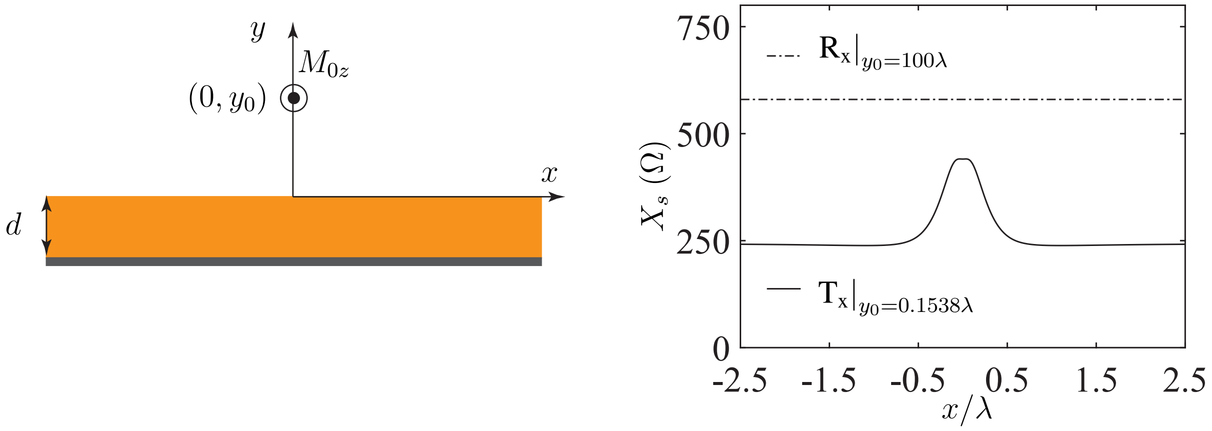

(a) (b)

Figure 3.6: a) Grounded dielectric slab with thickness $d = 0.1\lambda$ and $\epsilon_r = 4$, excited by a magnetic line source M_{0z}. b) Transmit $\mathrm{T_x}$ and receive $\mathrm{R_x}$ surface reactance for the M_{0z} excited grounded slab shown in Fig. 3.6(a).

the Sommerfeld integral along the Z-path in the w plane (see Appendix B) for the $\mathrm{T_x}$ case allows one to compute the reactance which is shown in Fig. 3.6(b). The $\mathrm{T_x}$ reactance is significantly different from the $\mathrm{R_x}$ reactance. Furthermore, in the transmit problem $\mathrm{T_x}$ the surface reactance varies spatially close to the source. The R_s for the $\mathrm{T_x}$ case is shown in Fig. 3.5(d) and $R_s = 0$ for the $\mathrm{R_x}$ case.

3.3 IBC with $Z_s(x)$ on Infinite Slab

In order for an impedance boundary to accurately represent the true transmit $\mathrm{T_x}$ grounded slab problem, the spatial surface impedance variation has to be accounted for. Let us consider an impedance boundary at $y = 0$ which varies along x as shown in Fig. 3.7(a). Due to the surface impedance spatial variation there is no exact Green's function. However, we can use the true electric and magnetic fields, shown in Fig. 3.5 (c) and (b) respectively, with free space Green's functions to solve an equivalent problem with electric $J_x(x)$ and magnetic $M_z(x)$ currents as shown in Fig. 3.7(b). The radiated magnetic field for this equivalent problem can be expressed as (see [3],

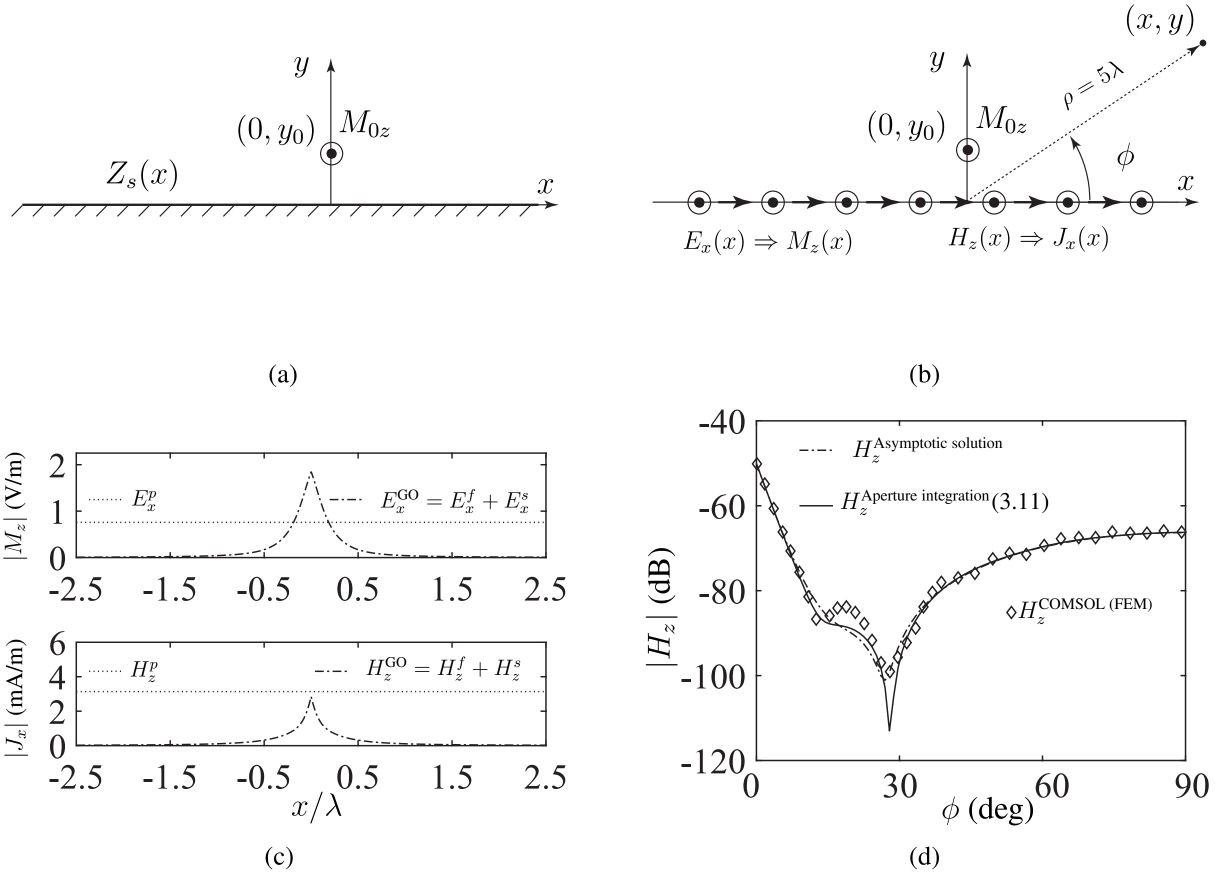

Figure 3.7: a) Impedance boundary $Z_s(x)$ at $y = 0$ excited by a magnetic line source M_{0z}. b) Equivalent electric $J_x(x)$ and magnetic current $M_z(x)$. c) Aperture GO and surface wave fields. d) Radiated magnetic field H_z (0 dB = 1 A/m).

p. 159)

$$H_z = M_{0z} G_m(kR) + \underbrace{\underbrace{\int_{-\infty}^{+\infty} M_z(x') G_m(kR)\, dx'}_{H_z(M_z)} + \underbrace{\int_{-\infty}^{+\infty} J_x(x') G_e(kR)\, dx'}_{H_z(J_x)}}_{H_z(M_z, J_x)} \tag{3.11}$$

where

$$G_m(kR) = \frac{-k}{4\eta} H_0^{(2)}(kR)$$
$$G_e(kR) = \frac{-jk}{4} H_1^{(2)}(kR)\, \frac{y}{R}$$

and $k = 2\pi/\lambda$, $R = |\boldsymbol{\rho} - \boldsymbol{\rho}'|$.

The first term on the right hand side of (3.11) represents the incident field due to the excitation source M_{0z}. The other two integral terms provide the radiation from the aperture electric and magnetic fields, respectively. In order to evaluate the integrals in (3.11), one can express $H_z(M_z, J_x)$ in terms of aperture electric and magnetic fields as

$$H_z(M_z, J_x) = \int_{-\infty}^{+\infty} E_x(x')G_m(kR)\, dx' + \int_{-\infty}^{+\infty} H_z(x')G_e(kR)\, dx'. \tag{3.12}$$

The aperture electric E_x and magnetic H_z field for the grounded slab considered in the previous section can be decomposed into GO fields and surface wave fields (p represents the pole wave), as shown in Fig. 3.7(c). This allows (3.12) to be written as

$$H_z(M_z, J_x) = \int_{-\infty}^{+\infty} \left(E_x^{\mathrm{GO}}(x') + E_x^{p}(x')\right) G_m(kR)\, dx' + \int_{-\infty}^{+\infty} \left(H_z^{\mathrm{GO}}(x') + H_z^{p}(x')\right) G_e(kR)\, dx'. \tag{3.13}$$

As can be seen in Fig. 3.7(c), the GO field becomes zero when $|x| \geq 2\lambda$. This eliminates the need of evaluating the infinite integral over the GO field part, hence leading to

$$\begin{aligned} H_z(M_z, J_x) = &\int_{-2\lambda}^{+2\lambda} \left(E_x^{\mathrm{GO}}(x')\, G_m(kR) + H_z^{\mathrm{GO}}(x')\, G_e(kR)\right) dx' \\ &+ \int_{-\infty}^{+\infty} \left(E_x^{p}(x')\, G_m(kR) + H_z^{p}(x')\, G_e(kR)\right) dx'. \end{aligned} \tag{3.14}$$

The first integral on the right hand side of (3.14) can be evaluated numerically by employing the trapezoidal rule with $\Delta = 0.01\lambda$ (see [33], p. 192). The second integral in (3.14) signifies radiation from the surface wave fields over an infinite aperture. This can be solved by taking the Fourier transform of the aperture field and solving the integral via the stationary phase method (see [3], Sec. 5.5); details are provided in Appendix C. One can write (3.14) as

$$H_z(M_z, J_x) = \Delta \sum_{n=1}^{N} \left[E_x^{\mathrm{GO}}(x_n)\, G_m(kR_n) + H_z^{\mathrm{GO}}(x_n)\, G_e(kR_n)\right] + H_z^{\mathrm{swr}} \tag{3.15}$$

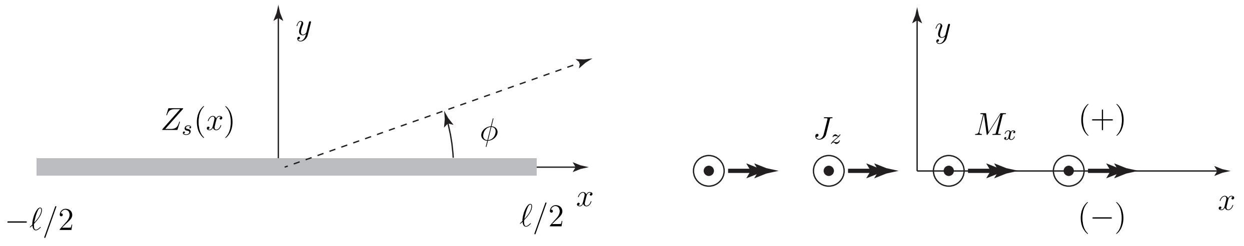

(a) (b)

Figure 3.8: a) Impedance strip excited by a magnetic point source. b) Equivalent electric J_z and magnetic M_x currents.

where $R_n = \sqrt{(x - x_n)^2 + y^2}$ and the surface wave radiation part H_z^{swr} is derived in Appendix C (see (C.25)).

Let us consider the field point (x, y) to be at 5λ as shown in Fig. 3.7(b). At this distance the field solution from the IBC problem in Fig. 3.7(a) can be compared with the asymptotic solution (see Appendix B) for the true grounded slab problem of Fig. 3.5(a). The magnetic field H_z from the two solutions are in good agreement as shown in Fig. 3.7(d). In order to further verify the solution, one can numerically solve the true 2D slab problem of Fig. 3.5(a) with COMSOL, which also gives a very similar H_z, as shown in Fig. 3.7(d). This precisely shows that for the IBC to accurately represent the true problem, surface impedance variation near the source region has to be accounted for.

3.4 $Z_s(x)$ on Finite IBC Strip Integral Equations

We now develop the integral equation MoM solution for the 2D problem of an impenetrable impedance strip of length ℓ in the x-z plane, as shown in Fig. 3.8(a). This work is reported in [34] and [35]. The impedance $Z_s(x)$ is an arbitrary function of x. The equivalence principle (see [3], p. 147) is used to replace the original strip by an equivalent electric current J_z and magnetic current M_x as shown in Fig. 3.8(b). The presence of J_z is associated with the discontinuity in H_x and similarly, the presence of M_x is associated with the discontinuity in E_z, as we move from the top $(+)$ side of the strip to the bottom $(-)$ side of the strip.

The IBC on the top $(+)$ and bottom $(-)$ sides of the strip are as follows:

$$E_z^{\pm} = Z_s^{\pm}(x) J_z^{\pm}(x) \tag{3.16}$$

$$H_x^{\pm} = Y_s^{\pm}(x) M_x^{\pm}(x). \tag{3.17}$$

We will assume that both sides have the same impedance function so that $Z_s^+(x) = Z_s^-(x) = Z_s(x)$ and likewise for $Y_s(x)$, where $Y_s(x) = 1/Z_s(x)$. This leads to the following coupled field equations, which can be decoupled by making use of field symmetries;

$$E_z^i(x) + E_z^{s+}(J_z) + E_z^{s+}(M_x) = Z_s(x) J_z(x)^+ \ \ (+) \tag{3.18}$$

$$E_z^i(x) + E_z^{s-}(J_z) + E_z^{s-}(M_x) = Z_s(x) J_z(x)^- \ \ (-) \tag{3.19}$$

$$H_x^i(x) + H_x^{s+}(J_z) + H_x^{s+}(M_x) = Y_s(x) M_x(x)^+ \ (+) \tag{3.20}$$

$$H_x^i(x) + H_x^{s-}(J_z) + H_x^{s-}(M_x) = Y_s(x) M_x(x)^- \ (-) \tag{3.21}$$

Here, $E_z^i(x)$ and $H_x^i(x)$ are the incident tangential fields at $y = 0$. The incident field is dependent on the choice of excitation source and will be discussed in the subsequent sections. In this notation,

$$E_z^{s+}(J_z) = E_z^{s+} \text{ due to } J_z \text{ on the } (+) \text{ side}$$

$$H_x^{s-}(M_x) = H_x^{s-} \text{ due to } M_x \text{ on the } (-) \text{ side}$$

with similar interpretation for the other terms. The fields at $y = 0^+$ and $y = 0^-$ have the following symmetries with respect to $y = 0$

$$E_z^{s+}(J_z) = E_z^{s-}(J_z) \qquad \text{even symmetric} \tag{3.22}$$

$$E_z^{s+}(M_x) = -E_z^{s-}(M_x) \ \ \text{odd symmetric} \tag{3.23}$$

$$H_x^{s+}(M_x) = H_x^{s-}(M_x) \qquad \text{even symmetric} \tag{3.24}$$

$$H_x^{s+}(J_z) = -H_x^{s-}(J_z) \quad \text{odd symmetric.} \tag{3.25}$$

In Fig.3.8(b), the top and bottom currents of the free-space equivalent have merged so that $J_z(x) = J_z(x)^+ + J_z(x)^-$ and $M_x(x) = M_x(x)^+ + M_x(x)^-$. Adding (3.18) and (3.19) and using the symmetry relations (3.22) and (3.23) leads to (3.26). Similarly adding (3.20) and (3.21) with (3.24) and (3.25) gives (3.27):

$$E_z^i(x) + E_z^{s+}(J_z) = \frac{1}{2} Z_s(x) J_z(x) \tag{3.26}$$

$$H_x^i(x) + H_x^{s+}(M_x) = \frac{1}{2} Y_s(x) M_x(x). \tag{3.27}$$

These two decoupled equations can be solved for $J_z(x)$ and $M_x(x)$ using the MoM [36].

3.4.1 MoM Solution

We can rewrite the decoupled electric field (3.26) and magnetic field (3.27) integral equations in the following way, which makes them conducive to be used with MoM. This work is reported in [35] [34]:

$$E_z^i(x) = \frac{Z_s(x)}{2} J_z(x) + \int_{-\ell/2}^{\ell/2} J_z(x') G_e(x, x') dx' \tag{3.28}$$

$$H_x^i(x) = \frac{Y_s(x)}{2} M_x(x) + \int_{-\ell/2}^{\ell/2} M_x(x') G_m(x, x') dx'. \tag{3.29}$$

The integral equations can be solved by using pulse basis functions and point matching. The currents are expressed as a sum of N unit pulses $p(x - x_n)$ centered at $x = x_n$ and width Δ so that

$$J_z(x) = \sum_{n=1}^{N} I_n p(x - x_n);\ M_x(x) = \sum_{n=1}^{N} M_n p(x - x_n).$$

The pulses are on the top and bottom surfaces with $N/2$ pulses on each surface; for convenience N is assumed to be even. G_e and G_m are the electric and magnetic free space Green's functions

$$\begin{aligned} G_e(x, x') &= \frac{k\eta}{4} H_0^{(2)}(k|x - x'|) \\ G_m(x, x') &= \frac{k}{4\eta} \frac{H_1^{(2)}(k|x - x'|)}{k|x - x'|}. \end{aligned}$$

Enforcing (3.28) at the match points $x = x_m$ leads to a matrix equation $\mathbf{V} = \mathbf{ZI}$ with a column vector $\mathbf{V}$ having elements $V_m = E_z^i(x_m)$ and an impedance matrix with elements

$$Z_{mn} = \frac{Z_s(x_m)\delta_{mn}}{2} + \int_{x_n - \Delta/2}^{x_n + \Delta/2} G_e(x_m, x')dx' \tag{3.30}$$

in which δ_{mn} is the Kronecker delta. This can be solved for the electric current $\mathbf{I}$ having elements I_n. Similarly, (3.29) is written as $\mathbf{I} = \mathbf{YV}$ with a column vector $\mathbf{I}$ having elements $I_m = H_x^i(x_m)$ and an admittance matrix with elements

$$Y_{mn} = \frac{Y_s(x_m)\delta_{mn}}{2} + \int_{x_n - \Delta/2}^{x_n + \Delta/2} G_m(x_m, x')dx' \tag{3.31}$$

which can be solved for the magnetic current $\mathbf{V}$ with elements M_n. When $m = n$ the self terms Z_{mm} and Y_{mm} involve singular integrands; these are evaluated in Appendix D.

3.4.2 Plane Wave Excitation

In order to test the formulation developed in the preceding section, we can solve a simple test problem. Consider the impedance strip in Fig. 3.8(a) to have a constant impenetrable impedance of $Z_s = 377\ \Omega$ and $\ell = 5\lambda$. The impedance strip is illuminated by a TM (transverse magnetic H_x) plane wave traveling in the $-y$ direction ($\phi_i = 90°$). For this test we use geometrical optics (GO)

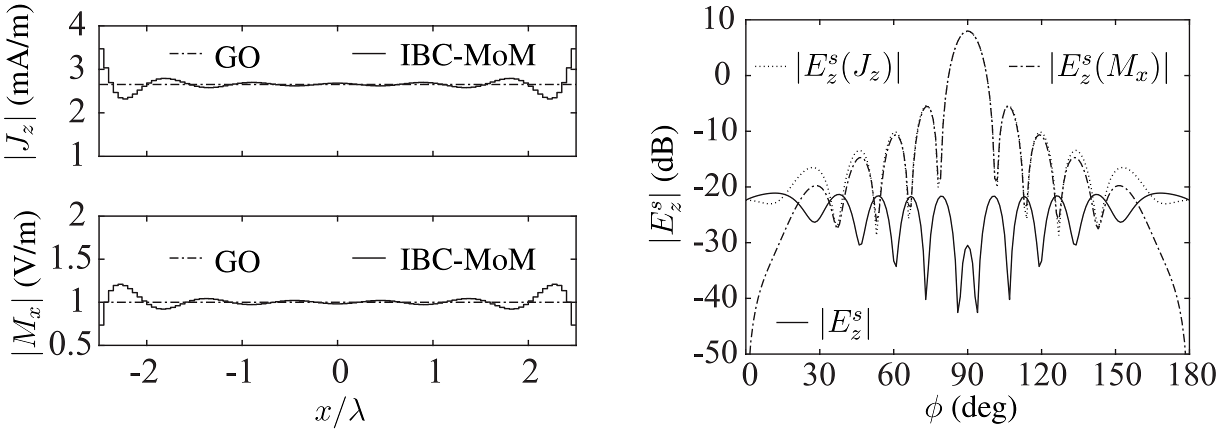

(a) (b)

Figure 3.9: a) Surface current computed via MoM and compared with GO for $Z_s = 377\ \Omega$ and plane wave excitation. b) Far field radiation pattern for the MoM currents (0 dB= 1 V/m).

to approximately compute the currents as

$$J_z^{(\mathrm{GO})} = \frac{1}{\eta}(1 + \Gamma_m) \tag{3.32}$$

$$M_x^{(\mathrm{GO})} = 1 + \Gamma_e \tag{3.33}$$

where $\Gamma_e = (Z_s - \eta)/(Z_s + \eta) = -\Gamma_m$ and $\eta = 377\ \Omega$. $\Gamma_{e,m}$ are the reflection coefficients for the electric and magnetic field. GO assumes the $H_{\text{tan}} \approx 0$ and $E_{\text{tan}} \approx 0$ on the bottom side $(-)$ or the shadow side of the strip which is, strictly speaking, not accurate due the finite extent of the strip the in x direction (see [3], p.147). On the lit side edge diffractions that contribute to the J_z and M_x are ignored.

Using $Z_s = 377\ \Omega$ in the integral equations (3.28), (3.29) and solving these via MoM allows one to calculate the currents, which are compared with GO currents in Fig. 3.9(a). The agreement validates the MoM procedure. If we take the ratio of the IBC-MoM currents as $Z_s = M_x/J_z$, using the complex values of M_x and J_z, we obtain the expected 377 Ω for all x.

Furthermore, we can compute the far field radiation pattern from the computed MoM currents as (see [3], problem 6.1)

$$E_z^s(J_z) = -e^{j\pi/4}\,\eta\,\Delta\sqrt{\frac{k}{8\pi}}\sum_{n=1}^{N} I_n\, e^{jkx_n\cos\phi}\,\frac{e^{-jk\rho}}{\sqrt{\rho}} \tag{3.34}$$

$$E_z^s(M_x) = -e^{j\pi/4}\,\Delta\sqrt{\frac{k}{8\pi}}\,\sin\phi\sum_{n=1}^{N} M_n\, e^{jkx_n\cos\phi}\,\frac{e^{-jk\rho}}{\sqrt{\rho}} \tag{3.35}$$

$$E_z^s = E_z^s(J_z) + E_z^s(M_x) \tag{3.36}$$

which is shown in Fig. 3.9(b). As the surface impedance was chosen to be $Z_s = 377\ \Omega$ which is matched to free space impedance, the electric field due to J_z cancels out with the electric field due to M_x. The resulting total electric field E_z^s remains minuscule and is shown in Fig. 3.9(b).

3.4.3 Huygens Source Excitation

As a second test case let us change the excitation. Consider a 2D problem of an impenetrable impedance strip excited by sources located at (x_0, y_0) as shown in Fig. 3.10(a). The strip is in the x-z plane and the far field angle ϕ is with respect to x. Ideally, a well-designed source should excite the guided mode but otherwise produce little or no additional, or "spurious" radiation. This is accomplished with a Huygens source, which has an electric line source and a magnetic line dipole that are related by $\eta J_{0z} = M_{0x}$, where $\eta = 120\pi\ \Omega$. Then, the radiation by J_{0z} and M_{0x} adds in the $-y$ direction and cancel in the $+y$ direction (see Appendix D). $Z_s(x)$ can be an arbitrary function of x.

The incident field due to the Huygens source located at $(x_0, 0)$ can be expressed as

$$E_z^i(x) = E_z(J_{0z}) + E_z(M_{0x}) \tag{3.37}$$

$$H_x^i(x) = H_x(M_{0x}) + H_x(J_{0z}) \tag{3.38}$$

where $E_z(J_{0z})$ is $E_z(x)$ due to J_{0z}, with similar interpretations for the other terms. Detailed expressions for these quantities are provided in Appendix D.

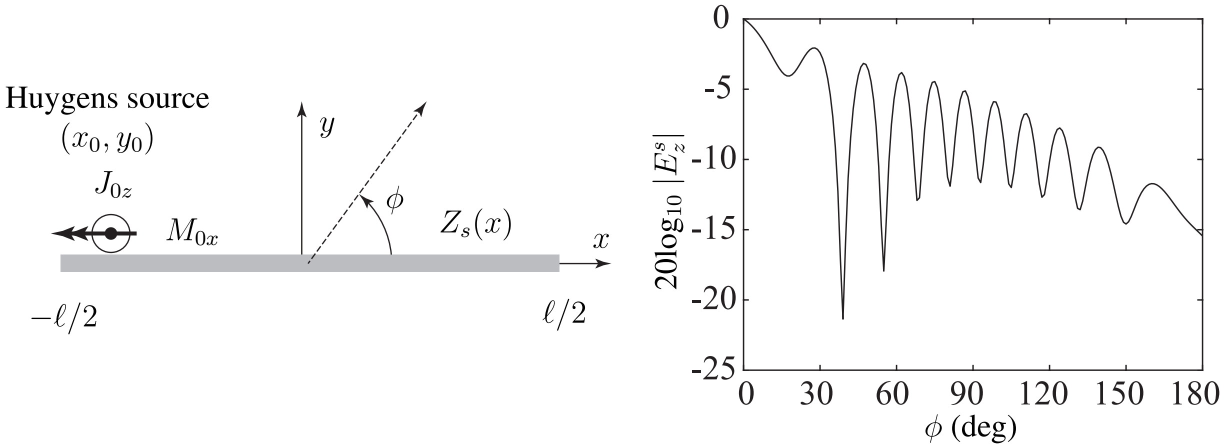

(a)

(b)

Figure 3.10: a) Impenetrable impedance strip excited by a Huygens point source [35]. b) Normalized scattered far field pattern calculated via MoM for the impedance strip in Fig.3.10(a) with $Z_s = -j1.2\eta$ Ω and $\ell = 5\lambda$ (0 dB = 1 V/m).

As a test example let us consider a constant reactance $Z_s = jX_s$ for the strip of $\ell = 5\lambda$ in Fig. 3.10(a). For the polarization considered here, the surface has to be capacitive in order to support a surface wave, which is to say $X_s < 0$ (see [37], p. 170) . From Oliner and Hessel [8] we know that for a constant reactance, the propagation constant is

$$k_x = k\sqrt{1 + (X_s/\eta)^2} \Rightarrow k_x > k \Rightarrow \text{ slow wave}$$

where $\eta = 377$ Ω. Due the finite extent of the impedance strip in the x direction, end fire radiation is expected for this slow wave.

Using $Z_s = -j1.2\eta$ and (3.37), (3.38) for the incident fields in the integral equations (3.28), (3.29) and solving these via the MoM allows one to calculate the currents, which can then be substituted in (3.34), (3.35) and (3.36) to calculate the far field radiation pattern. The radiation pattern in Fig. 3.10(b) shows the expected end-fire beam ($\phi = 0°$).

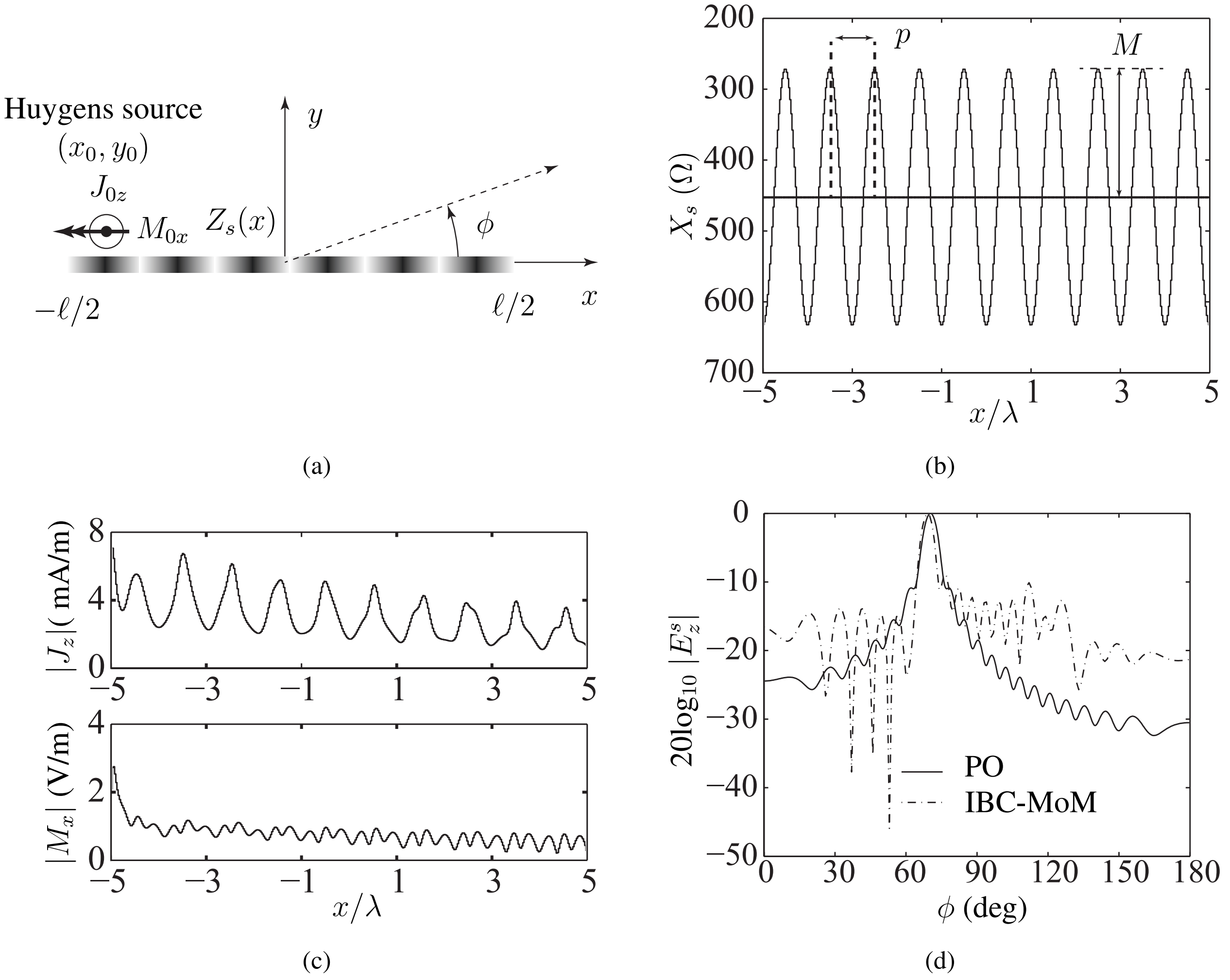

Figure 3.11: a) Sinusoidally modulated reactance strip excited by Huygen source of $\ell = 10\lambda$ [34]. b) Sinusoidally modulated reactance profile with $M = 0.4$, $p = \lambda$, and $X_s = 1.2\eta$ [34]. c) $|J_z(x)|$ and $|M_x(x)|$ calculated via MoM [34]. d) Normalized radiated field $|E_z^s|$ [34].

3.4.4 Sinusoidally Modulated Reactance Strip

Let us consider a sinusoidally modulated reactance strip excited by a Huygens source as shown in Fig. 3.11(a). Mathematically we can express the modulated reactance as

$$Z_s(x) = jX_{av}\left[1 + M\cos\left(\frac{2\pi}{p}x\right)\right] \tag{3.39}$$

where X_{av} is the average reactance, M is the modulation index and p is the period. As an example, let us consider $M = 0.4$, $p = 1\lambda$ and $X_s = 1.2\eta$ Ω. The plot of (3.39) with the aforementioned parameters is shown in Fig. 3.11(b). Using $Z_s(x)$ from (3.39) and incident fields (3.37), (3.38) in the integral equations (3.28), (3.29) and solving these via the MoM allows one to calculate the currents. The magnitudes of the IBC-MoM $J_z(x)$ and $M_x(x)$ are shown in Fig. 3.11(c). The currents suggest the existence of the leaky-wave harmonic, which is evident by the decay of the currents as we move along the x direction. If we take the ratio of the complex IBC-MoM currents as $Z_s(x) = M_x/J_z$, we obtain the specified sinusoidal reactance. Using these currents in (3.34), (3.35) and (3.36) allows one to calculate the far field pattern, which is called IBC-MoM solution in Fig. 3.11(d).

From Oliner and Hessel's [8] solution (see Chapter 2) we can find $k_x = \beta_n - j\alpha$ for the impedance expressed by (A.8). Using this k_x, one can assume an aperture field distribution of the form $e^{-jk_x x}$ and evaluate a radiation integral with $\ell = 10\lambda$ to find an approximate radiation pattern for the leaky-wave harmonic, which is called the physical optics (PO) solution in Fig.3.11(d). Note that Oliner-Hessel theory gives k_x and PO provides the approximate radiation pattern for a finite-length antenna.

The IBC-MoM solution agrees with the PO solution in terms of the beam angle which is $\phi \approx 70^\circ$ and 3 dB beamwidth which is about 6.2°. However, PO is an approximate solution as it does not account for more subtle effects such as a negative-x travelling reflected wave in the radiating aperture. But, the IBC-MoM solution does account for a negative-x travelling reflected wave, the radiation from which can be seen by the peak at $\phi \approx 110^\circ$ in the IBC-MoM solution in Fig. 3.11(d).

Chapter 4

Modulated Surface Impedance Realization

How to physically realize a given surface impedance modulation is of paramount importance for leaky-wave antenna design. This is because the IBC is mathematically convenient, but does not provide a way to obtain a physical guiding structure. In this chapter we consider two ways to make a physical structure that has the desired surface impedance. The first way is, using the theory of a grounded dielectric slab (see [3], Sec. 3.6.2), we realize a given surface impedance modulation via slab thickness modulation analytically. Both sinusoidal and square-wave modulations are considered to realize two leaky-wave antennas using 3D full-wave electromagnetic simulator CST [38].

The second way is, employing the theory of a grounded dielectric slab, with the surface impedance modulation realized via permittivity modulation of a grounded slab. This in turn can be achieved through perforations of the grounded dielectric slab. The two perforation parameters are: the hole radius r and the hole spacing s. A commercial full-wave solver (CST [38]) can be used to numerically calculate the dispersion curve β of the surface wave mode for r and s variations. Knowing β for a given r and s allows one to extract the permittivity as $\epsilon_r(r, s)$.

In any practical leaky-wave antenna design excitation of the radiating aperture is important to consider. The spurious radiation from the feed might contaminate the leaky-wave radiation pattern, which is not desired. Two different ways of exciting the leaky-wave antennas are tested using full-wave analysis (CST). These feeds are not idealized 2D models but are actual 3D structures that can be built.

4.1 Dielectric Grounded Slab and Feed

An ideal feed should only excite the guided mode and should have minimum contribution to the far field otherwise. In an effort to minimize the direct radiation from the excitation feed, Sharkawy *et al.* [39] presented a ridge-gap waveguide horn and Foroozesh *et al.* [40] used a rectangular waveguide to excite a metal strip grating leaky-wave antenna. Many other researchers e.g. Poldilchak *et al.* [26] have considered the design of high efficiency surface-wave launchers. We do not attempt to advance the state of the art in this regard. Rather, we prefer to use a simple launcher with adequate return loss and low radiation. Our focus is on the radiation pattern. To this end, we investigated two ways of exciting the antenna, which are as follows.

A modulated reactance can be physically realized by using a grounded dielectric slab in Fig. 4.1(a) with a feed that excites a TM_0 surface wave (it is H_z polarized). The feed is based on a substrate integrated waveguide (SIW). The dimensions of the SIW are chosen such that the mode inside the SIW is the fundamental TE_{10} mode (with respect to x), which is to say that it has an H_z component. The SIW is excited by a microstrip line as shown in Fig. 4.1(a). This kind of excitation is easy to fabricate. As shown in Fig. 4.1(a), there is a discontinuity at the open-circuit end of the SIW. In spite of this, the reflection coefficient $|S_{11}|$ remains below -10 dB, as shown in Fig. 4.1(b). The weak reflection also implies that this lossless structure is radiating; we note in passing that it is an end-fire antenna. This work in reported in [35].

The grounded slab dielectric thickness is d and the permittivity is $\epsilon_d = \epsilon_0\epsilon_r$. For $y \geq 0$ and looking down in the $-y$ direction, the tangential field components of the surface wave provide the impedance (see [37], p. 170)

$$Z = \frac{E_x}{H_z} = \frac{j\alpha}{\omega\epsilon_0}. \tag{4.1}$$

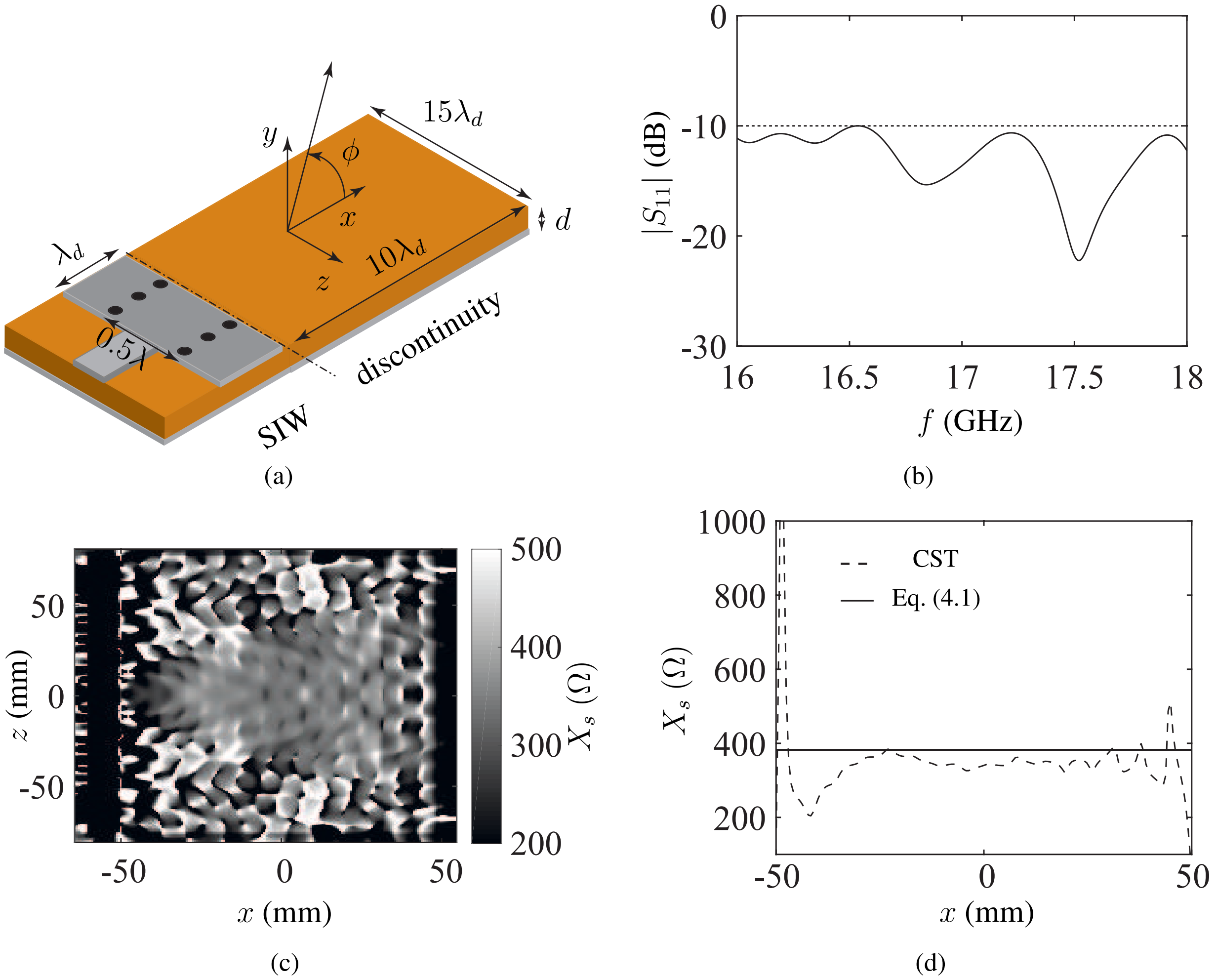

(a) (b)

(c) (d)

Figure 4.1: a) Illustration of the grounded dielectric slab, SIW exciting a TM_0 surface wave. b) Reflection coefficient $|S_{11}|$. c) Impedance in the x-z plane at $y = 0$ (CST). d) Cut of impedance profile in the x-z plane at $z = 0$. Taken from [35].

α is found from the pair of equations (see [3], p. 86), which stems from enforcing the tangential field continuity along the air-dielectric interface,

$$(k_y d)\tan(k_y d) = \epsilon_r(\alpha d) \tag{4.2}$$

$$(k_y d)^2 + (\alpha d)^2 = (kd)^2(\epsilon_r - 1) \tag{4.3}$$

by eliminating k_y and solving the resulting transcendental equation for α with the secant method or other numerical techniques. Here, k_y and α are the y-direction wavenumber and attenuation

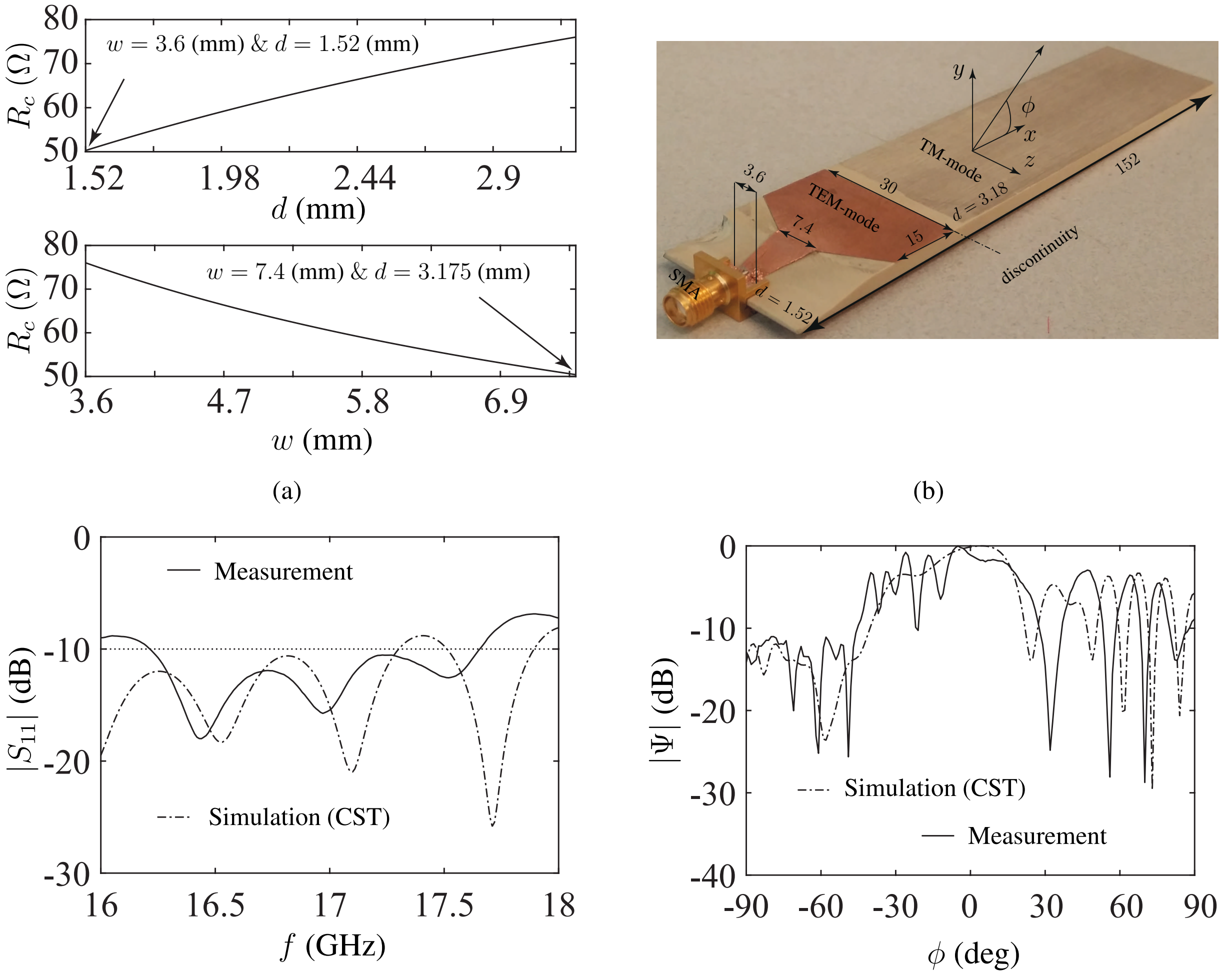

(a) (b)

(c) (d)

Figure 4.2: a) Microstrip line impedance variation as function of dielectric thickness d and line width w variation (see [3], p. 53). b) Fabricated prototype (all dimensions are in mm). c) Reflection coefficient $|S_{11}|$. d) Normalized far field radiation pattern at 17 GHz.

constant; ω is the angular frequency. With a thickness of $d = 3.175$ mm, a relative permittivity $\epsilon_r = 3.27$, and a frequency of 17 GHz, we obtain $\alpha = 364$ np/m from which (4.1) gives $Z = j385\,\Omega$. The impedance boundary and grounded slab should have the same fields, so $Z_s = j385\,\Omega$ as well. In Fig. 4.1(d) this Z_s is compared with Z_s obtained from the tangential fields in a CST simulation. Away from the edges the agreement on the average is close, which validates the concept. This work is reported in [35].

Alternatively, one can use a parallel plate waveguide to excite the surface wave on the grounded slab. The parallel plate waveguide can be excited with a microstrip transmission line. As the thickness of the slab is $d = 3.175$ mm, which leads to a wider $50\ \Omega$ microstrip line of width $w = 7.4$ mm (using $Z_0 \cong \eta d/w$; see [3], p. 53). In order to excite the microstrip line with an SMA connector a thinner dielectric substrate and a narrower line width is required. To that end, let us consider a dielectric thickness $d = 1.52$ mm and $\epsilon_r = 3.27$ for which the $50\ \Omega$ line width is $w = 3.6$ mm. If the d is increased, it results in an increase of the line impedance as shown in Fig.4.2(a). This increase in the line impedance can be compensated by increasing the line width w, which is shown in Fig.4.2(a). Hence, the line width w tapering is used in conjunction with the slab thickness d tapering to keep the impedance $50\ \Omega$.

The fabricated prototype and $|S_{11}|$ is shown in Fig. 4.2(b) and (c), respectively. The mode inside the parallel plate waveguide is TEM and mode on the grounded slab is TM_0 (H_z). In spite of the discontinuity, $|S_{11}|$ remains below -10 dB. Furthermore, the surface wave does radiate in the expected end fire direction ($\phi = 0°$), which can be seen from the far field radiation pattern in Fig. 4.2(d). This design was not optimized and it is also speculated that the discontinuity might be contributing to the radiation. This prototype served as a proof of concept, and better results might be obtained with a more efficient launcher.

4.2 Thickness Modulated Grounded Slab

A given surface impedance modulation $X_s(x)$ can be realized by modulating the thickness of a grounded dielectric slab $d(x)$. In the subsequent sections, the theory of a grounded dielectric slab is used to map a given impedance modulation onto the thickness of a slab. This work is reported in [41].

4.2.1 Sinusoidal Thickness Modulation

Consider a sinusoidally modulated impedance of the form

$$Z_s(x) = jX_{av}\left[1 + M\cos\left(\frac{2\pi}{p}x\right)\right] \tag{4.4}$$

where X_{av} is the average reactance, M is the modulation index and p is the period. Generally $M \leq 1$, and $M = 0.2$ is typical. From Oliner and Hessel [8], one can find the propagation constant k_x, which is based on the transverse resonance method and Floquet's theorem for periodic structures (see Chapter 2). A sinusoidally modulated impedance surface allows for a complex wavenumber k_x:

$$k_x = \beta_n - j\alpha$$

where $\beta_n = \beta_0 + \dfrac{2n\pi}{p}$ and $n = \pm 1, \pm 2, \cdots$ (spatial harmonics). The relationship between the beam angle ϕ_0 and β_{-1} is

$$\phi_0 = \cos^{-1}\left(\frac{\beta_{-1}}{k}\right). \tag{4.5}$$

For a desired beam angle of ϕ_0 and a chosen period p, we can calculate the required average reactance X_{av} via the approximate equation (2.5) or vice versa. As an example, we have chosen $p = 14.7$ mm, $\phi_0 = 82.4°$. With these parameters and a frequency of 17 GHz, (4.5) allows one to calculate $\beta_{-1} = 47.0753$ radians/m. Substituting this β into (2.5) provides $X_{av} = 335\ \Omega$.

Eq. (2.5) cannot provide α and to this degree of approximation, $\alpha = 0$. However the expressions (2.6) (2.7) with terms of $O(M^2)$ can be used to obtain α and also improve the accuracy of β. Assuming a modulation depth of $M = 0.2$ leads to $\alpha = 1.6604$ np/m and $\Delta\beta = -1.1192$ radians/m. The corrected phase constant is $\beta_{-1} + \Delta\beta = 45.9561$ radians/m which, via (4.5), implies that $\phi_0 = 82.6°$; a negligible change in the beam angle. More importantly, we now have the very significant parameter α which is related to the beamwidth. Using the aforementioned parameters

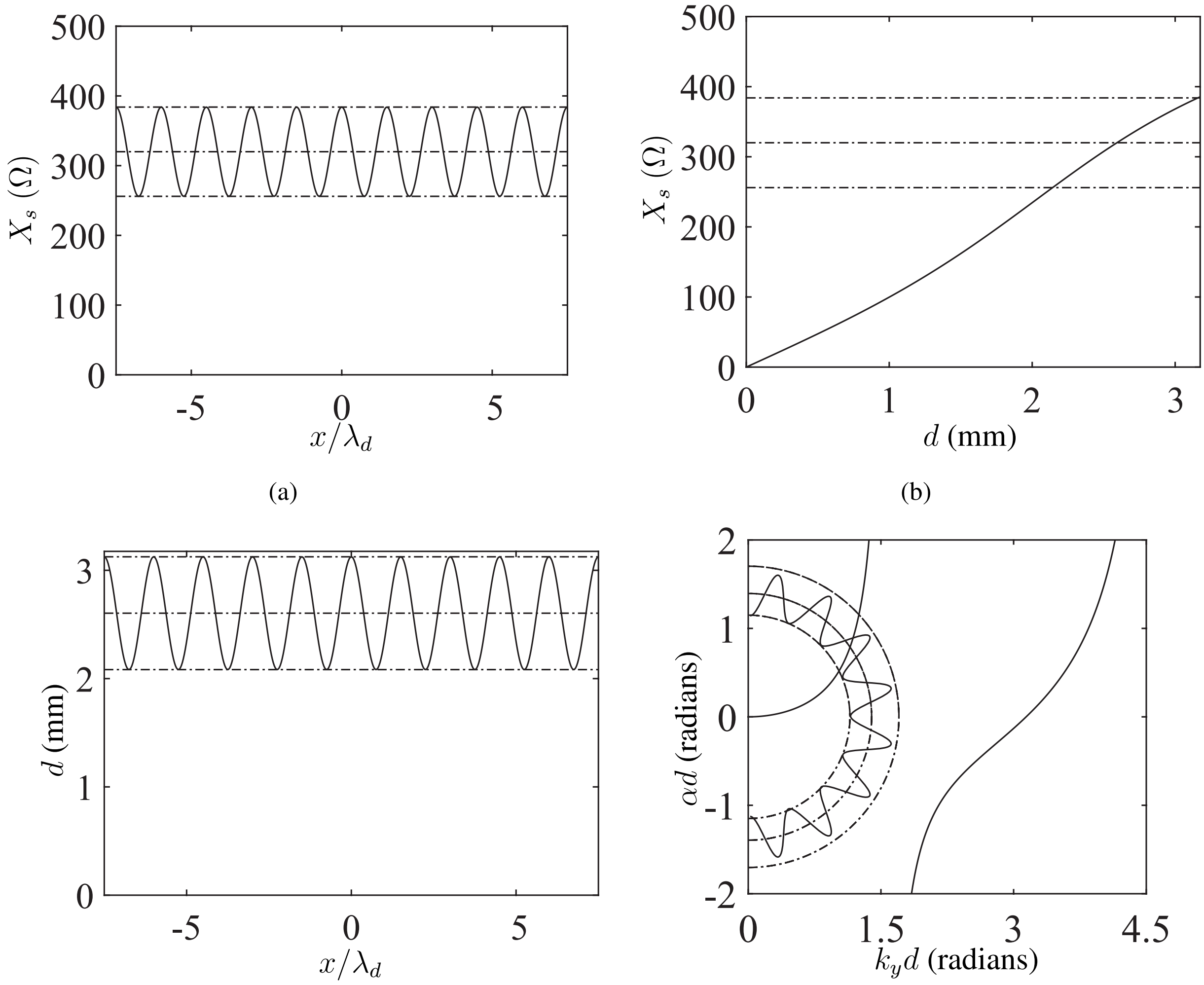

(a)

(b)

(c)

(d)

Figure 4.3: a) Sinusoidally modulated impedance profile. b) Surface impedance variation vs dielectric thickness d. c) Desired spatial variation of dielectric thickness d. d) Modal analysis of the desired variation of d (plot of (4.2) and (4.3)). Taken from [35].

we can plot the impedance in (4.4), which is shown in Fig. 4.3(a).

The IBC-MoM model (see Chapter 3) should use the same surface reactance as the physical structure shown in Fig. 4.4(a). Therefore, the surface impedance $Z_s(x) = jX_s(x)$ shown in Fig. 4.3(a) is used in (3.28) and (3.29) and then solved to obtain the induced currents, which are then substituted in (3.34) and (3.35) to compute the far field radiation pattern.

To obtain a physically realizable antenna, the sinusoidal impedance can be mapped to a dielectric thickness variation by using (4.1). The variation of the surface impedance as a function

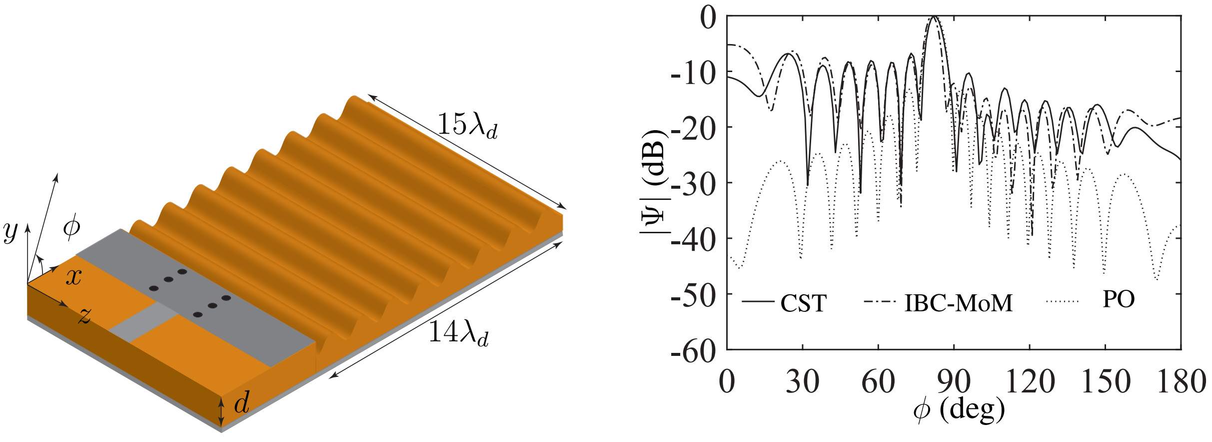

(a) (b)

Figure 4.4: a) Illustration of the physical structure. b) Normalized far field radiation pattern at 17 GHz. Taken from [35].

of dielectric thickness d is shown in Fig. 4.3(b). The relation between X_s and d is approximately linear, which makes $d(x)$ in Fig. 4.3(c) sinusoidal. This linearity is not a requirement, but might make the design more straightforward.

Fig. 4.3(d) is a graph of (4.2) and (4.3) in which $d = d(x)$ has a varying range and it shows there is only one surface wave mode solution and no higher modes. An illustration of the physical structure is shown in Fig. 4.4(a). The length of the antenna is 136.62 mm (or $14\lambda_d$, where $\lambda_d = \lambda/\sqrt{\epsilon_r} = 9.75$ mm).

It is noted that the surface impedance is obtained from the total tangential fields at $y = 0$, looking into the surface. At near-grazing incidence the field is dominated by a surface wave, whose impedance (4.1) does not depend on height y. Therefore, the air gaps between the $y = 0$ plane and the troughs of the modulated slab do not alter the impedance. Strictly speaking, there is also a space wave (the continuous spectrum), but it is negligible for the modulation depths considered here, as shown by Khan and Paknys [42] and is discussed in Sec. 4.3.

The radiation patterns obtained from the PO/Oliner-Hessel theory, IBC-MoM, and CST are shown in Fig. 4.4(b). The physical optics (PO) solution is computed by using k_x from the method provided by Oliner and Hessel and a radiation integral using an aperture field distribution of the form $e^{-jk_x x}$. PO provides an approximate radiation pattern of the leaky mode on a finite-length

Table 4.1: Frequency Scanning and 3-dB Beamwidth [35]

f (GHz)	beam angle CST	beam angle IBC-MoM	beamwidth CST	beamwidth IBC-MoM
16	$87.40°$	$87.05°$	$12.25°$	$12.46°$
16.5	$84.94°$	$84.15°$	$10.19°$	$10.61°$
17	$82.61°$	$81.62°$	$8.43°$	$8.79°$
17.5	$78.19°$	$78.01°$	$7.73°$	$7.92°$
18	$75.85°$	$75.11°$	$6.55°$	$6.91°$

antenna. The scan angle and beamwidth are accurately predicted by the Oliner-Hessel theory, and PO provides the side lobes. Also in the PO solution there is no feed.

A 2D Huygens source which comprised of a J_{0z} line source and a M_{0x} dipole source is used to excite an impedance strip with sinusoidal reactance modulation. On the other hand, a 3D SIW excited with a microstrip line is used to excite the actual physical antenna as shown in Fig. 4.4(a). These two feeds are quite different. In spite of this, the side lobe structure for both models are very similar. It indicates that for both cases if there is any direct radiation from the source it must be small, so that the radiation pattern characteristics are mainly due to the leaky mode in the radiating aperture. More importantly, it shows that the fine details of the feed do not matter when the feed is well designed and has minimal radiation.

All three results predict the scan angle and beamwidth quite well. The IBC-MoM shows a scan angle and beamwidth that is close to the PO and CST predictions. The scan angle differs by about 1 degree and the 3 dB beamwidth is smaller by about 1.2%. PO is the most approximate of all three methods, as it does not include more subtle effects such as a negative-x travelling reflected wave in the aperture field.

The surface reactance mapping onto the dielectric thickness, as shown in Fig. 4.3(b), is frequency dependent. In the IBC-MoM an appropriate surface reactance at a given frequency must be used. Care must be taken while changing the frequency, so that higher order modes do not appear on the grounded slab, which is to say, the circle in Fig. 4.3(d) should intercept only once with the $\tan$ function for a given frequency. Other frequencies in the range of 16-18 GHz were tested and the resulting scan angles and beamwidths for the sinusoidally-modulated antenna are shown in Table 4.1. It was found that the beam scanning behavior predicted by IBC-MoM and CST were the same, scanning forward with increasing frequency, which is expected for this type of antenna.

4.2.2 Square-Wave Thickness Modulation

A square wave impedance is attractive due to the relative ease of fabrication compared to the sinusoidal case. This profile can be expressed as follows:

$$Z_s(x) = jX_{av}[1 + Mf(x)] \tag{4.6}$$

where X_{av} is the average reactance, M is the modulation index and $f(x)$ is a unit-amplitude square wave with a period p and average value of zero. The impedance is shown in Fig. 4.5(a) for the case $p = 9.8$ mm, $X_{av} = 320\ \Omega$ and $M = 0.2$. The mapping of the reactance X_s onto the dielectric thickness d leads to the spatial variation of d, which is shown in Fig. 4.5(b). The variation only allows the TM$_0$ mode on the structure. An illustration of the physical structure is shown in Fig. 4.5(c). The length of the antenna is 136.62 mm (or $14\lambda_d$, where $\lambda_d = \lambda/\sqrt{\epsilon_r} = 9.75$ mm). The same kind of SIW feed is used as for the sinusoidal case.

The radiation patterns obtained from IBC-MoM and CST models are shown in Fig. 4.5(d). The scan angle can be approximately predicted by (2.5). Considering the $n = -1$ spatial harmonic, $X_{av} = 320\ \Omega$ and $p = 9.8$ mm, we can use (4.5) and (2.5) to find $\beta_{-1} = -176.8295$ radians/m and $\phi_0 = 119.77°$. For the IBC-MoM, $Z_s(x) = jX_s(x)$ from Fig. 4.5(a) is used in (3.28) and (3.29) and then solved to obtain the induced currents, which are then substituted in (3.34) and (3.35) to compute the far field radiation pattern.

The same scan angle is obtained from both IBC-MoM and CST, as seen in Fig. 4.5(d). The 3 dB beamwidths differ by about 0.4%. The side lobe features are not as well predicted as in the sinusoidal case. It is speculated that with a backward beam in the $\phi_0 \approx 120°$ direction there are more subtle diffraction effects from the feed that are not accounted for in the IBC-MoM model.

Eq. (2.5) is approximate, as β for an unmodulated slab is not the same thing as β_0, associated

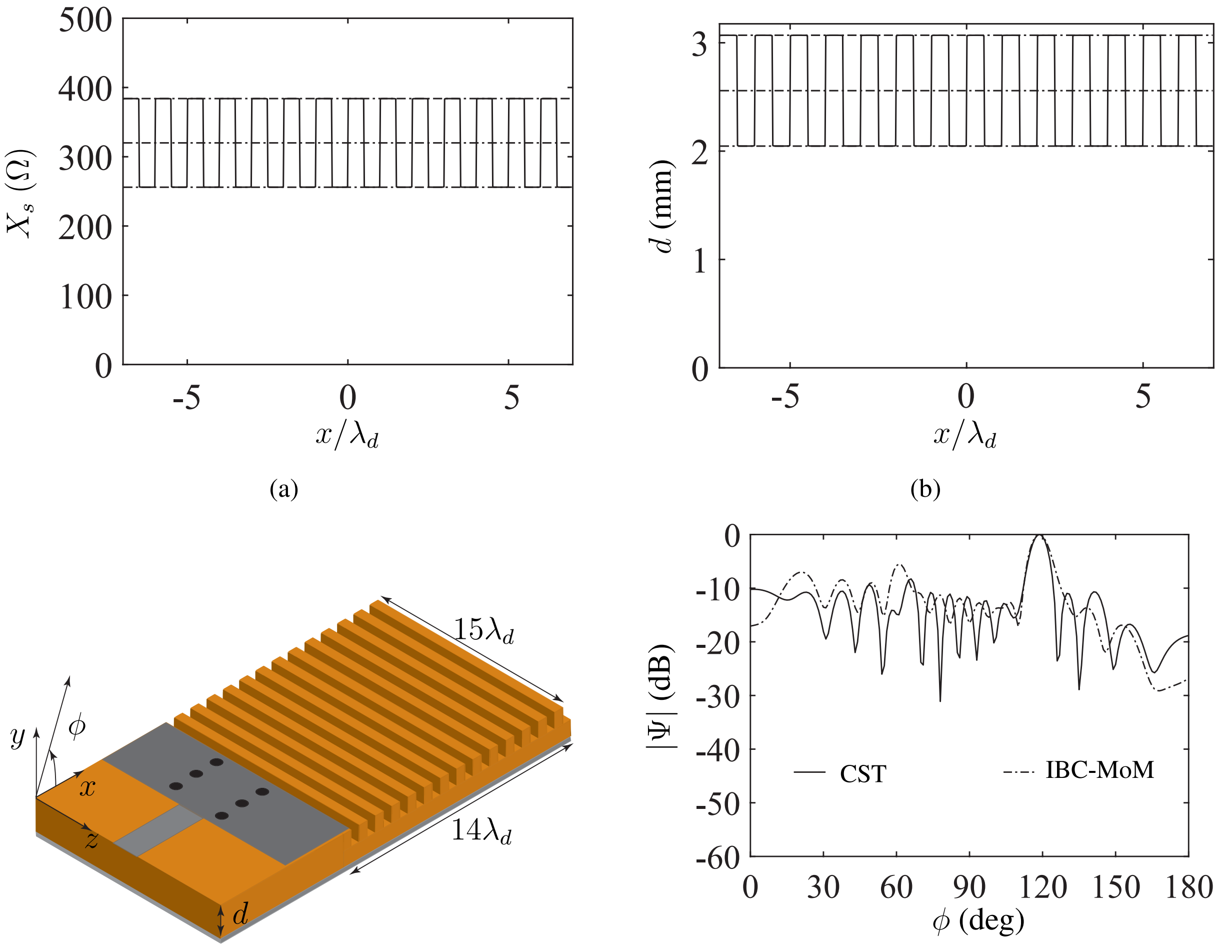

(a) (b)

(c) (d)

Figure 4.5: a) Square wave impedance profile. b) Desired spatial variation of dielectric thickness d. c) Illustration of the physical structure. d) Normalized far field radiation pattern at 17 GHz. Taken from [35].

with the $n = 0$ harmonic of the modulated slab. In spite of this, it provides a satisfactory result for the specific case considered here. Due to the finite length of the antenna, there is a reflected wave which radiates at about $\phi \approx 60°$. This work is reported in [35].

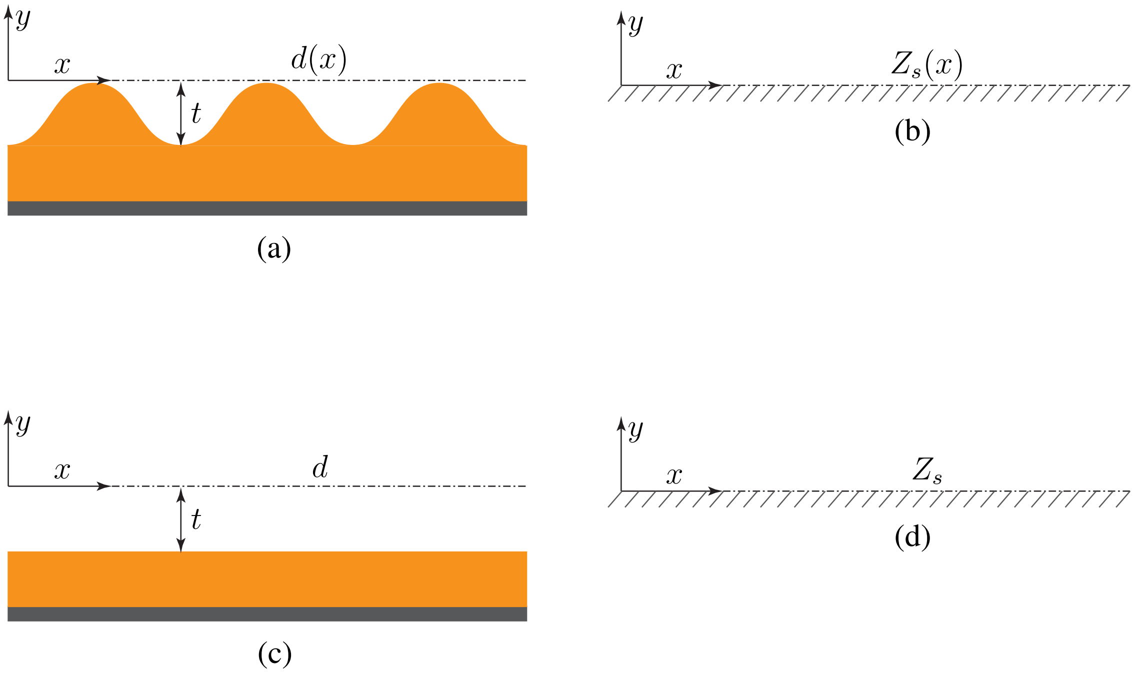

(a) (b) (c) (d)

Figure 4.6: a) Thickness modulated grounded slab $d(x)$. b) Equivalent surface impedance $Z_s(x)$. c) Grounded slab with a constant thickness d and gap t. d) Equivalent surface impedance Z_s. Taken from [42].

4.3 Air Gap Between the Impedance Boundary and the Physical Boundary

In this section some results are obtained that show it is not necessary to have an impedance boundary conform to a physical surface. This is important because it is very convenient to specify an IBC on a flat plane, whether or not the actual structure is flat. This happens, for instance, on a corrugated surface.

A grounded slab with modulated thickness $d(x)$ is shown in Fig. 4.6(a). Consider the surface impedance being evaluated at $y = 0$. We can replace the real structure with an equivalent surface impedance $Z_s(x)$ as shown in Fig. 4.6(b). As shown in Fig. 4.6(a) there is a gap t between the $y = 0$ plane and the physical structure. In order to evaluate the effects of this gap t, we can simplify the problem by studying a constant thickness slab with the same gap t between the field point plane (where the impedance is evaluated) and the physical structure shown in Fig. 4.6(c). The impedance equivalent for this case is shown in Fig. 4.6(d). This simplified problem of a constant thickness slab d with the gap t is studied in following discussion, which will allow us to understand the effect of the gap t on the surface impedance, and is discussed subsequently.

Consider a grounded slab excited by a magnetic line source M_{0z} as shown in Fig. 4.7(a). The complete rigorous field solution for this problem is provided in Appendix B. Also, it is shown in [42] that close to the source M_{0z} the reactance of the slab is not constant. However, when the field point is approximately 2λ away from M_{0z} the exact reactance becomes the surface wave reactance (see Chapter 3).

Considering $x \geq 2\lambda$, we can change the height t of the field points, as shown in Fig. 4.7(a). When $t = 0$ this leads to $\alpha = 90°$ which results in $\angle\Gamma = -180°$ which is shown in Fig. 4.7(b). This leads to a cancellation of free space field contribution G_f with the reflected field contribution G_s. The only contribution in this case comes from surface wave G_p (see Appendix B and Chapter 3). From Fig. 4.7(b) we can see that as long as $t < 0.1\lambda$, G_f and G_s still effectively cancel, leaving a field that is predominantly a surface wave. It is also noted that when G_f and G_s cancel, the surface-wave impedance (4.1) becomes the total impedance and this is independent of t. This consequently allows us to ignore the gap t; this is used in the following discussion to evaluate the reactance of a thickness modulated grounded slab.

Using (4.1) in conjunction with (4.2) and (4.3) allows us to calculate the surface reactance $X_s(d)$ for a given slab thickness d with $\epsilon_r = 4$ as shown in Fig. 4.8(a). Care must be taken while changing d, such that the higher order modes do not appear, which is to say the circle (4.3) should intercept only once with the $\tan$ function in (4.2) for a given d. The X_s and d do not have a linear relation. However, for design convenience it has been chosen to be in the linear region, as shown in Fig. 4.8(a). This allows us to map a given $X_s(x)$ linearly onto $d(x)$.

Consider a grounded slab with a periodic thickness modulation as shown in Fig. 4.8(b) and (d), sinusoidal and square-wave thickness modulation respectively. The excitation M_{0z} is at $(x_0, y_0) =$

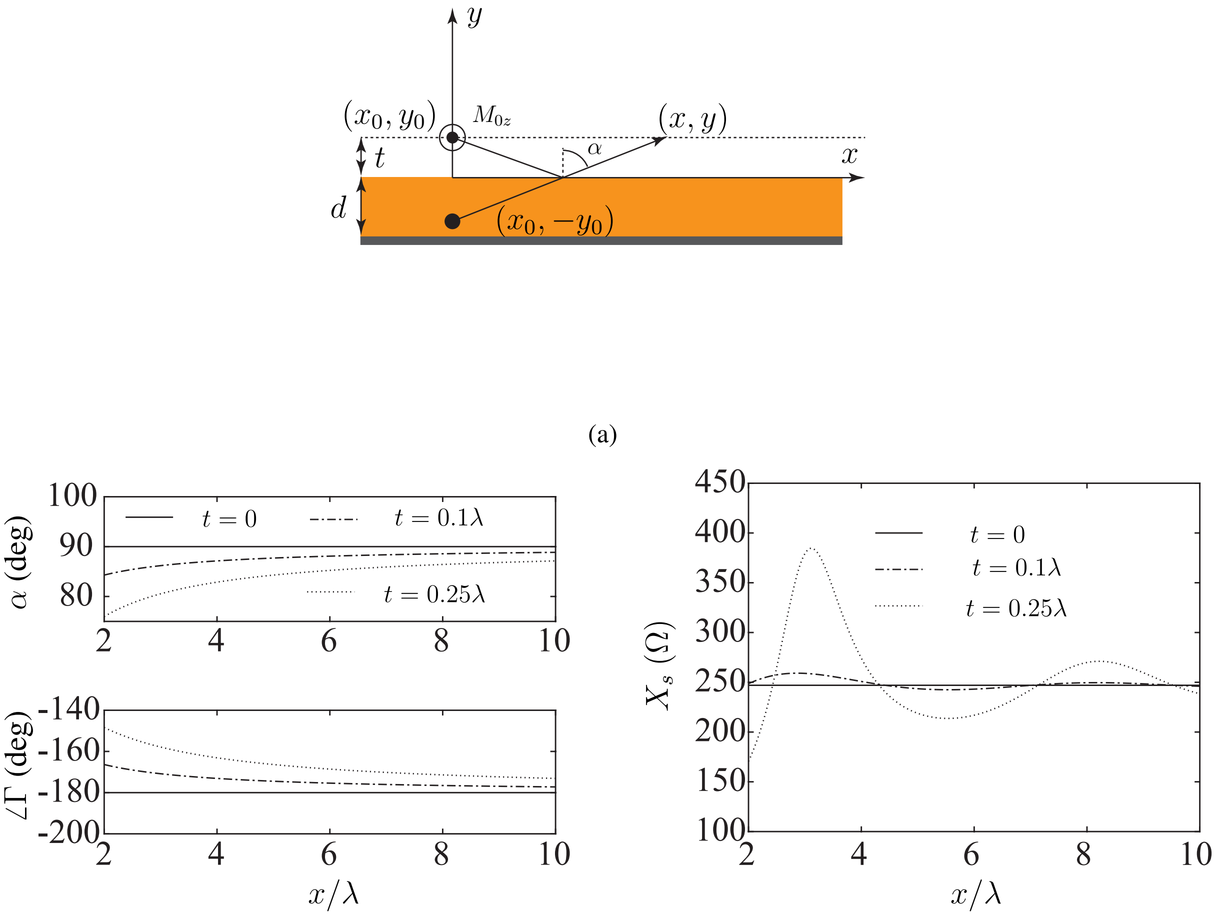

(a)

(b)

(c)

Figure 4.7: a) Grounded dielectric slab excited by a magnetic line source M_{0z}. b) α and phase of Γ variation as a function of x and impedance plane height t. c) X_s for different impedance plane heights t. Taken from [42].

$(0, 0)$ as shown. A reference plane is at $y = 0$. The thickness modulation of the slab leads to some gaps of depth t between the reference plane and the physical structure. If $t < 0.1\lambda$ the impedance $Z_s(x, y)$ at $y = 0$ and $y = -t$ between the teeth will be about the same. This allows one to ignore the gaps between the physical structure and the reference plane. The surface wave impedance as a function of slab thickness can be calculated by (4.1) and compared with the impedance from the tangential fields above the actual structure, computed with a full-wave solver (CST) at $y = 0$ as shown in Fig. 4.8(c) and (e), sinusoidal and square-wave thickness modulation respectively. For $t = 0.05\lambda$ the surface-wave impedance via (4.1) is in agreement with the impedance from the

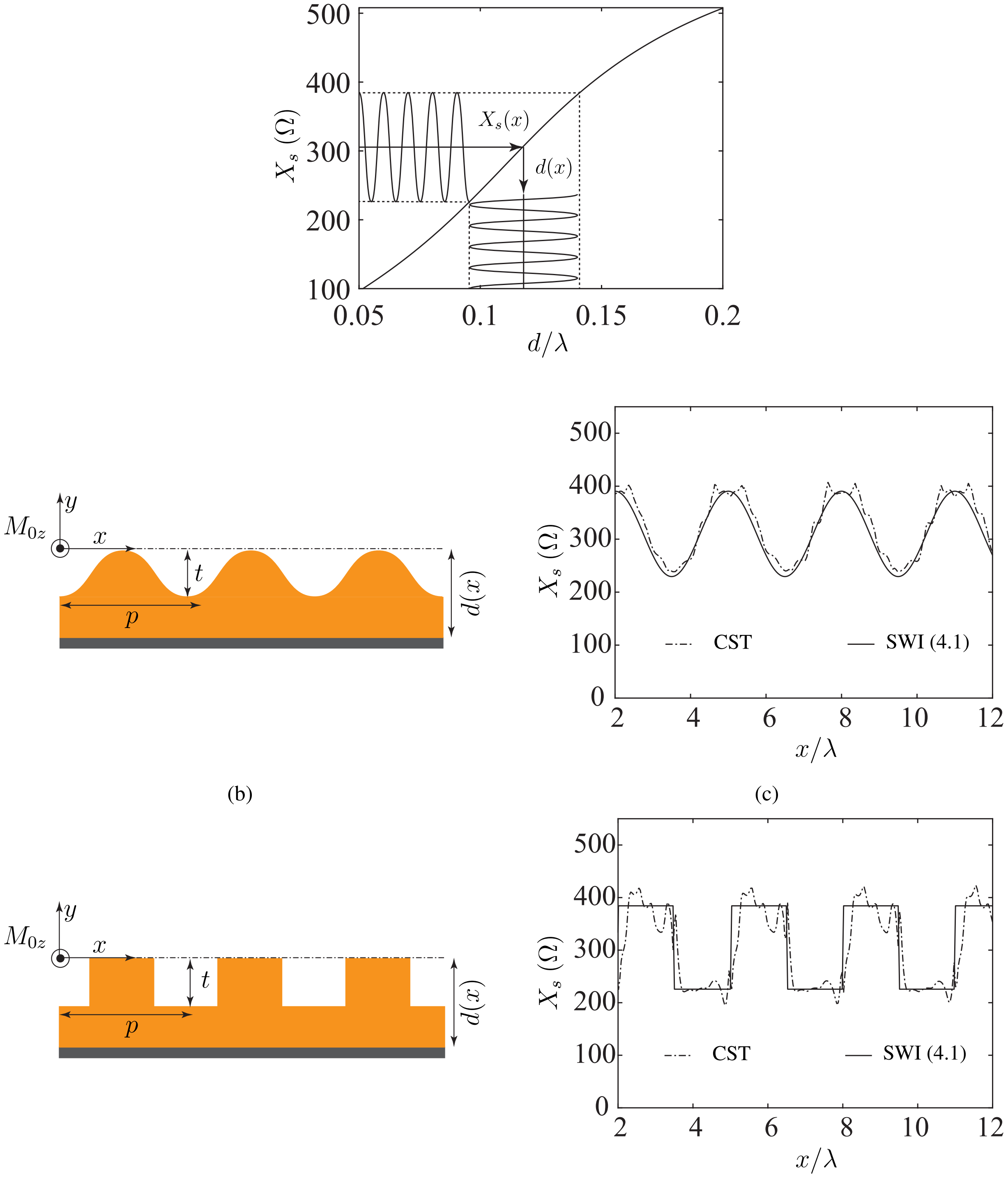

(b)

(c)

(d)

(e)

Figure 4.8: a) Surface reactance as a function of slab thickness $X_s(d)$. b) Sinusoidally thickness modulated grounded dielectric slab. c) Surface reactance computed with CST and compared with surface-wave impedance (4.1) for the structure in Fig. 4.8(b) with $t = 0.05\lambda$ at $y = 0$. d) Square-wave thickness modulated grounded dielectric slab. e) Surface reactance computed with CST and compared with surface-wave impedance (4.1) for the structure in Fig. 4.8(d) with $t = 0.05\lambda$ at $y = 0$. Taken from [42].

full-wave solver. This work is reported in [42].

4.4 Permittivity Modulated Grounded Slab

As an alternative to varying the thickness, surface impedance modulation $Z_s(x)$ can be realized via permittivity modulation $\epsilon_r(x)$ of a grounded dielectric slab. To illustrate this idea, let us consider the square-wave impedance modulation expressed by (4.6). As an example, assume the average reactance $X_{av} = 335\ \Omega$, the modulation index $M = 0.2$ and period $p = 1\lambda$. With these parameters one can plot (4.6) which is shown in Fig. 4.9(a). Considering $f = 5$ GHz, one can use (4.5) and (2.5) to find $\beta_{-1} = 35.37$ radians/m and approximately compute the beam angle $\phi_0 \approx 70.2°$.

Assuming the grounded slab thickness $d = 10$ mm, (4.2) and (4.3) can be solved numerically (secant method) and used in conjunction with (4.1) in order to map the X_s variation onto the ϵ_r variation, which is shown in Fig. 4.9(b). The X_s does not vary linearly with ϵ_r. But, for design convenience the reactance modulation parameters (M, p, X_{av}) are chosen such that it remains in the linear region, however, this is not a requirement.

The required spatial variation of $\epsilon_r(x)$ is shown in Fig. 4.9(c). For this $\epsilon_r(x)$ modulation only the TM$_0$ mode exists on the slab, which can be seen in Fig. 4.9(d). An illustration of the structure realized in CST is shown in Fig. 4.9(e). The IBC-MoM model (see Chapter 3) should use the same surface reactance as that of the physical structure, which is shown in Fig. 4.9(e). Therefore, the surface impedance $Z_s(x) = jX_s(x)$ shown in Fig. 4.9(a) is used in (3.28) and (3.29) and then solved to obtain the induced currents, which are then substituted in (3.34) and (3.35) to compute the far field radiation pattern.

The radiation patterns obtained from the IBC-MoM and CST are shown in Fig. 4.9(f). The main beam was expected to be at $\phi_0 \approx 70°$ which is obtained from both solutions. The IBC-MoM 3 dB beamwidth is larger by 2° than CST. Also, due to finite extent of the structure in the x direction it has a reflected negative-x travelling wave which radiates at $\phi \approx 110°$. This work in reported in [43].

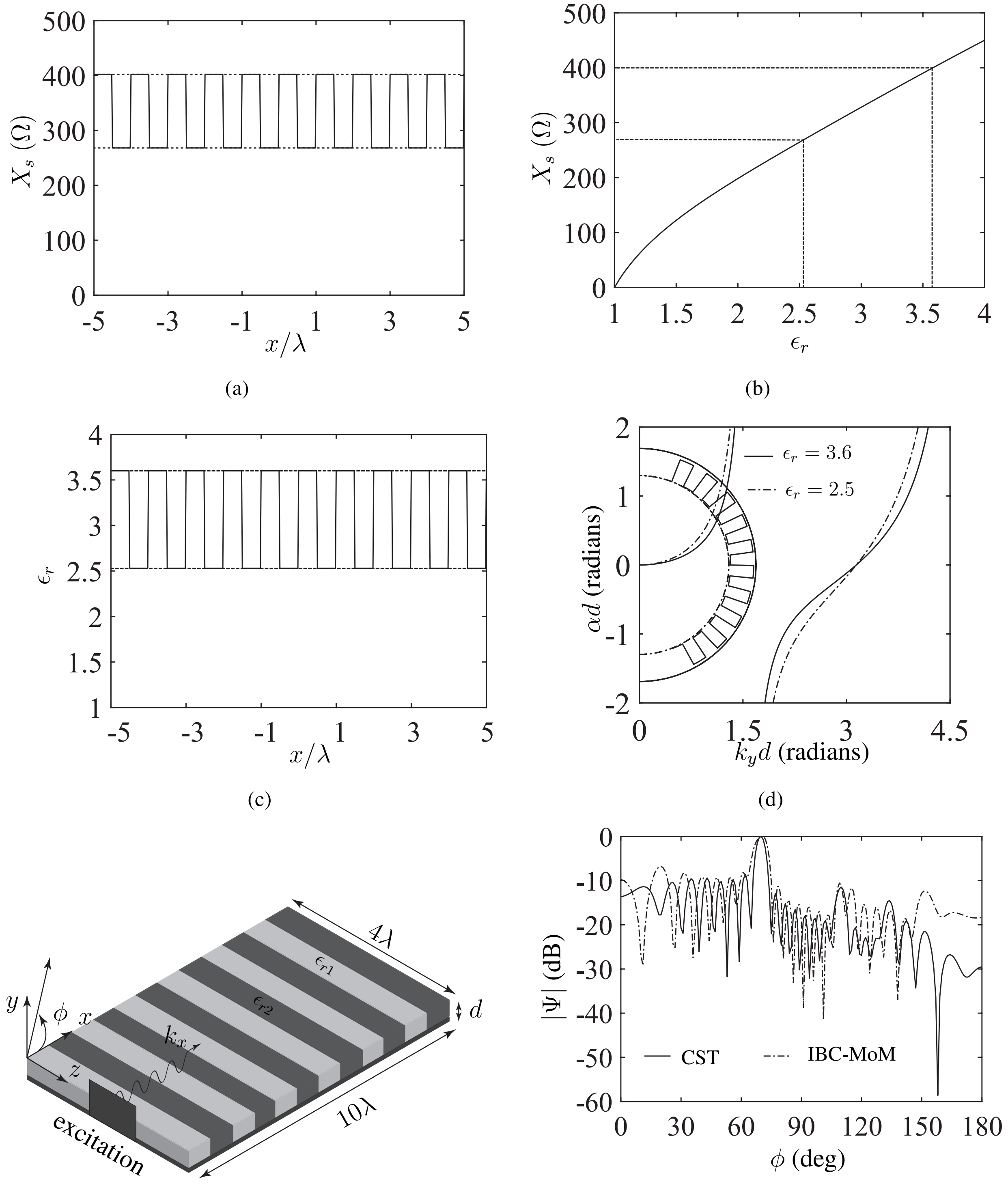
(a) (b) (c) (d) (e) (f)

Figure 4.9: a) Square wave impedance profile. b) Surface impedance variation vs dielectric permittivity ϵ_r. c) Desired spatial variation of permittivity ϵ_r. d) Modal analysis of the desired variation of ϵ_r (plot of (4.2) and (4.3)). e) Illustration of a grounded dielectric slab with periodically varying ϵ_r in x direction. f) Normalized far field pattern computed at 5 GHz [43].

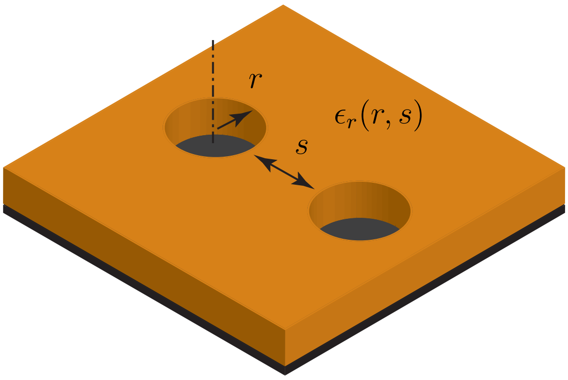

Figure 4.10: Perforated grounded dielectric slab.

4.4.1 Perforated Dielectric

In order to realize the spatial permittivity variation $\epsilon_r(x)$ we can use perforations. The two perforation parameters are: the hole radius r and the hole spacing s as shown in Fig. 4.10. It is imperative for the design to map out the permittivity variation as the function of r and s, which is to say $\epsilon_r(r, s)$, which is discussed in the following sections.

Perforations allow a lot of control over the value of the effective ϵ_r. First, a procedure is desired, using a full-wave simulator to determine β, and in turn ϵ_r. This is first tested on a unit cell where ϵ_r is already known. Once the procedure has been validated it is then applied to the perforated case.

Let us consider a unit cell of a grounded slab, which is periodic in the x direction, as shown in Fig. 4.11(a). The ϵ_r is arbitrarily chosen to be 3.6. The goal of this test case is to be able to retrieve the same value of ϵ_r.

Let us assume the phase variation in the z direction to be 0; this simplifies the problem. We can use a numerical full-wave eigenmode solver (CST) to calculate the field distribution for all the modes of the unit cell shown in Fig. 4.11(a). However, only the TM$_0$ mode (surface wave) is of interest. The full-wave E_x field distribution in the x-y plane at $z = 0$ is shown in Fig. 4.11(b). It is evident from the field decay in the $+y$ direction (away from the air-dielectric interface) that this is TM$_0$ surface wave mode. Furthermore, we can sweep the phase Φ_x from $0°$ to $180°$ in the x direction, while keeping the physical length constant at $\ell = 20$ mm in the x direction. This allows

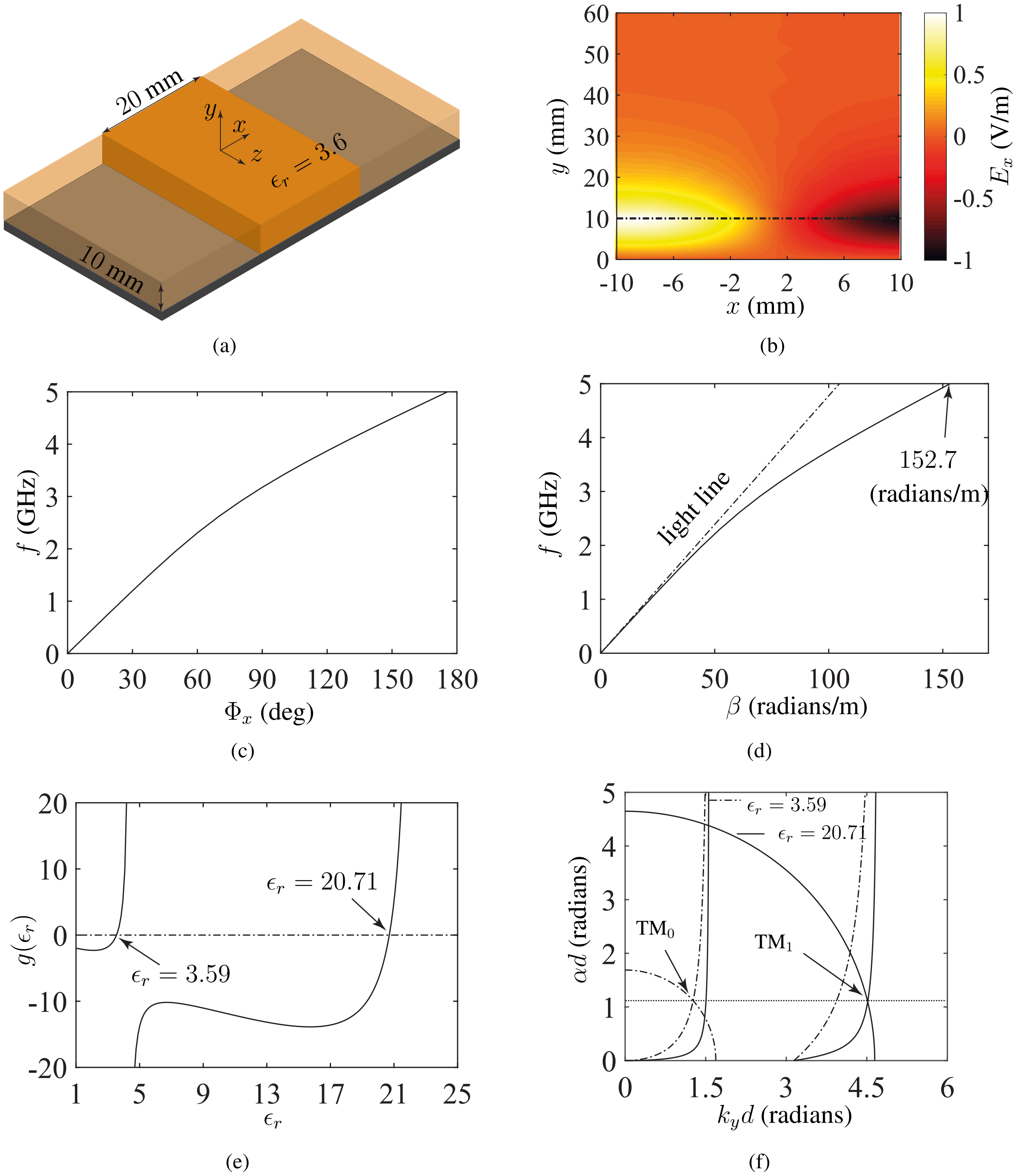

(a) (b) (c) (d) (e) (f)

Figure 4.11: a) Unit cell of a grounded slab with $\epsilon_r = 3.6$. b) TM$_0$ mode E_x field distribution in x-y plane at $z = 0$. c) Frequency variation vs phase Φ_x variation in x direction. d) Dispersion curve. e) Equation (4.12) as the permittivity ϵ_r is varied. f) Plot of (4.2) and (4.3) with $d = 10$ mm and $f = 5$ GHz.

one to compute the eigenfrequencies numerically for this mode as shown in Fig. 4.11(c). We use

$$\beta = \frac{\Phi_x}{\ell} \tag{4.7}$$

where $\ell = 20$ mm in the x direction. One can than compute the dispersion curve, which is shown in Fig. 4.11(d). As the dispersion line is underneath the light line, the wave is slow. This is expected for a surface wave mode. As a check, if we solve (4.2) and (4.3) for k_y and α numerically via secant method, with $d = 10$ mm, $\epsilon_r = 3.6$ at $f = 5$ GHz and use the following expression to calculate β:

$$\beta = \sqrt{k^2 + \alpha^2} \Rightarrow 152.8 \text{ (radians/m)}. \tag{4.8}$$

This agrees very well with the dispersion line computed with CST as shown in Fig. 4.11(d) and serves as a sanity check.

As the β is computed with the numerical eigenmode simulation, one can also calculate α as (see [3], p. 86):

$$\alpha = \sqrt{\beta^2 - k^2} \tag{4.9}$$

Our goal is to retrieve the value of ϵ_r. One can write k_y in the following form:

$$k_y(\epsilon_r) = \sqrt{k^2\epsilon_r - \beta^2} \tag{4.10}$$

For the TM mode k_y and α obey the following relation (4.2), repeated here

$$k_y d \tan(k_y d) = \epsilon_r(\alpha d). \tag{4.11}$$

A value of ϵ_r that satisfies both (4.10) and (4.11) will be a solution. We can write the following function $g(\epsilon_r)$:

$$g(\epsilon_r) = k_y(\epsilon_r)d \tan(k_y(\epsilon_r)d) - \epsilon_r(\alpha d) = 0 \tag{4.12}$$

Fig. 4.11(e) shows the variation of $g(\epsilon_r)$ as ϵ_r is swept from 1-25. As we can see in Fig. 4.11(e), the zero crossing occurs at $\epsilon_r = 3.59$, which is the expected solution; also another solution occurs at $\epsilon_r = 20.71$. The zero crossing of $g(\epsilon_r)$ repeats as ϵ_r is further increased, which leads to multiple solutions for ϵ_r.

In order to understand the other solutions we can plot (4.2) and (4.3) for the two solutions of ϵ_r, which is shown in Fig. 4.11(f). We can see that $\epsilon_r = 3.59$ corresponds to the fundamental TM_0 mode. However, $\epsilon_r = 20.71$ corresponds to the higher order TM_1 mode. This TM_1 will have the same α as TM_0 mode. By (4.8) we can see that TM_1 will also have the same β as TM_0 mode. But the propagation constant inside the dielectric in y direction k_y is different for the two modes. As in this case we are only interested in the fundamental TM_0 mode, which means that our solution is $\epsilon_r = 3.59$, which what we started with. This validates the procedure followed to extract the ϵ_r. Now we can use this procedure to extract the ϵ_r for case of a perforated grounded dielectric slab.

Consider a unit cell which is composed of perforated grounded dielectric slab. This is shown in Fig. 4.12(a). In this case we also arbitrarily chose $\epsilon_r = 3.6$. The holes drilled are deeply sub-wavelength in diameter. It is expected that the resulting ϵ_r will be less then 3.6. Assuming zero phase variation in the z direction, one can compute the eigenmode field distribution numerically from CST. The E_x field distribution is shown in Fig. 4.12(b). The decay of E_x in the $+y$ direction away from the air-dielectric interface suggests that the mode is TM_0. For this mode the phase Φ_x in the x direction can be swept from $0°$ to $180°$, while the physical length is kept constant at $\ell = 20$ mm in the x direction. The corresponding eigenfrequencies can be computed numerically from CST, and is shown in Fig. 4.12(c).

The dispersion curve is computed by using (4.7), which is shown in Fig. 4.12(d). As we can see in this case, the dispersion line lies closer to the light line as compared to the previous (non-

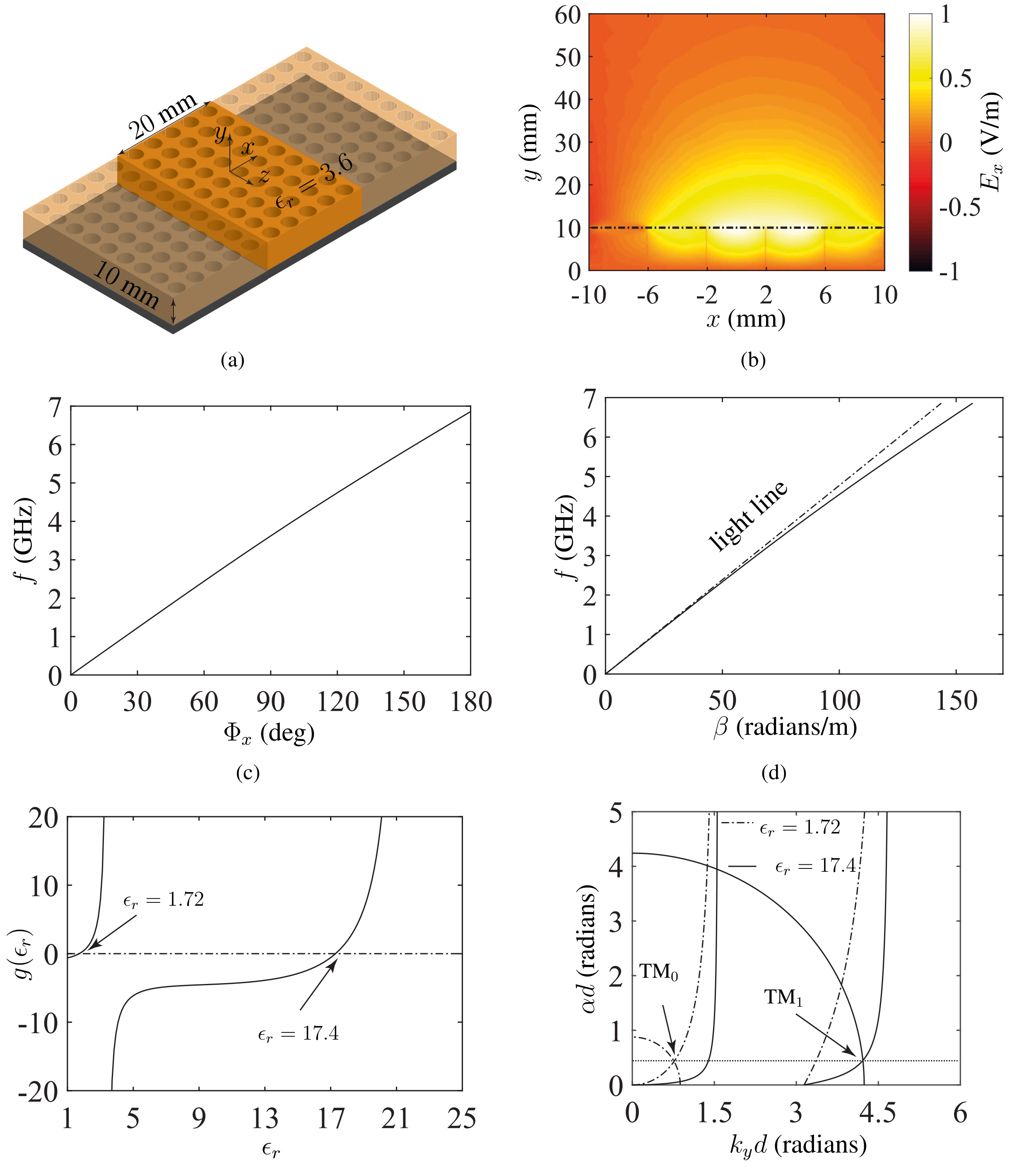

(a) (b)

(c) (d)

(e) (f)

Figure 4.12: a) Unit cell of a perforated grounded slab with $\epsilon_r = 3.6$. b) TM_0 mode E_x field distribution in x-y plane at $z = 0$. c) Frequency variation vs phase Φ_x variation in x direction. d) Dispersion curve. e) Eq. (4.12) as ϵ_r is varied. f) Plot of (4.2) and (4.3) with $d = 10$ mm and $f = 5$ GHz.

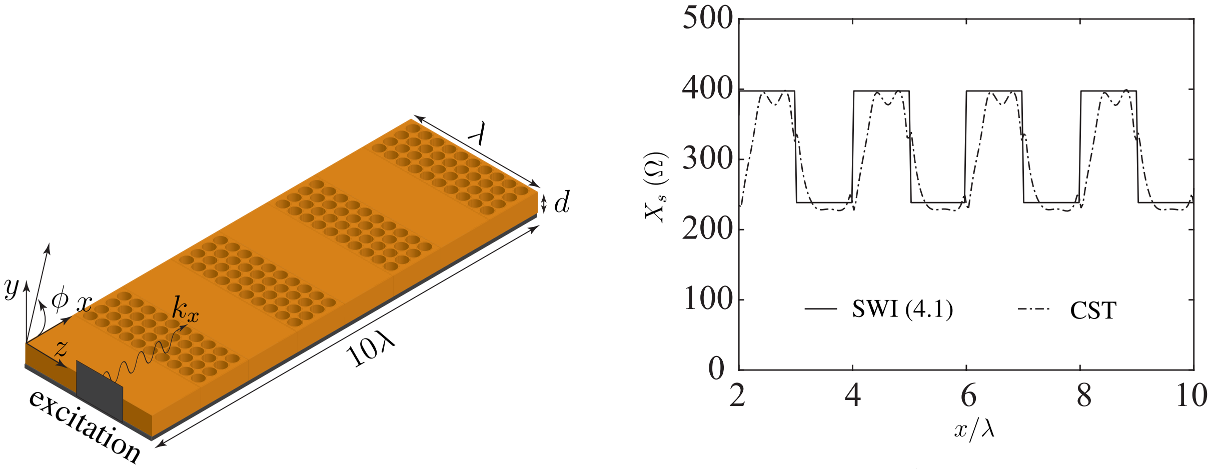

(a) (b)

Figure 4.13: a) Illustration of physical structure realized in CST [43]. b) Surface reactance comparison.

perforated) case, which means that β is closer to k (the free space propagation constant). Also, compare the E_x field distribution in Fig. 4.12(b) which is the perforated case with the E_x field distribution in Fig. 4.11(b) which is the non-perforated case. It becomes evident that the field E_x in the non-perforated case is tightly bound to the dielectric surface, which is to say it decays relatively quickly as we move away from the air-dielectric interface in the $+y$ direction, as compared to the perforated case. Both these aforementioned observations suggest a drop in the ϵ_r for the perforated case.

Using (4.12) and following the aforementioned procedure one can plot the variation of $g(\epsilon_r)$ as ϵ_r is swept from 1-25, which is shown in Fig. 4.12(e). Similar to the previous (non-perforated) case, here we also obtain multiple solutions for ϵ_r. The two solutions for this case are $\epsilon_r = 1.72$ and $\epsilon_r = 17.4$. The plot of (4.2) and (4.3) for the two solutions reveals that $\epsilon_r = 1.72$ corresponds to the TM$_0$ mode and $\epsilon_r = 17.4$ corresponds to the TM$_1$ mode as shown in Fig. 4.12(f). The procedure followed allows us to compute the permittivty as a function of hole radius and spacing $\epsilon_r(r, s)$ which is required for impedance modulation realization via perforations.

4.4.2 Impedance Modulation via $\epsilon_r(x)$

An illustration of the structure emulating reactance $X_s(x)$ variation via $\epsilon_r(r,s)$ is shown in Fig. 4.13(a). The perforated areas corresponds to a lower ϵ_r which results in lower surface reactance X_s locally. The areas with no perforations corresponds to a higher ϵ_r resulting in higher X_s, which can be seen from the X_s and ϵ_r mapping in Fig. 4.9(b).

Using a full-wave solver (CST), one can compute the fields in the x-z plane for the structure shown in Fig. 4.13(a). From these fields surface reactance can be calculated at $z = 0.5\lambda$ along x. The full-wave solution is compared with surface wave impedance (4.1) in Fig. 4.13(b). The surface wave impedance solution is for the mode on an infinite grounded slab. However, in CST a finite structure is considered. In spite of this difference the square-wave surface impedance profile can be seen in Fig. 4.13(b). The far field radiation pattern is given in Fig.4.9(f).

Chapter 5

Conclusion

Using the complete rigorous Green's function field solution for a grounded dielectric slab of infinite extent, it was shown that the surface impedance varies with the location of the excitation source. The transmit (when the source is close to the slab surface) and receive (when the source is far from the slab surface) cases are reciprocal problems but were shown to be not equivalent problems. Furthermore, by evaluating numerically a Sommerfeld integral in the complex w plane allows one to compute the exact fields in the vicinity of the excitation source. Using the exact fields, it was shown that for the transmit problem, the slab surface impedance varies spatially in the vicinity of the excitation source. The analytic surface impedance solution was validated against a numerical full-wave solution (COMSOL), both solutions show the same spatial surface impedance variation near the source region.

For the IBC to provide an accurate electromagnetic representation of the true physical slab problem, the surface impedance spatial variation has to be taken into account. However, the Green's function solution for the impedance boundary condition does not allow for the spatial surface impedance variation. One can solve this problem by evaluating the radiation integrals with true electric and magnetic fields from the true slab problem. In order to evaluate the integral over an infinite aperture, the true aperture fields were decomposed into geometrical optic (GO) and surface wave field parts. The GO field becomes zero a few wavelengths away from the source, which sets the limits for the radiation integral for the GO aperture field part. For the surface wave part, the radiated field was evaluated by taking the Fourier transform of the aperture field and solving the integral via the stationary-phase method. The field solution was validated by comparing it with the asymptotic field solution and a numerical full-wave (COMSOL) field solution for the grounded dielectric slab problem.

In order to solve an arbitrary 2D impenetrable impedance strip of finite extent, electric and magnetic coupled field integral equations were formulated. These integral equations were decoupled by employing the field symmetries and assuming Z_s is the same on both faces for the flat strip, which then allows one to solve the uncoupled integral equations for electric and magnetic equivalent currents via the method of moments (MoM). In the MoM procedure simple pulse basis functions for the unknown currents along with point matching was used. Using these electric and magnetic currents in the radiation integrals, one can compute the radiation characteristics of an arbitrary impedance strip of finite extent with arbitrary excitation. The IBC-MoM solution was validated by solving a plane wave excited impedance strip with $Z_s = 377\ \Omega$. The geometrical optic (GO) currents compared nicely with IBC-MoM currents.

In the 2D model the far field contribution from the excitation source can be minimized by using a Huygens source which radiates predominantly from one side, towards the strip but not towards the far field point. Subsequently, the Huygens source was used to excite an inductive impedance strip (which supports a surface wave) of finite extent, the IBC-MoM solution gave the expected end-fire beam. Next, a sinusoidally modulated impedance strip of finite extent was considered. The IBC-MoM radiation pattern agreed with Oliner-Hessel/PO approximate solution in terms of beam angle and beamwidth. Also, the IBC-MoM solution does predict the radiated beam due to the edge diffracted surface wave, which the Oliner-Hessel/PO approximate solution does not.

For an actual 3D leaky-wave antenna that can be built, it is imperative to consider the feed design. In an effort to excite the leaky-wave antenna with minimum spurious radiation from the feed, two feed designs were considered. One was based on a substrate integrated waveguide (SIW) and the other used a parallel plate waveguide. Based on full-wave simulation (CST) these feeds work reasonably well. Return loss was better than 10 dB for the considered feeds.

As a practical design point of interest it is important to consider the relation between the surface impedance and its physical realization. The theory of a grounded slab was used to map surface impedance onto the thickness of the slab analytically. This allows one to realize a given surface impedance modulation via slab thickness modulation of a grounded dielectric slab. Sinusoidal impedance modulation and square-wave impedance modulation was realized via slab thickness modulation. The far field radiation pattern for these leaky-wave antennas were computed with a full-wave 3D electromagnetic solver (CST) and validated with the 2D IBC-MoM.

A consequence of thickness modulation of the grounded dielectric slab was that the impedance boundary did not conform to the physical structural boundary. Investigation showed that if the gap between the impedance boundary and the physical structural boundary is less than or equal to 0.1λ, the space-wave contribution, in this case, is negligible and the field is predominantly a surface wave. Hence, the gap can be ignored.

Alternatively, we also considered modulated surface impedance realization by modulating the permittivity of a grounded slab. The theory of the grounded slab was employed to find $X_s(\epsilon_r(x))$, the relation between permittivity and surface reactance, which in turn allows for the reactance modulation through permittivity modulation of the slab. A square-wave reactance modulation was realized via permittivity modulation of a grounded dielectric slab. The far field radiation pattern of this leaky-wave antenna was computed via CST and is found to agree with the IBC-MoM radiation pattern. The spatial permittivity variation of a grounded slab was obtained via perforations. Eigenmode full-wave electromagnetic simulations (CST) were used to compute the propagation constant of the surface wave mode. This in turn allowed us to extract permittivity as a function of the hole radius and spacing. The surface wave impedance obtained from full-wave simulation (CST) was verified by a comparison with the expected surface wave impedance.

5.1 Future Work

The IBC-MoM, as presented, can be used to solve for the surface equivalent currents, which provides the radiated fields for an impedance strip having same Z_s on the two faces. The IBC-MoM could be generalized to allow for different impedances on the two faces of the impedance strip.

The IBC-MoM, as presented, is limited to 1D impedance variation $Z_s(x)$. For a pencil beam 2D impedance variation $Z_s(x, z)$ would be required. The IBC-MoM could be extended to allow for more general $Z_s(x, z)$ that varies in both directions on the surface.

Other structures like tapered-resistance radar absorbing materials could be studied with the IBC-MoM.

In this thesis only linear polarization was considered. For circular polarization a tensor surface impedance $\bar{\bar{\boldsymbol{Z}}}_{\boldsymbol{s}}$ would be required. A more general case would be 2D modulated tensor impedance $\bar{\bar{\boldsymbol{Z}}}_{\boldsymbol{s}}(x, z)$, which would be required for a circularly polarized pencil beam. IBC-MoM could be applied to solve for this kind of impedance.

We have only considered 1D dielectric thickness and permittivity modulation. The 2D dielectric thickness modulation and permittivity modulation can be possible avenues of 2D modulated impedance realization.

The question of beam reconfigurability was not considered in this thesis. A multi layered structure could be realized, in which the upper layer is the radiating aperture and a tunable lower layer brings about beam reconfiguration.

An interesting problem which could be explored is, to investigate the surface impedance of a dielectric grounded slab with a tensor permittivity and 2D variation $\bar{\bar{\boldsymbol{\epsilon}}}_{\boldsymbol{r}}(x, z)$.

Bibliography

[1] D. R. Jackson and A. A. Oliner, “Leaky-wave antennas.” in *Modern Antenna Handbook*, C. A. Balanis, Ed. Wiley, 2008, pp. 325–367.

[2] A. A. Oliner and D. R. Jackson, “Leaky-wave antennas.” in *Antenna Engineering Handbook*, J. Volakis, Ed. McGraw-Hill, 2007, pp. 11.1–11.56.

[3] R. Paknys, *Applied Frequency-Domain Electromagnetics*. Wiley/IEEE Press, 2016.

[4] A. Hessel, “General characteristics of travelling-wave antennas.” in *Antenna Theory Part II*, R. E. Collin and F. J. Zucker, Eds. McGraw-Hill, 1969, pp. 151–225.

[5] T. Tamir, “Leaky-wave antennas.” in *Antenna Theory Part II*, R. E. Collin and F. J. Zucker, Eds. McGraw-Hill, 1969, pp. 259–289.

[6] C. Caloz, D. R. Jackson, and T. Itoh, “Leaky-wave antennas.” in *Frontiers in Antennas.*, F. B. Gross, Ed. McGraw-Hill, 2010.

[7] D. R. Jackson, C. Caloz, and T. Itoh, “Leaky-wave antennas,” *Proceedings of the IEEE*, vol. 100, no. 7, pp. 2194–2206, 2012.

[8] A. Oliner and A. Hessel, “Guided waves on sinusoidally-modulated reactance surfaces,” *IRE Trans. Antennas Propagat.*, vol. 7, no. 5, pp. 201–208, 1959.

[9] S. Cho and R. King, “Radiation from a finite sinusoidally modulated reactance surface (SMRS),” *Radio Science*, vol. 11, no. 6, pp. 561–570, 1976.

[10] E. H. Newman and M. Schrote, “An open surface integral formulation for electromagnetic scattering by material plates,” *IEEE Trans. Antennas Propagat.*, vol. 32, no. 7, pp. 672–678, 1984.

[11] E. H. Bleszynski, M. K. Bleszynski, and T. Jaroszewicz, “Surface-integral equations for electromagnetic scattering from impenetrable and penetrable sheets,” *IEEE Antennas Propagat. Mag.*, vol. 35, no. 6, pp. 14–25, 1993.

[12] F. K. Schwering and S.-T. Peng, “Design of dielectric grating antennas for millimeter-wave applications,” *IEEE Trans. Microw. Theory Tech.*, vol. 31, no. 2, pp. 199–209, 1983.

[13] A. M. Patel and A. Grbic, “A printed leaky-wave antenna based on a sinusoidally-modulated reactance surface,” *IEEE Trans. Antennas Propagat.*, vol. 59, no. 6, pp. 2087–2096, 2011.

[14] A. J. Martinez-Ros, J. L. Gómez-Tornero, V. Losada, F. Mesa, and F. Medina, “Non-uniform sinusoidally modulated half-mode leaky-wave lines for near-field focusing pattern synthesis,” *IEEE Trans. Antennas Propagat.*, vol. 63, no. 3, pp. 1022–1031, 2015.

[15] X. Bai, S.-W. Qu, K.-B. Ng, and C. H. Chan, “Sinusoidally modulated leaky-wave antenna for millimeter-wave application,” *IEEE Trans. Antennas Propagat.*, vol. 64, no. 3, pp. 849–855, 2016.

[16] “High Frequency Electromagnetic Structure Simulator (HFSS)®,” https://www.ansys.com, 2018, accessed: 2018-12-08.

[17] P. Hariharan and P. Hariharan, *Optical Holography: Principles, Techniques and Applications*. Cambridge University Press, 1996.

[18] J. W. Goodman, *Introduction to Fourier Optics*. Roberts and Company Publishers, 2005.

[19] P. Checcacci, V. Russo, and A. Scheggi, “Holographic antennas,” *IEEE Trans. Antennas Propagat.*, vol. 18, no. 6, pp. 811–813, 1970.

[20] M. Nannetti, F. Caminita, and S. Maci, “Leaky-wave based interpretation of the radiation from holographic surfaces,” in *IEEE AP-S Int’l Symp.*, 2007.

[21] K. Iizuka, M. Mizusawa, S. Urasaki, and H. Ushigome, “Volume-type holographic antenna,” *IEEE Trans. Antennas Propagat.*, vol. 23, no. 6, pp. 807–810, 1975.

[22] P. Sooriyadevan, D. McNamara, A. Petosa, and A. Ittipiboon, “Electromagnetic modelling and optimisation of a planar holographic antenna,” *IET Microw., Antennas & Propagat.*, vol. 1, no. 3, pp. 693–699, 2007.

[23] B. H. Fong, J. S. Colburn, J. J. Ottusch, J. L. Visher, and D. F. Sievenpiper, “Scalar and tensor holographic artificial impedance surfaces,” *IEEE Trans. Antennas Propagat.*, vol. 58, no. 10, pp. 3212–3221, 2010.

[24] G. Minatti, F. Caminita, M. Casaletti, and S. Maci, “Spiral leaky-wave antennas based on modulated surface impedance,” *IEEE Trans. Antennas Propagat.*, vol. 59, no. 12, pp. 4436–4444, 2011.

[25] S. Pandi, C. A. Balanis, and C. R. Birtcher, “Design of scalar impedance holographic metasurfaces for antenna beam formation with desired polarization,” *IEEE Trans. Antennas Propagat.*, vol. 63, no. 7, pp. 3016–3024, 2015.

[26] S. K. Podilchak, L. Matekovits, A. P. Freundorfer, Y. M. Antar, and M. Orefice, “Controlled leaky-wave radiation from a planar configuration of width-modulated microstrip lines,” *IEEE Trans. Antennas Propagat.*, vol. 61, no. 10, pp. 4957–4972, 2013.

[27] M. Leontovich, “Investigation of propagation of radio waves, Part II,” *USSR Acad. Sci., Moscow*, 1948.

[28] “Cross-Platform Finite Element Analysis, Solver and Multiphysics Simulation Software” (COMSOL) ®,” https://www.comsol.com, 2018, accessed: 2018-12-08.

[29] “FEldberechnung für Körper mit beliebiger Oberfläche” (FEKO)®,” https://altairhyperworks.com, 2018, accessed: 2018-12-08.

[30] E. F. Knott, J. F. Schaeffer, and M. T. Tulley, *Radar Cross Section.* SciTech Publishing, 2004.

[31] S. A. Schelkunoff and H. T. Friis, *Antennas: Theory and Practice.* Wiley, 1952.

[32] L. B. Felsen and N. Marcuvitz, *Radiation and Scattering of Waves.* IEEE Press, 1994.

[33] R. L. Burden and J. D. Faires, *Numerical Analysis.* Cengage Learning, 2010.

[34] B. A. Khan and R. Paknys, “MoM solution for spatially modulated impenetrable impedance strip,” in *XXXII URSI General Assembly and Scientific Symp., Montreal, QC*, Aug 2017.

[35] ——, “IBC-MoM model for reactance modulated leaky-wave antennas,” *IEEE Trans. Antennas Propagat.*, vol. 66, no. 9, pp. 4895–4899, 2018.

[36] R. F. Harrington, *Field Computation by Moment Methods.* Oxford University Press, 1996.

[37] ——, *Time-Harmonic Electromagnetic Fields.* McGraw-Hill, 1961.

[38] “Computer Simulation Technology (CST)®,” https://www.cst.com, 2018, accessed: 2018-12-08.

[39] M. Al Sharkawy, A. Foroozesh, A. A. Kishk, and R. Paknys, “A robust horn ridge gap waveguide launcher for metal strip grating leaky wave antenna,” *IEEE Trans. Antennas Propagat.*, vol. 62, no. 12, pp. 6019–6026, 2014.

[40] A. Foroozesh, R. Paknys, D. R. Jackson, and J.-J. Laurin, “Beam focusing using backward-radiating waves on conformal leaky-wave antennas based on a metal strip grating,” *IEEE Trans. Antennas Propagat.*, vol. 63, no. 11, pp. 4667–4677, 2015.

[41] B. A. Khan and R. Paknys, “Realizing a modulated surface impedance for leaky wave antenna design,” in *AERO 17 63rd Aeronautics Conf. and AGM, Cdn. Aeronautics and Space Inst., Toronto, ON*, May 2017.

[42] ——, “Surface reactance on a periodic modulated thickness grounded slab,” in *ANTEM 2018 Int.’l Symp. Antenna Technol. and Applied Electromag., Waterloo, ON*, Aug 2018.

[43] ——, “Modulated permittivity-based leaky-wave antenna design,” in *IEEE AP-S/URSI Int’l Symp., Boston MA*, Jul 2018.

[44] C. H. Walter, *Traveling Wave Antennas*. McGraw-Hill, 1965.

[45] D. F. Sievenpiper, “Artificial impedance surfaces for antennas.” in *Modern Antenna Handbook*, C. A. Balanis, Ed. Wiley, 2008, pp. 737–777.

[46] A. Ishimaru, *Electromagnetic Wave Propagation, Radiation, and Scattering: from Fundamentals to Applications*. Wiley, 2017.

[47] N. Marcuvitz, *Waveguide Handbook*. McGraw-Hill, 1951.

Appendix A

Sinusoidally Modulated Impedance

Consider a sinusoidally modulated surface impedance along $y = 0$ as shown in Fig. A.1. The free space propagation constant k has the following relation with the propagation constants k_x in the x direction and k_y in the y direction

$$k^2 = k_x^2 + k_y^2 \tag{A.1}$$

$$k_y = \sqrt{k^2 - k_x^2}\,. \tag{A.2}$$

As the impedance is periodic along x, Floquet's theorem for periodicity (see [46], sec. 7.1) allows us to write

$$k_x = \beta_0 + \frac{2n\pi}{p} \tag{A.3}$$

where β_0 is the propagation wavenumber along the surface, $n = 0, \pm 1, \pm 2, \ldots$ denote the spatial harmonics and p is the period. Substituting (A.3) into (A.2) leads to

$$k_y = \sqrt{k^2 - \left(\beta_0 + \frac{2n\pi}{p}\right)^2} \tag{A.4}$$

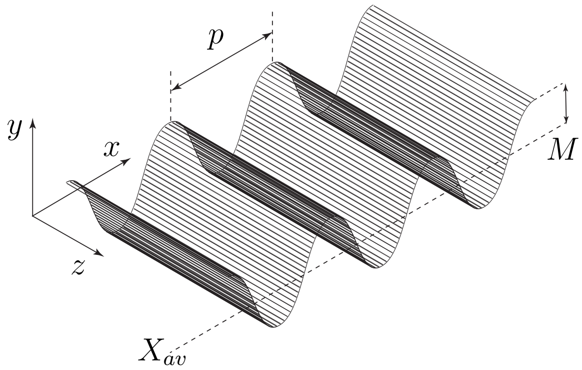

Figure A.1: Illustration of sinusoidally modulated surface impedance at $y = 0$.

Considering the TM$_x$ mode (H_z polarization) and (A.3), (A.4), it allows one to write $H_z(x, y)$ as (see [47], p. 88)

$$H_z(x,y) = e^{-j\beta_0 x} \sum_{n=-\infty}^{\infty} A_n(y) e^{-j\frac{2n\pi x}{p}} e^{-jk_y y} \,. \tag{A.5}$$

E_x and H_z at $y = 0$ are related through the surface impedance

$$E_x(x) = Z_s(x) H_z(x). \tag{A.6}$$

The mode voltage V_n can be expressed as

$$V_n = \int_0^p E_x(x)\, dx. \tag{A.7}$$

Using

$$Z_s(x) = jX_{av} \left[1 + M \cos\left(\frac{2\pi}{p} x \right) \right] \tag{A.8}$$

and (A.6), one can write

$$V_n = j \int_0^p X_{av} \left[1 + M \cos\left(\frac{2\pi}{p} x \right) \right] H_z(x)\, dx \tag{A.9}$$

which can be expanded as

$$V_n = jX_{av} \int_0^p H_z(x)\, dx + jMX_{av} \int_0^p \cos\left(\frac{2\pi}{p}x\right) H_z(x)\, dx. \tag{A.10}$$

Knowing

$$\cos\left(\frac{2\pi}{p}x\right) = \frac{e^{j\frac{2\pi x}{p}} + e^{-j\frac{2\pi x}{p}}}{2} \tag{A.11}$$

in conjunction with (A.5) allows one to write (A.10) as

$$\begin{aligned} V_n = {} & jX_{av} \int_0^p e^{-j\beta_0 x} \sum_{n=-\infty}^{\infty} A_n e^{-j\frac{2n\pi x}{p}}\, dx \\ & + j\frac{M}{2}X_{av} \left(\int_0^p e^{-j\beta_0 x} \sum_{n=-\infty}^{\infty} A_n e^{-j\frac{2(n+1)\pi x}{p}}\, dx + \int_0^p e^{-j\beta_0 x} \sum_{n=-\infty}^{\infty} A_n e^{-j\frac{2(n-1)\pi x}{p}}\, dx \right). \end{aligned}$$

Eq. (A.5) allows us to express this as

$$V_n = jX_{av} \int_0^p H_z(x)\, dx + j\frac{M}{2}X_{av} \left(\int_0^p H_z(x)_{n+1}\, dx + \int_0^p H_z(x)_{n-1}\, dx \right). \tag{A.12}$$

Mode current I_n can be written as

$$I_n = \int_0^p H_z(x)\, dx \tag{A.13}$$

allowing one to rewrite (A.12)

$$V_n = jX_{av} I_n + j\frac{M}{2}X_{av} \left(I_{n+1} + I_{n-1} \right). \tag{A.14}$$

The transverse resonance condition can be written as (see [3], sec. 3.7 for more extensive details)

$$\overleftarrow{Z} + \overrightarrow{Z} = 0 \tag{A.15}$$

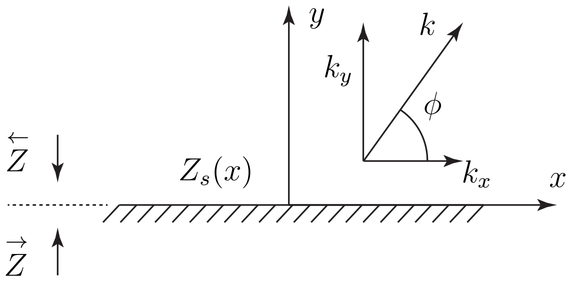

Figure A.2: Transverse resonance impedance illustration.

where $\overleftarrow{Z}$ is the impedance looking in the $-y$ direction and $\overrightarrow{Z}$ is the impedance looking in the $+y$ direction, as shown in Fig. A.2. The characteristic impedance for a y-directed transmission line in terms of the field components that are transverse to y is (see [3], p. 93)

$$Z = -\frac{E_x}{H_z} = \eta \sin\phi = \sqrt{\frac{\mu_0}{\epsilon_0}}\frac{k_y}{k} = \sqrt{\frac{\mu_0}{\epsilon_0}}\frac{k_y}{\omega\sqrt{\epsilon_0\mu_0}} = \frac{k_y}{\omega\epsilon_0} \tag{A.16}$$

where $\eta = 377\ \Omega$, μ_0 is the free space permeability and ϵ_0 is the free space permittivity. From the transverse resonance condition (A.15) and impedance (A.16) we can write

$$V_n = \frac{k_y}{\omega\epsilon_0} I_n. \tag{A.17}$$

Substituting V_n from (A.17) into (A.14) leads to

$$I_{n+1} + D_n I_n + I_{n-1} = 0 \tag{A.18}$$

where

$$D_n = \frac{2}{M}\left(1 - j\frac{k_y}{X_{av}\omega\epsilon_0}\right).$$

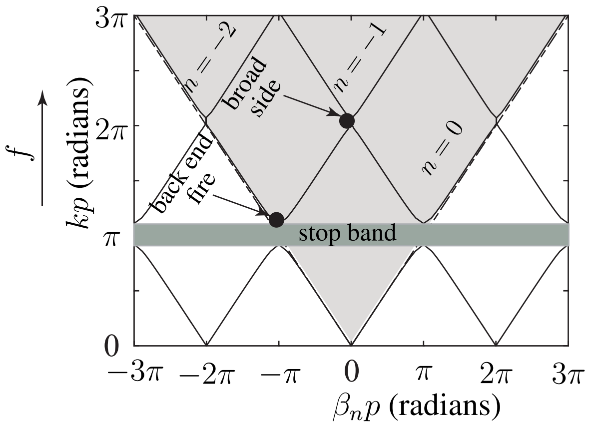

Figure A.3: Dispersion diagram for a sinusoidally modulated impedance (A.8) with $M = 0.2$, $X_{av} = 377\ \Omega$ and $p = \lambda = 1$ m.

Oliner and Hessel provided the following continued fraction solution for (A.18)

$$
\begin{aligned}
1-\frac{j}{X'_{av}}\sqrt{1-\left(\frac{k_x}{k}\right)^2} = & \frac{M^2/4}{1-\frac{j}{X'_{av}}\sqrt{1-\left(\frac{k_x}{k}+\frac{2\pi(-1)}{kp}\right)^2}}\Bigg| \\
& -\frac{M^2/4}{1-\frac{j}{X'_{av}}\sqrt{1-\left(\frac{k_x}{k}+\frac{2\pi(-2)}{kp}\right)^2}}\Bigg|\cdots \\
& +\frac{M^2/4}{1-\frac{j}{X'_{av}}\sqrt{1-\left(\frac{k_x}{k}+\frac{2\pi(1)}{kp}\right)^2}}\Bigg| \\
& -\frac{M^2/4}{1-\frac{j}{X'_{av}}\sqrt{1-\left(\frac{k_x}{k}+\frac{2\pi(2)}{kp}\right)^2}}\Bigg|\cdots
\end{aligned}
\tag{A.19}
$$

where $X'_{av} = X_{av}/\eta$. Alternatively (A.18) can be solved numerically by rewriting it in the following matrix form (see [4], p. 213). Let us use the $n = 0, \pm1, \pm2, \pm3, \pm4$ spatial harmonics only

$$\begin{bmatrix} \ddots & \ddots & \ddots & 0 & 0 & 0 & 0 \\ 0 & 1 & D_{-1} & 1 & 0 & 0 & 0 \\ 0 & 0 & 1 & D_0 & 1 & 0 & 0 \\ 0 & 0 & 0 & 1 & D_1 & 1 & 0 \\ 0 & 0 & 0 & 0 & \ddots & \ddots & \ddots \end{bmatrix} \begin{bmatrix} \vdots \\ I_{-1} \\ I_0 \\ I_1 \\ \vdots \end{bmatrix} = \begin{bmatrix} \vdots \\ 0 \\ 0 \\ 0 \\ \vdots \end{bmatrix}.$$

The above equation can be written as

$$\mathbf{DI} = 0. \tag{A.20}$$

kp can be specified in (A.20) and a nontrivial solution $\beta_n p$ can be obtained numerically by enforcing $|\mathbf{D}| = 0$. This allows one to compute the dispersion diagram shown in Fig. A.3.

Appendix B

Grounded Slab and IBC Slab

Consider a grounded slab excited by a magnetic line source M_{0z} located at (x_0, y_0) and the field point (where the field is evaluated) is at (x, y), as shown in Fig. B.1(a). A complete field solution for H_z can be found in [3], Chapter 12 and is summarized here:

$$H_z = -j\omega\epsilon_0 M_{0z} G \tag{B.1}$$

$$G = G_f + G_s + G_p. \tag{B.2}$$

The Green's function G has three parts. G_f is the direct or "free space" field contribution from the source and can be written as follows:

$$G_f = \frac{1}{j4} H_0^{(2)}(k_1\rho_0) \tag{B.3}$$

where $\rho_0 = \sqrt{(x-x_0)^2 + (y-y_0)^2}$ and $k_1 = 2\pi/\lambda$.

The reflected or "scattered" field from the slab is G_s. This can be represented by a Sommerfeld integral in the complex w plane:

$$G_s = \frac{1}{j4\pi} \int_P e^{-jk_1\rho\cos(w-\alpha)} \Gamma(w)\, dw \tag{B.4}$$

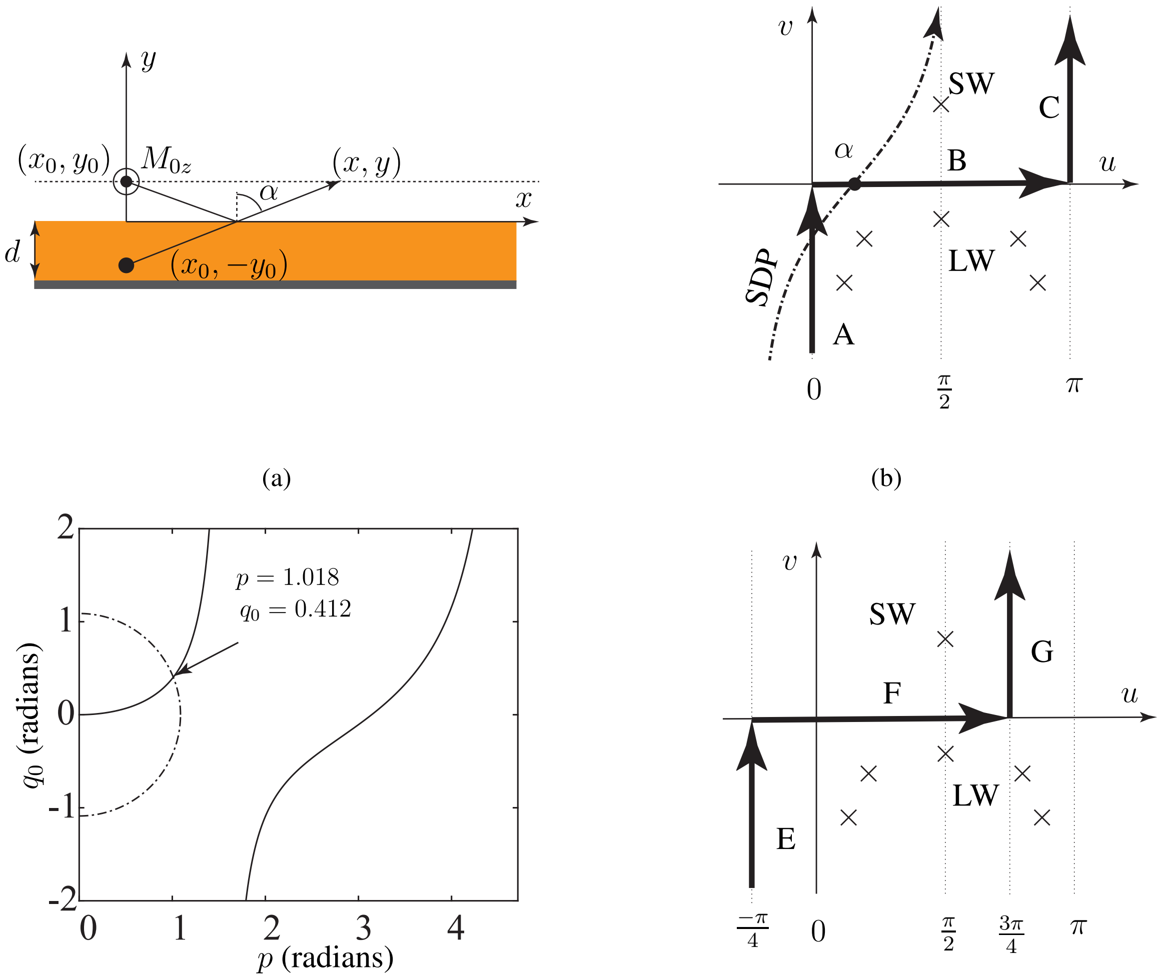

(a)

(b)

(c)

(d)

Figure B.1: a) Grounded dielectric slab excited by a magnetic line source M_{0z} [42]. b) w plane showing SDP and ABC integration paths along with the surface wave (SW) and leaky-wave poles (LW) [42]. c) Plot of (B.13) and (B.14) [42]. d) w plane showing EFG (Z-path) integration path and surface wave pole (SW) and leaky-wave poles (LW).

where $x - x_0 = \rho \sin \alpha$ and $y + y_0 = \rho \cos \alpha$ as shown in Fig. B.1(a).

$\Gamma(w)$ is the magnetic field reflection coefficient

$$\Gamma(w) = -\frac{j\kappa_2 \sin(\kappa_2 d) - \epsilon_r \kappa_1 \cos(\kappa_2 d)}{j\kappa_2 \sin(\kappa_2 d) + \epsilon_r \kappa_1 \cos(\kappa_2 d)} \tag{B.5}$$

where $w = u + jv$, $\nu = k_1 \sin w$, $\kappa_1 = k_1 \cos w$, $k_2 = k_1\sqrt{\epsilon_r}$ and $\kappa_2 = \sqrt{k_2^2 - \nu^2}$.

The integration path P is the steepest descent path (SDP) which is given by:

$$\cos(u-\alpha)\cosh v = 1. \tag{B.6}$$

The poles of $\Gamma(w)$ in the w plane are shown in Fig. B.1(b). The saddle point (see [3], p. 387) is at $w=\alpha$, which determines the SDP's position in the w plane.

The surface wave pole contribution G_p in (B.2) is (see [3], p. 403)

$$G_p = \frac{j\epsilon_r q}{k_1 d \sin w_p B_p} e^{-j\nu_p|x-x_0|} e^{-j\kappa_p(y+y_0)} U(\alpha-\alpha_p) \tag{B.7}$$

$$B_p = j\epsilon_r\left(1-(q/p)^2\right) - q\left(1-(\epsilon_r q/p)^2\right) \tag{B.8}$$

where $p=\kappa_2 d$, $q=\kappa_1 d$, $\nu_p = k_1 \sin w_p$ and $\kappa_p = k_1\cos w_p$. The step function $U(\alpha-\alpha_p)$ indicates that G_p does not contribute at angles $\alpha < \alpha_p$; this will be discussed later.

The integral in (B.4) for G_s can be evaluated by the saddle point method with the result that

$$G_s \sim \frac{1}{j4}\sqrt{\frac{2}{\pi k_1 \rho}} e^{-j(k_1\rho-\pi/4)}\Gamma(k_1\sin\alpha). \tag{B.9}$$

This asymptotic approximation gives good results if $k_1\rho >> 1$. Near the source it is not accurate. For this case the integral in (B.4) has to be evaluated numerically. The integration can be done along the SDP. In this case, since u depends on v through the SDP definition, and u can be eliminated in the following way. Consider (B.4) with $w = u + jv$ which can be rewritten as:

$$G_s = \frac{1}{j4\pi}\int_P e^{-jk_1\rho\cos(u+jv-\alpha)}\Gamma(u+jv)\,(du+jdv).$$

To eliminate $u = u(v)$ from this integral the SDP (B.6) can be rewritten as:

$$\begin{aligned}
\cos(u-\alpha)\cosh v &= 1 \\
\cos(u-\alpha)\cosh v &= \cosh^2 v - \sinh^2 v \\
\cos(u-\alpha) &= \cosh v - \frac{\sinh^2 v}{\cosh v} \\
\frac{\cos(u-\alpha)}{\cosh v} &= 1 - \frac{\sinh^2 v}{\cosh^2 v} \\
\frac{\cos(u-\alpha)}{1/\cos(u-\alpha)} &= 1 - \tanh^2 v \\
\cos^2(u-\alpha) &= 1 - \tanh^2 v \\
\tanh^2 v &= 1 - \cos^2(u-\alpha) \\
\tanh^2 v &= \sin^2(u-\alpha)
\end{aligned}$$

$$\Rightarrow \sin(u-\alpha) = \pm \tanh v. \tag{B.10}$$

To find du in terms of dv we differentiate the SDP:

$$\begin{aligned}
\frac{d}{dv}(\cos(u-\alpha)\cosh v) &= 0 \\
-\sin(u-\alpha)\frac{du}{dv}\cosh v + \cos(u-\alpha)\sinh v &= 0 \\
\sin(u-\alpha)\cosh v\; du &= \cos(u-\alpha)\sinh v\; dv \\
du &= \frac{\cos(u-\alpha)}{\sin(u-\alpha)}\frac{\sinh v}{\cosh v}dv \\
du &= \frac{\cos(u-\alpha)}{\tanh v}\tanh v\; dv \\
du &= \cos(u-\alpha)\; dv \\
du &= \frac{1}{\cosh v}\; dv
\end{aligned}$$

$$\Rightarrow du = \operatorname{sech} v \; dv. \tag{B.11}$$

Using (B.6) (B.10) and (B.11) then allows us to rewrite (B.4) in the form

$$G_s = \frac{e^{-jk_1\rho}}{j4\pi} \int_P e^{(-k_1\rho \tanh v \sinh v)} \Gamma(v) \; (\operatorname{sech} v + j) dv. \tag{B.12}$$

There can be a surface wave pole as shown in Fig. B.1(b). For example, the surface wave pole w_p when $\epsilon_r = 4.0$ and $d = 0.1\lambda$ (where λ is the free-space wavelength) can be found by solving numerically (by secant method) the following pair of equations (see [3], p. 402):

$$p \tan p = \epsilon_r q_0 \tag{B.13}$$

$$p^2 + q_0^2 = (\mu_r \epsilon_r - 1)(k_1 d)^2 \tag{B.14}$$

where $jq = q_0$ and p, q_0 are real. A plot of (B.13) and (B.14) and the graphical solution is shown in Fig B.1(c), which shows that only the dominant TM$_0$ mode exists. From p and q_0 it follows that $w_p = \pi/2 + j0.617$. Knowing w_p allows one to calculate the angle $\alpha = \alpha_p$ at which the SDP intercepts the pole. This is done by solving (B.6) in the following way:

$$\cos(\pi/2 - \alpha_p) \cosh(0.617) = 1$$

$$\alpha_p = \sin^{-1}(\operatorname{sech}(0.617)) = 56.6^0.$$

At $\alpha_p = 56.6^0$ the SDP passes through the surface wave pole which is undesirable for the numerical integration. To avoid this problem the SDP can be deformed into three linear paths A, B and C. (In this deformation the surface-wave pole is crossed so the step function in (B.7) is taken to be

$U = 1$). These paths can be mathematically expressed as follows:

$$\begin{aligned} G_A &= \frac{1}{4\pi}\int_{-v_0}^{0} e^{-jk_1\rho\cos(jv-\alpha)}\Gamma(0+jv)\,dv \\ G_B &= \frac{1}{j4\pi}\int_{0}^{\pi} e^{-jk_1\rho\cos(u-\alpha)}\Gamma(u+j0)\,du \\ G_C &= \frac{1}{4\pi}\int_{0}^{v_0} e^{-jk_1\rho\cos(\pi+jv-\alpha)}\Gamma(\pi+jv)\,dv \end{aligned}$$

where

$$G_s = G_A + G_B + G_C. \tag{B.15}$$

These paths are shown in Fig. B.1(b) in the w plane. The integration limits at $\pm v_0$ are determined by requiring:

$$|e^{-jk_1\rho\cos(jv-\alpha)}| \leq 10^{-4}.$$

In order to avoid integrand oscillations we can choose the SDP when $0^0 \leq \alpha < 45^0$. In order to have an integration path well away from the pole w_p we can choose the ABC path when $45^0 \leq \alpha \leq 90^0$. However, this integration path switch causes the pole w_p crossing, which makes the integral G_s discontinuous.

In order to avoid the integration path switch, we can find an other possible integration path by examining carefully the behavior of the exponential term in (B.4)

$$e^{-jk_1\rho\cos(w-\alpha)} = e^{-jk_1\rho\cos(u+jv-\alpha)} = \underbrace{e^{-jk_1\rho\cos(u-\alpha)\cosh v}}_{\text{oscillating term}}\overbrace{e^{-k_1\rho\sin(u-\alpha)\sinh v}}^{\text{decay term}}. \tag{B.16}$$

The decay term in (B.16) approaches zero with $|v|$ increasing along path E and G. These paths are shown in Fig. B.1(d). As $u = -\pi/4$ for path E and $u = 3\pi/4$ for path G, this means $\sin(u - \alpha)$ remains between $-1/\sqrt{2}$, -1 and $1/\sqrt{2}$ for $0 \leq \alpha \leq 90°$. This allows one to find the integration limit v_0 as

$$e^{\frac{k_1\rho}{\sqrt{2}}\sinh v} \leq 10^{-4} \tag{B.17}$$

$$v_0 \leq \sinh^{-1}\left(\frac{\sqrt{2}}{k_1\rho}\ln(10^{-4})\right). \tag{B.18}$$

We can take $n = 10/T$ slices for the numerical integration, where T is the period of oscillation and can be calculated by considering the oscillating term in (B.16). As v_0 is known from (B.18) and $\cos(u-\alpha)$ remains between $-1/\sqrt{2}$, 0 and $1/\sqrt{2}$ for $0 \leq \alpha \leq 90°$, one can write

$$e^{-j\frac{k_1\rho}{\sqrt{2}}\cosh v_0}$$

for the period of oscillation T, we can write

$$\frac{k_1\rho}{\sqrt{2}}\left[\cosh v_0 - \cosh(v_0+T)\right] = 2\pi. \tag{B.19}$$

As $\cosh v_0 = \dfrac{e^{-v_0}}{2} + \dfrac{e^{v_0}}{2} \approx \dfrac{e^{v_0}}{2}$, one can write

$$\frac{k_1\rho}{\sqrt{2}}\left[\frac{e^{v_0}}{2} - \frac{e^{(v_0+T)}}{2}\right] = 2\pi \tag{B.20}$$

$$T = \ln\left(\frac{\pi\sqrt{2}}{e^{v_0}k_1\rho} + 1\right). \tag{B.21}$$

The mathematical expression for the integration path along EFG is

$$\begin{aligned}
G_E &= \frac{1}{4\pi}\int_{-v_0}^{0} e^{-jk_1\rho\cos(-\pi/4+jv-\alpha)}\Gamma(-\pi/4+jv)\,dv \\
G_F &= \frac{1}{j4\pi}\int_{-\pi/4}^{3\pi/4} e^{-jk_1\rho\cos(u-\alpha)}\Gamma(u+j0)\,du \\
G_G &= \frac{1}{4\pi}\int_{0}^{v_0} e^{-jk_1\rho\cos(3\pi/4+jv-\alpha)}\Gamma(3\pi/4+jv)\,dv
\end{aligned}$$

where

$$G_s = G_E + G_F + G_G. \tag{B.22}$$

In the interest of brevity, let us call the path EFG the Z-path. Evaluating numerically the Sommerfeld integral (B.4) along the Z-path does not need a path switch because the integrand is well behaved for $0 \leq \alpha \leq 90^\circ$.

E_x can be computed by taking the curl of (B.1), which leads to

$$E_x = E_x^f + E_x^s + E_x^p \tag{B.23}$$

where

$$E_x^f = \frac{M_{0z}k_1}{j4} H_1^{(2)}(k_1\rho_0)\frac{(y-y_0)}{\rho_0} \tag{B.24}$$

$$E_x^s = \frac{M_{0z}k_1}{4\pi}\int_P e^{-jk_1\rho\cos(w-\alpha)}\cos w \;\; \Gamma(w)\,dw \tag{B.25}$$

$$E_x^p = j\kappa_p M_{0z}\frac{j\epsilon_r q}{k_1 d\sin w_p B_p} e^{-j\nu_p|x-x_0|}e^{-j\kappa_p(y+y_0)}U(\alpha-\alpha_p) \tag{B.26}$$

where B_p is defined in (B.8). The integral in (B.25) can be numerically evaluated in the w plane along the Z-path, which is shown in Fig. B.1(d).

With only a minor modification we can also have G and H_z for the IBC plane. By using a new Γ (see [32], Chapter 5)

$$\Gamma = \frac{\cos w - \bar{Z}_s}{\cos w + \bar{Z}_s}, \tag{B.27}$$

where $\bar{Z}_s = Z_s/\eta$ and $\eta = 377\ \Omega$, one can get the H_z for the IBC plane. The contribution due to G_p in this case comes from a pole w_p at $\bar{Z}_s = -\cos w_p$.

Appendix C

Surface Wave Radiation

To compute the radiation from a discontinuous surface wave field, let us consider a surface wave field along $y = 0$ which can be expressed as

$$H_z = -j\omega\epsilon_0 G \tag{C.1}$$

$$G = Ae^{-j\nu_p|x|}e^{-j\kappa_p y} \tag{C.2}$$

where

$$A = \frac{j\epsilon_r q}{kd\sin w_p B_p}e^{-j\kappa_p y_0} \tag{C.3}$$

where $k = 2\pi/\lambda$, B_p is defined in (B.8), w_p is the pole location in the w plane, ν_p is surface wave propagation constant along x and κ_p is the decay constant along y (see Appendix B for details). This surface wave represents part of the total field that is produced by a z-directed magnetic line source at $(x, y) = (0, y_0)$.

A surface wave does not radiate, however because of the $|x|$ the surface electric field E_y in (C.1), (C.2) is discontinuous at $x = 0$ so there will be radiation associated with the discontinuity.

We wish to find the radiated magnetic field H_z^{rd} in $y \geq 0$ due to the surface wave along $y = 0$ [1].

---

[1] The derivation for radiation by a surface wave with a source discontinuity was provided to us by Professor David R. Jackson in a private communication.

First let us consider the magnetic field H_z (C.1) along $y = 0$. Let us take the G from (C.2) and substitute $y = 0$

$$G = Ae^{-j\nu_p|x|}. \tag{C.4}$$

The field at any point (x, y) may be written as

$$G(x, y) = \frac{1}{2\pi} \int_{-\infty}^{+\infty} \tilde{G}(k_x, 0)\, e^{-jk_x x} e^{-jk_y y}\, dk_x. \tag{C.5}$$

Here, $k = \sqrt{k_x^2 + k_y^2}$ which allow us to write $k_y = \sqrt{k^2 - k_x^2}$. Introducing polar coordinates $x = \rho\cos\phi$, $y = \rho\sin\phi$ and a normalized wavenumber $\bar{k}_x = k_x/k$ we get

$$G(x, y) = \frac{k}{2\pi} \int_{-\infty}^{+\infty} \tilde{G}(k_x, 0)\, e^{-jk\rho(\bar{k}_x \cos\phi + \sqrt{1-\bar{k}_x^2}\sin\phi)}\, d\bar{k}_x. \tag{C.6}$$

The stationary-phase point is at $\bar{k}_{x0} = \cos\phi$. From the stationary-phase method (see [3], sec. 5.5),

$$I(\Omega) \sim \int_{\alpha_1}^{\alpha_2} f(x)\, e^{j\Omega g(x)}\, dx \sim f(x_0)\, e^{j\Omega g(x_0)} \sqrt{\frac{2\pi}{\Omega|g''(x_0)|}}\, e^{\pm j\pi/4} \tag{C.7}$$

where $g'(x_0) = 0$ and the $\pm$ is for $g''(x_0) > 0$ or $g''(x_0) < 0$ respectively. It is assumed that the integrand is sufficiently small near the endpoints α_1, α_2 so that they do not contribute.

In our case $g''(\bar{k}_{x0}) = \csc^2\phi$ so that

$$G(\rho, \phi) = \sqrt{\frac{k}{2\pi}}\, e^{j\pi/4}\, \tilde{G}(k\cos\phi, 0)\, \sin\phi\, \frac{e^{-jk\rho}}{\sqrt{\rho}}. \tag{C.8}$$

Using (C.5) the Fourier transform of the interface field is

$$\tilde{G}(k\cos\phi, 0) = A \int_{-\infty}^{+\infty} e^{-j\nu_p|x|} e^{jk_x x}\, dx = 2A \int_{0}^{+\infty} e^{-j\nu_p x} \cos(k_x x)\, dx \tag{C.9}$$

assuming an infinitesimal amount of loss which makes ν_p complex, hence the contribution from

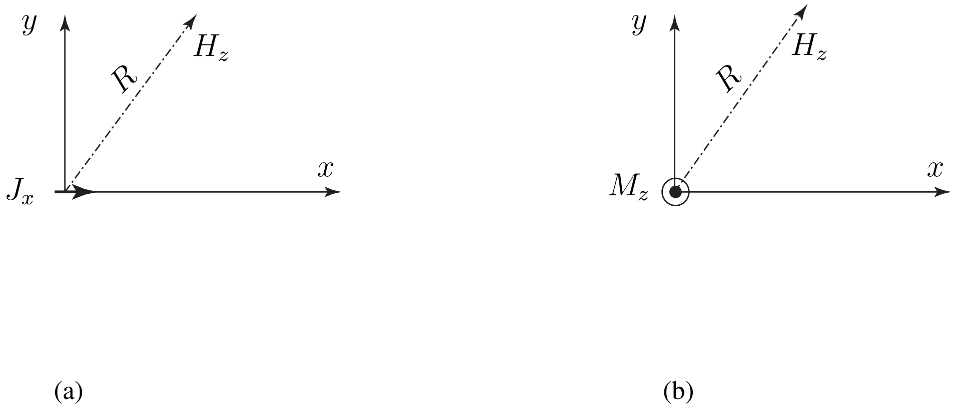

Figure C.1: a) Electric current J_x radiating b) Magnetic current M_z radiating

the endpoint at $+\infty$ is zero, so that

$$\tilde{G}(k\cos\phi, 0) = 2A\, \frac{e^{-j\nu_p x}(-j\nu_p \cos(k_x x) + k_x \sin(k_x x))}{k_x^2 - \nu_p^2}\Bigg|_0^{+\infty} = 2A\frac{j\nu_p}{k_x^2 - \nu_p^2}. \tag{C.10}$$

Hence, we have

$$\tilde{G}(k\cos\phi, 0) = 2A\frac{j\nu_p}{k^2\cos^2\phi - \nu_p^2}. \tag{C.11}$$

Substituting this in to (C.8) leads to

$$G(\rho, \phi) = A\,\sqrt{\frac{2}{\pi k}}\; e^{j\pi/4}\; \frac{jk\nu_p}{k^2\cos^2\phi - \nu_p^2}\; \sin\phi\; \frac{e^{-jk\rho}}{\sqrt{\rho}}. \tag{C.12}$$

The radiated magnetic field $H_z^{\mathrm{rd}}(H_z)$ due to the aperture magnetic field H_z can now be expressed as

$$H_z^{\mathrm{rd}}(H_z) = \frac{-j\omega\epsilon_0}{2}\; A\,\sqrt{\frac{2}{\pi k}}\; e^{j\pi/4}\; \frac{jk\nu_p}{k^2\cos^2\phi - \nu_p^2}\; \sin\phi\; \frac{e^{-jk\rho}}{\sqrt{\rho}}. \tag{C.13}$$

In order to find the radiated magnetic field $H_z^{\mathrm{rd}}(E_x)$ due to the aperture electric field E_x, one can compare the field solution for the two problems shown in Fig. C.1. Consider an electric current

J_x radiating H_z as shown in Fig. C.1(a), which can be expressed as (see [3], (4.104))

$$H_z = \frac{-jk}{4}\, J_x\, \sin\phi\, H_1^{(2)}(kR). \tag{C.14}$$

The Hankel function asymptotic approximation for large kR (the Debye approximation) (see [3], Appendix C) is

$$H_0^{(2)}(kR) \sim \sqrt{\frac{2}{\pi kR}}\, e^{-j(kR-\pi/4)} \tag{C.15}$$

$$H_1^{(2)}(kR) \sim \sqrt{\frac{2}{\pi kR}}\, e^{-j(kR-\pi/4)}\, e^{j\pi/2} \sim jH_0^{(2)}(kR). \tag{C.16}$$

Using (C.16), (C.14) can be rewritten as

$$H_z \sim \frac{k}{4}\, J_x\, \sin\phi\, H_0^{(2)}(kR). \tag{C.17}$$

Now consider a magnetic current M_z radiating H_z as shown in Fig. C.1(b), which can be expressed as (see [3], (4.105))

$$H_z = \frac{-k}{4\eta}\, M_z\, H_0^{(2)}(kR). \tag{C.18}$$

Considering that

$$M_z|_{y=0} = Z_s J_x \tag{C.19}$$

it allows (C.18) to be rewritten as

$$H_z = \frac{-k}{4}\, \bar{Z}_s\, J_x\, H_0^{(2)}(kR) \tag{C.20}$$

where $\bar{Z}_s = Z_s/\eta$ and $\eta = 120\pi\ \Omega$. The comparison between (C.17) and (C.20) reveals that replacing $\sin\phi$ with $-\bar{Z}_s$ in (C.17) gives H_z due to M_z. Using this same rationale, we can replace

$\sin\phi$ in (C.13) with $-\bar{Z}_s$. So the radiated magnetic field $H_z^{\text{rd}}(E_x)$ due to the aperture electric field E_x becomes

$$H_z^{\text{rd}}(E_x) = \frac{-j\omega\epsilon_0}{2}\, A \sqrt{\frac{2}{\pi k}}\, e^{j\pi/4}\, \frac{jk\nu_p}{k^2\cos^2\phi - \nu_p^2}\, \cos w_p\, \frac{e^{-jk\rho}}{\sqrt{\rho}}. \tag{C.21}$$

where $\cos w_p = -\bar{Z}_s$ (see [32], p. 555).

The radiated magnetic field H_z^{rd} due to the aperture field can be computed by adding (C.13) and (C.21)

$$H_z^{\text{rd}} = H_z^{\text{rd}}(H_z) + H_z^{\text{rd}}(E_x) \tag{C.22}$$

$$H_z^{\text{rd}} = \frac{-j\omega\epsilon_0}{2}\, A \sqrt{\frac{2}{\pi k}}\, e^{j\pi/4}\, \frac{jk\nu_p}{k^2\cos^2\phi - \nu_p^2}\, [\sin\phi + \cos w_p]\, \frac{e^{-jk\rho}}{\sqrt{\rho}}. \tag{C.23}$$

The source for the surface wave is the magnetic current sheet M_z at $x = 0$. The field due to this sheet is

$$H_z(M_z^{\text{sheet}}|_{x=0}) = -j\omega\epsilon_0\, A\, e^{-jk\rho\cos(w_p-\alpha)} \tag{C.24}$$

Adding (C.23) and (C.24) gives the total magnetic field radiated by a surface wave discontinuity at $x = 0$

$$H_z^{\text{swr}} = H_z^{\text{rd}} + H_z(M_z^{\text{sheet}}|_{x=0}). \tag{C.25}$$

Appendix D

Singular Integrals in IBC-MoM

This appendix provides expressions for the IBC-MoM incident field, self-impedance, and self-admittance terms. The incident field follows readily from the impressed sources J_{0x} and M_{0z}. In the MoM procedure, finding the incident field is straightforward, except when the match point is directly beneath the source at x_0. In this case, G_e and G_m are singular when $x = x_0$. In order to evaluate the incident field we can replace the infinitesimal line sources J_{0z} and M_{0x} by narrow current ribbons of width Δ along x, as shown in Fig. D.1(a) and (b). The total field due to the Huygens source includes the contribution from both J_{0z} and M_{0x} as expressed in (3.37) and (3.38). When $x \approx x_0$, small-argument approximations for G_e and G_m are used. The incident field on the impedance strip can then be expressed as

$$E_z^i(x) = \begin{cases} -\displaystyle\int_{x_0-\Delta/2}^{x_0+\Delta/2} J_{0z} G_e(x, x_0)\, dx_0 & \text{when } x \neq x_0 \\ \\ -p_e S_1 + \dfrac{p_m}{2\Delta} & \text{when } x = x_0 \end{cases} \tag{D.1}$$

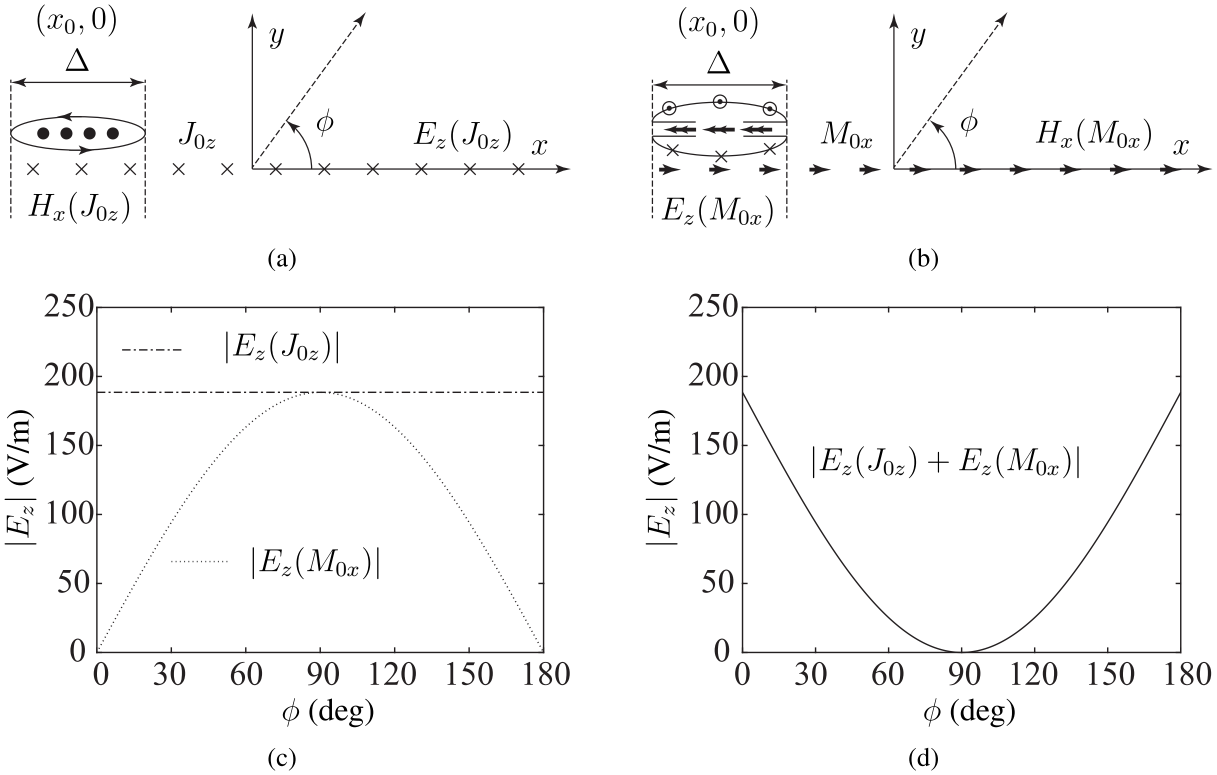

Figure D.1: a) Illustration of the near field due to J_{0z} ribbon of width Δ. b) Illustration of the near field due to M_{0x} ribbon of width Δ. c) Far field $|E_z|$ due to J_{0z} and M_{0x}. d) Total far field $|E_z|$ due to J_{0z} and M_{0x}.

$$H_x^i(x) = \begin{cases} -\displaystyle\int_{x_0-\Delta/2}^{x_0+\Delta/2} M_{0x} G_m(x, x_0)\, dx_0 & \text{when } x \neq x_0 \\ \\ -p_m S_2 + \dfrac{p_e}{2\Delta} & \text{when } x = x_0 \end{cases} \tag{D.2}$$

where

$$S_1 = \frac{\omega\mu}{4}\left(1 - j\frac{2}{\pi}[\ln(\gamma k \Delta/4) - 1]\right)$$
$$S_2 = \frac{k}{4\eta}\left\{1 - j\frac{2}{\pi}\ln\left(\frac{\gamma_0 k \Delta}{4e}\right)\right\} - \frac{1}{2\eta\Delta}H_1^{(2)}(k\Delta/2)$$

γ=$1.781072416\cdots$ and γ_0=exp γ=$0.577215665\cdots$. $p_e = J_{0z}\Delta$ and $p_m = M_{0x}\Delta$ are the strengths of electric and magnetic current ribbons of width Δ; see [3] (sec. 6.3.4) for a more extensive explanation.

It is noted that the J_{0z} ribbon only contributes to H_x^i at the match point directly underneath the ribbon, whereas it contributes to E_z^i everywhere along the strip. Similarly, the M_{0x} ribbon only contributes to E_z^i underneath the ribbon but contributes to H_x^i everywhere along the strip. This is illustrated in Fig. D.1(a) and (b).

Similar considerations apply to singularities arising in the self-impedance terms which have the match point and current pulse at the same location x_m. Using a small-argument approximation for G_e in (3.30) leads to

$$Z_{mm} = \frac{Z_s(x_m)}{2} + \Delta S_1$$

and using a small-argument approximation for G_m in (3.31),

$$Y_{mm} = \frac{Y_s(x_m)}{2} + \Delta S_2.$$

The far field radiation of the Huygens source is shown in Fig. D.1(c) and (d), which shows zero total field in the $+y$ direction ($\phi = 90°$). This source is good for exciting the guided mode on an impedance strip. This work is reported in [35].